

AD A089710

(18) AFOSR-TR- 80-0872

(9) SEMI-ANNUAL TECHNICAL REPORT
1 October 1979 - 31 March 1980

LEVEL II
6
B.S.

ARPA Order No.: 3291.30
Program Code: OD60
Name of Contractor: California Institute of Technology
Effective Date of Contract: 1 October 1979
Contract Expiration Date: 30 September 1980
Amount of Contract: \$150,000
Contract Number: (15) F49620-77-C-0022, ARPA Order-3291
Principal Investigators: (10) David G. Harkrider
(213) 795-6811, ext. 2910
Donald V. Helmburger
(213) 795-6811, ext. 2911
J. Bernard Minster
(213) 795-6811, ext. 2909
Program Manager and
Telephone Number: William J. Best
(202) 767-5011
Short Title of Work: (6) Body and Surface Wave Modeling
of Observed Seismic Events

The views and conclusions contained in this document are those of the authors and should not be interpreted as necessarily representing the official policies, either expressed or implied, of the Defense Advanced Research Projects Agency or the U.S. Government.

Sponsored by
Advanced Research Projects Agency (DOD)
ARPA Order No. 3291.30
Monitored by AFOSR Under Contract No. F49620-77-C-0022

DTIC
SELECTED
SEP 30 1980
S D

A

Seismological Laboratory
Division of Geological and Planetary Sciences
California Institute of Technology
Pasadena, California 91125

Approved for public release;
distribution unlimited.
JOS

320050

80 9 22 174

UNCLASSIFIED

SECURITY CLASSIFICATION OF THIS PAGE (When Data Entered)

REPORT DOCUMENTATION PAGE		READ INSTRUCTIONS BEFORE COMPLETING FORM
1. REPORT NUMBER AFOSR-TR-80-0872	2. GOVT ACCESSION NO. AD-A089 710	3. RECIPIENT'S CATALOG NUMBER
4. TITLE (and Subtitle) Body and Surface Wave Modeling of Observed Seismic Events	5. TYPE OF REPORT & PERIOD COVERED 1 Oct. 1979 - 31 March 1980 Semi-Annual Technical Report	
7. AUTHOR(s) David G. Harkrider Donald V. Helmberger J. Bernard Minster	6. PERFORMING ORG. REPORT NUMBER	
9. PERFORMING ORGANIZATION NAME AND ADDRESS California Institute of Technology Seismological Laboratory, 252-21 Pasadena, California 91125	10. PROGRAM ELEMENT, PROJECT, TASK AREA & WORK UNIT NUMBERS ARPA Order 3291-31 OD60	
11. CONTROLLING OFFICE NAME AND ADDRESS DARPA 1400 Wilson Blvd. Arlington, VA 22209	12. REPORT DATE September 1980	
14. MONITORING AGENCY NAME & ADDRESS(if different from Controlling Office) AFOSR/NP Bolling AFB Wash DC 20332	13. NUMBER OF PAGES 126	
16. DISTRIBUTION STATEMENT (of this Report) Approved for public release; distribution unlimited	15. SECURITY CLASS. (of this report) Unclassified	
17. DISTRIBUTION ST. (if different from abstract entered in Block 20, if different from Report)	15a. DECLASSIFICATION/DOWNGRADING SCHEDULE	
18. SUPPLEMENTARY NOTES		
19. KEY WORDS (Continue on reverse side if necessary and identify by block number) Linear modeling of nonlinear sources generalized rays Pn to PL, elastic representation theory upper mantle structure cylindrical Green's functions		
20. ABSTRACT (Continue on reverse side if necessary and identify by block number) The research performed under this contract during the period 1 October through 31 March 1980 can be divided into three main topics, excitation of surface waves from complex source regions, modeling of Pn to PL waves for source inversion and determining earthquake source characteristics using synthetic teleseismic long period body and surface waves.	In Section II preliminary results are presented which show the	

M sub S

feasibility of using the representation theorem to investigate the excitation of surface waves due to complicated sources in complex source regions. The research is motivated by our lack of knowledge concerning the theoretical quantitative effects of various source regions and geometries on M_s .

P sub n

→ In Section III, it is shown that a simple one-layer crust mantle structure is adequate to model P_n to PL waves at ranges 1 to 12 degrees for most of the western U.S. In Section IV an inversion technique of this procedure is used to determine the source parameters of three western U.S. earthquakes. The inversion technique appears ideal for determining the source parameters of moderate size earthquake. In addition, in the course of inverting a number of events, anomalous travel paths will become apparent and can be investigated.

→ Section V concerns the use of synthetic long period body and surface waves to determine the depth, dimensions, and moment of the 1976 Friuli, Italy earthquake and its principal aftershock.

T

TABLE OF CONTENTS

	Page
I. Summary- - - - -	1
II. A method for propagating surface waves from complex seismic source regions to teleseismic distances - Preliminary results- - - - -	2
III. Modeling the long-period body-waves from shallow earthquakes at regional ranges - - - -	8
IV. A technique for the inversion of regional data in source parameter studies- - - - -	47
V. Teleseismic observations of the 1976 Friuli, Italy earthquake sequence- - - - -	80

Accession For	
NTIS	GA-141
DDC	248
Unannounced	<input type="checkbox"/>
Justification _____	
By _____	
Distribution/ _____	
Availability Categ _____	
Dist.	Avail and/or special
A	

i

AIR FORCE OFFICE OF SCIENTIFIC RESEARCH (AFSC)
NOTICE OF TRANSMITTAL TO DDC
This technical report has been reviewed and is approved for public release IAW AFR 190-12 (7b). Distribution is unlimited.
A. D. BLOSE
Technical Information Officer

I. SUMMARY

The research performed under this contract during the period 1 October through 31 March 1980 can be divided into three main topics, excitation of surface waves from complex source regions, modeling of P_n and P_L waves for source inversion and determining earthquake source characteristics using synthetic teleseismic long period body and surface waves.

In Section II preliminary results are presented which show the feasibility of using the representation theorem to investigate the excitation of surface waves due to complicated sources in complex source regions. The research is motivated by our lack of knowledge concerning the theoretical quantitative effects of various source regions and geometries on M_s .

In Section III, it is shown that a simple one-layer crust mantle structure is adequate to model P_n to P_L waves at ranges 1 to 12 degrees for most of the western U.S. In Section IV an inversion technique of this procedure is used to determine the source parameters of three western U.S. earthquakes. The inversion technique appears ideal for determining the source parameters of moderate size earthquakes. In addition, in the course of inverting a number of events, anomalous travel paths will become apparent and can be investigated.

Section V concerns the use of synthetic long period body and surface waves to determine the depth, dimensions, and moment of the 1976 Friuli, Italy earthquake and its principal aftershock.

II. A Method for Propagating Surface Waves From
Complex Seismic Source Regions to Teleseismic
Distances - Preliminary Results
D. G. Harkrider and P. Glover

The Representation Theorem allows one to extend near source calculations in laterally and vertically inhomogeneous regions to regional and teleseismic ranges using standard laterally homogeneous half-space codes. We define a surface which encloses the heterogeneity of the source region and exterior to which the medium can be represented by a plane stratified medium. As long as the surface is chosen so that the exterior radiation does not reflect back on the surface, then the Green's functions are those appropriate for the exterior region with no heterogeneities present. For a plane stratified half-space terminated at depth by a homogeneous half-space, the source containing surface can be a cylinder, i.e., canister, extending from the free-surface down into the terminating half-space. Various numerical techniques can then be used to determine the stress and displacement at a finite number of nodes on the surface. By spatially integrating the convolution of these nodal quantities with the appropriate surface wave Green's functions for ring sources in the laterally homogeneous region, we can obtain synthetic Rayleigh and Love waves for arbitrarily complex sources.

An example of the technique is shown in Figure 1. The nodal displacement-stress values were calculated at Del Mar Technical Associates and the results were for a joint AFOSR project. The synthetics shown in the figure are the vertical Rayleigh wave displacements due to a vertical point source at a depth of .4 km in a homogeneous half-space at a range of 300.1 km. The nodal displacements and stresses are calculated for

the bottom and sides of a cylindrical canister of radius 2.1 and vertical extent of 2.1 kms. The vertical force is located on the axis with a band limited δ function history. The frequency range is .01 - 2.0 hertz.

The nodal values were calculated by two very different techniques. The SWISS code is a finite element code capable of calculating displacements and stresses in a vertically and laterally inhomogeneous medium. For practical purposes the lateral range is restricted to no more than five (5) source depths in this problem. The PROSE code is a full (ω - k) numerical integration solution to a source and receiver in a plane layered viscoelastic half-space. The two nodal value results are combined with ring source surface wave Green's functions, which propagate the values from the canister to receiver and are calculated by the plane layered surface wave code HARK.

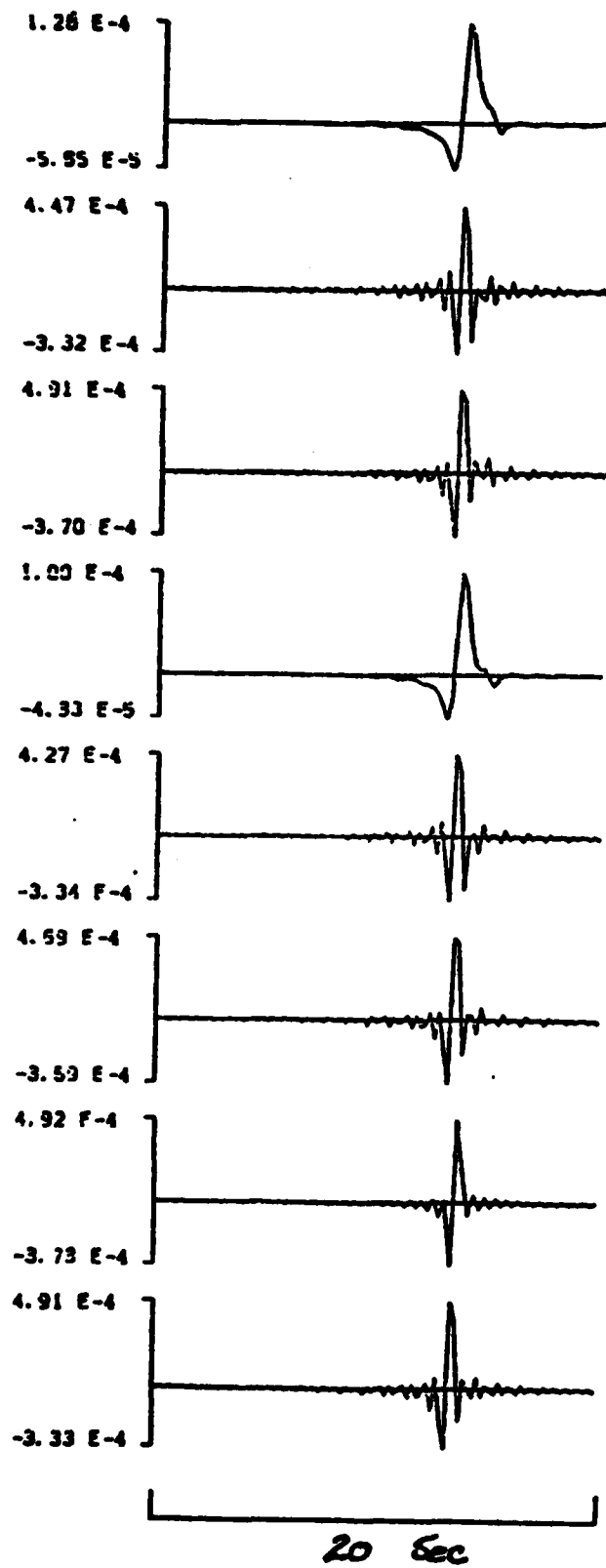
The resultant Rayleigh waves due to the bottom, side and total canister nodes are shown in the figure. The bottom two traces are PROSE and HARK vertical displacement calculations at a range of 300.1 km from the vertical point force. HARK generates only the Rayleigh wave while PROSE includes the direct body waves which at this range are negligible compared to the Rayleigh wave.

The comparison between signatures of PROSE-HARK, SWISS-HARK, and HARK is very good. This is due to the fact that propagation over the major part of the path is given by HARK calculations. The peak amplitude values of PROSE-HARK, PROSE and HARK are in excellent agreement. The choice of a band limited delta function source history is a very severe test of the technique in that a slight shift of phase can give differences on the order of 10% in time domain side lobe amplitudes,

i.e., the time spacing misses the narrower side lobe peak values. The differences between SWISS and PROSE as seen in SWISS-HARK and PROSE-HARK amplitude comparisons are not unexpected considering the differences in technique.

Earlier we stated that as long as the exterior reflected energy on the source enclosure is negligible, then the exterior Green's functions should be those appropriate for the propagation medium. As a test of this, we coupled the above canister driving functions, i.e., nodal displacements and stresses for a vertical point force in a simple half-space, to the Rayleigh Green's functions for a multilayered crust-mantle model of the western U.S., CIT 109. We felt that the negligible reflection criteria would easily be met in this case since the surface layer of CIT 109 was the same elastic medium as the interior source region and the nearest reflector was at the bottom of the 14 km thick surface layer, a distance of almost 12 kms from the canister bottom.

The results are shown on Figures 2 and 3 at a range of 1500 km with a WWSSN-LP instrument and without. The comparison of the direct calculation HARK with the PROSE driving function result as seen through the long period instrument is excellent both in absolute amplitude and shape. A similar comparison with SWISS-HARK, Figure 3, is outstanding especially before and after the maximum peak to trough amplitude. The two signals are vertically indistinguishable when overlayed.



Bottom Prose-Hark

Side Prose-Hark

Sum Prose-Hark

Bottom Swiss-Hark

Side Swiss-Hark

Sum Swiss-Hark

Prose

Hark

Figure 1

Vertical Pt. Force ; CIT109 Crust-Mantle

$R = 1500 \text{ km}$

No Q⁻¹

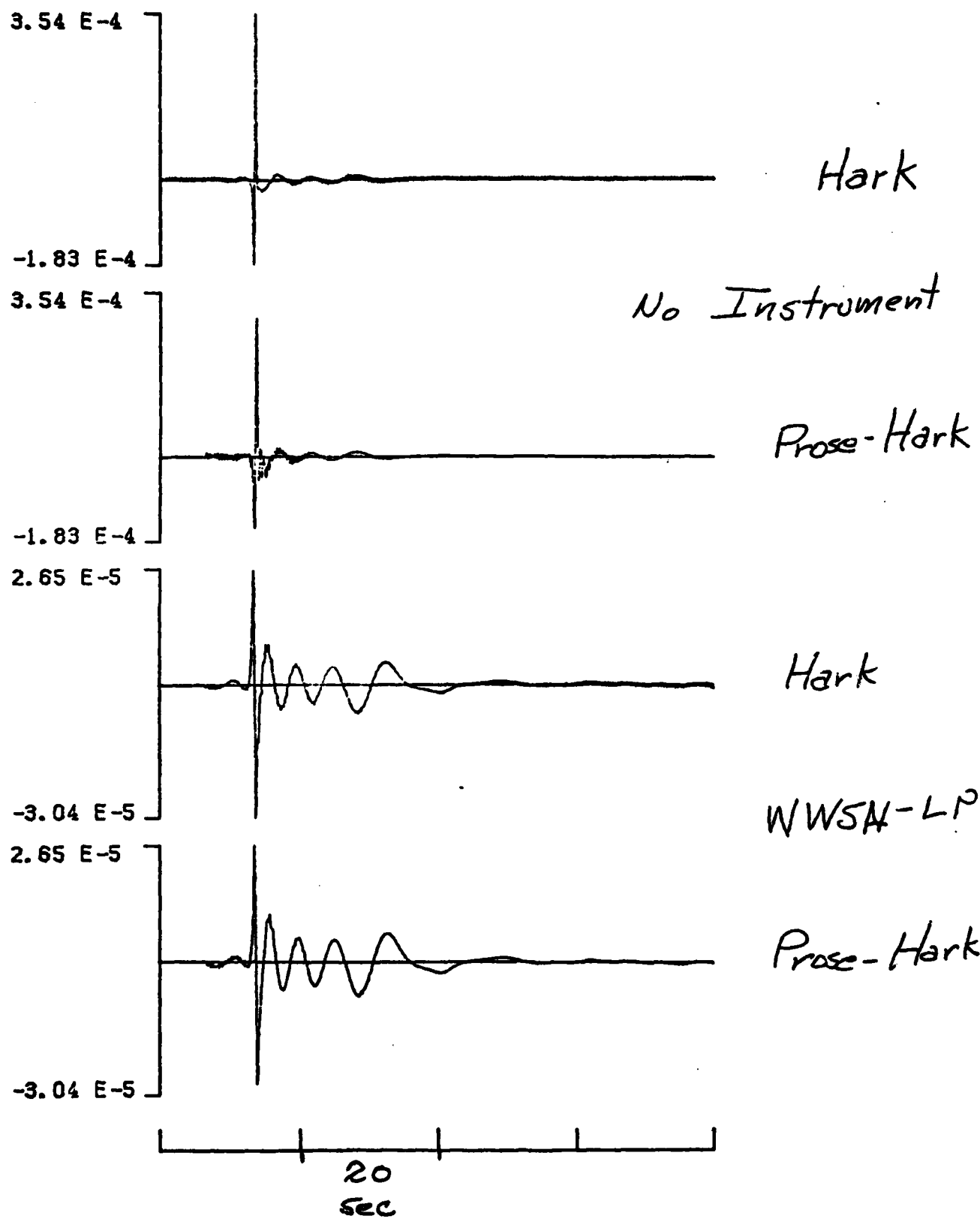


Figure 2

3.54 E-4

-1.83 E-4

3.54 E-4

-1.83 E-4

2.61 E-5

-3.04 E-5

2.61 E-5

-3.04 E-5

Hark

No Instrument

SWIS-Hark

Hark

NWSN-LP

SWIS-Hark

20 Sec

Figure 3

MODELING THE LONG-PERIOD BODY-WAVES
FROM SHALLOW EARTHQUAKES AT REGIONAL RANGES

By

D. V. Helmberger

G. R. Engen

Seismological Laboratory
California Institute of Technology
Pasadena, California 91125

ABSTRACT

A procedure for modeling P and PL waves at ranges 1 to 12 degrees is presented. Following the experience gained by modeling explosions, Helmberger (1972), we demonstrate that these long period phases are adequately treated by a single crustal layer for most of Western United States. After generating the Green's functions at the various ranges for the three fundamental dislocation types, we need only construct linear combinations of these vectors to represent any arbitrary oriented earthquake. The waveform patterns produced from the various fault types are quite diagnostic with the dip-slip orientations showing a strong ringing nature which is caused by the vertical SV-lobes. To test the usefulness of this technique we construct synthetics for some well studied west coast earthquakes where the orientation, time history, and moment have been determined independently. Comparing the predicted seismograms with observations

we find good agreement in waveshapes and amplitudes.

INTRODUCTION

In recent years, our understanding of earth structure and of earthquakes has increased substantially because of our increased ability to interpret seismograms. Much of this progress can be directly attributed to the development of fast techniques for constructing synthetic seismograms where source effects and propagational distortions are treated as separate effects. Following the procedures outlined in Fukao (1971) and Langston and Helmberger (1975) we are able to model the body phases from shallow earthquake sources as distributed shear dislocations with considerable success at teleseismic ranges where the reflected phases from the surface, pP, sP etc., are used to great advantage. Unfortunately, only magnitudes between 6 and 7 are sufficiently large to be well recorded by the WWSSN global network at ranges greater than 30 degrees. Once the source parameters are obtained by modeling the teleseismic results we can treat the source as known and use the observations from 15 to 30 degrees to study the upper-mantle structure, for example see Burdick and Helmberger (1978). Unfortunately, these size earthquakes produce SH waves that are off-scale at triplication distances. Thus, one must use magnitudes between 5 and 6 to study upper mantle shear structure with only rough estimates of the source parameters, see Helmberger and Engen (1974). Secondly, these smaller events are far more abundant geographically and of much importance tectonically. In this paper we present a technique for using a combination of P_n and PL phases

recorded at regional distances in the determination of source parameters for these moderate size events.

One of these smaller earthquakes, Truckee, $m = 5 \frac{3}{4}$, has been studied by numerous authors. From first-motion studies, it was determined to be a strike-slip event, striking N 44° E and dipping 80° SE, (Tsai and Aki, 1970). They found the moments of 1. and $.83 \times 10^{24}$ dyne-cm respectively from the Love and Rayleigh wave data. This event was also used by Burdick (1978) to study the upper mantle and, consequently, modeled at teleseismic distances. He used a triangular shape with $\delta t_1 = 1$ and $\delta t_2 = 2$ secs and a moment of $.6 \times 10^{24}$ dyne-cm to model the short and long period waveforms. Unfortunately, only a few long period body waves can be seen beyond 30 degrees so that his moment estimates are weak statistically. On the other hand the surface waves are clear and on-scale for ranges greater than 10 degrees, see Fig. 1. Thus, we will assume Tsai and Aki (1960) moment estimates and Burdick's time functions and predict the P_u and PL waveshapes and amplitudes at all the stations less than 12 degrees to test the usefulness of our technique.

We will be concerned with the beginning portion of the seismograms, essentially that portion of the record that has apparent velocities greater than the shear waves. At the start of the record the motions are completely dominated by the P-waves (P_u) and moving back into the record the motion contains progressively more SV

contributions (PL). We will call this wave group P_{nl} for brevity which would include the first 2 minutes of record in Fig. 1 as an example.

P_{nl} is polarized mostly in the vertical plane as can be seen in Fig. 2 where a naturally rotated motion is recorded. In general, we find that the relative strengths of the NS and EW components can be accurately estimated from the geometry which helped motivate this study. A display of the radial components found by either a summation of the EW and NS motions or by projection are given in Fig. 3. Note that the amplitudes at the nodal stations, BOZ and TUC, are relatively small and that the polarities of the P_n 's are in agreement with the focal mechanism. We will be primarily interested in modeling the vertical and radial motions at these ranges.

SYNTHETIC P_{nl}

We will assume that earthquakes can be represented by a point shear dislocation and that the earth can be treated by a single layer (crust) over a halfspace (mantle); both assumptions are over-simplifications but as we will see worth consideration as viable models at long periods. The solution in cylindrical coordinates for a point shear dislocation (double couple) situated in a whole space is discussed at length by Harkrider (1976) and Helmberger and Harkrider (1979). Using generalized ray expansions in conjunction with the

Cagniard-deHoop technique we express the vertical displacement as

$$w(r, \alpha, \theta, t) = \frac{M_0}{4\pi\rho_0} \frac{d}{dt} \left[D(t) * \sum_{j=1}^3 A_j w_j \right] \quad (1)$$

where

$$\begin{aligned} w_j(t) = & \sqrt{\frac{2}{r}} \frac{1}{\pi} \left[\frac{1}{\sqrt{t}} * \sum_{i=1}^n \text{Im} \left(\frac{\sqrt{p}}{\eta_a} C_j(p) R_{NZ}(p) \tau_i(p) \frac{dp}{dt} \right)_1 \right] \\ & + \sqrt{\frac{2}{r}} \frac{1}{\pi} \left[\frac{1}{\sqrt{t}} * \sum_{i=1}^n \text{Im} \left(\frac{\sqrt{p}}{\eta_s} S V_j(p) R_{NZ}(p) \tau_i(p) \frac{dp}{dt} \right)_1 \right] \end{aligned} \quad (2)$$

with

p = ray parameter

$$\eta_v = \left(\frac{1}{v^2} - p^2 \right)^{1/2}$$

a = compressional velocity

s = shear velocity

ρ = density

M_0 = seismic moment

$D(t)$ = far-field time history

and with the orientation constants given by:

$$A_1(\theta, \lambda, \delta) = \sin \theta \cos \lambda \sin \delta + \frac{1}{2} \cos \theta \sin \lambda \sin 2\delta$$

$$A_2(\theta, \lambda, \delta) = \cos \theta \cos \lambda \cos \delta - \sin \theta \sin \lambda \cos 2\delta$$

$$A_3(\theta, \lambda, \delta) = \frac{1}{2} \sin \lambda \sin 2\delta$$

where

θ = strike from the end of the fault plane

λ = rake angle

δ = dip angle

The vertical radiation patterns are defined by

$$C_1 = -p^2$$

$$SV_1 = -cpn_B$$

$$C_2 = 2cpn_a$$

$$SV_2 = (n_B^2 - p^2)$$

$$C_3 = (p^2 - 2n_a^2)$$

$$SV_3 = 3cpn_B$$

$$\text{where } c = \begin{cases} +1 & z > h \\ -1 & z < h \end{cases}$$

We are using the same notation and conventions used by Langston and Helmberger (1975). Note that W is positive for downward motions. The summation is over contributing rays where the function $\pi_1(p)$ defines the product of all transmission and reflection coefficients along the path from the source to the receiver. The function $R_{NZ}(p)$ is defined by $R_{PZ}(p)$ or $R_{SZ}(p)$ depending on the mode of propagation upon arrival at the receiver, with

$$R_{PZ} \equiv \frac{2n_a(n_B^2 - p^2)}{s^2 R(p)}$$

$$R_{SZ} \equiv \frac{n_a n_B}{s}$$

$$R(p) \equiv (n_B^2 - p^2)^2 + 4p^2 n_a n_B$$

The radial displacements, Q_i , are obtained by replacing R_{PZ} and R_{SZ} by R_{PR} and R_{SR} defined by

$$R_{PR} = \frac{-4n_a n_B p}{s^2 R(p)}$$

$$R_{SR} = \frac{2n_B(n_B^2 - p^2)}{s^2 R(p)}$$

The above high frequency solution has many advantages in model studies due to its simplicity. However, for small r , one must use more terms in the expansion or the full solution, see Helmberger and Harkrider (1979). Since we are primarily interested in regional distances, $100 \text{ km} < \Delta < 1400 \text{ km}$, we can neglect the near-field effects for the moderate sized events of interest.

In the remaining portion of this section we discuss the motions produced by the three fundamental faults. Normally, we generate and save the $W_j(t)$ and $Q_j(t)$ specified by expression (2) and construct various solutions for arbitrary $(\theta, \lambda, \delta)$ and assumed time history. For presentation it is convenient to perform the convolution indicated by (1) which more clearly displays the broad-band nature of the motions. Thus, we will assume the $\delta(t)$ is specified by a symmetric trapezoidal shape with a 1.5 sec duration which is about the expected period for a moderate sized event. We will adopt the same units used by Helmberger and Malone (1975), namely if we express r in km, time in sec, ρ_0 in gm/cm^3 , velocity in km/sec , M_0 in dyne-cm and displacements in cm we must include a factor of (10^{20}) for unit conversion. In what follows we assume that $M \times 10^{-20} / 4\pi\rho_0 = 1$ or $M_0 = 4\pi\rho_0 \times 10^{20}$ dyne-cm. The assumed crustal model is given in Table 1.

Constructing the solution by summing the rays as described by equation (2) is tedious in that many rays are required to produce reliable synthetics at the larger ranges. To insure stability, ray

files containing increasing numbers of multiples are computed sequentially where the output is monitored per multiple. An example calculation is displayed in Fig. 4 to show the convergence with the addition of multiples as well as to introduce some geometrical considerations. Since the strengths and polarities of the various rays are strongly influenced by the vertical radiation patterns, $C_j(p)$ and $SV_j(p)$, we have included these patterns above each column. In the strike-slip (SS) case, the direct P and diffracted P along the free surface, included in the direct S generalized ray, are in phase but out of phase in the dip-slip (DS) case. Note that due to our limited time window we do not include the direct S pulse which at this range would be embedded in the Rayleigh wavetrain. The rays appropriate for reflections are leaving the source near the horizontal and because of the position of the P-loops produce strong reflections for SS events and weak reflections in the DS case. The opposite is true with respect to the headwaves. The strong downswing in the DS case a few seconds after the onset is produced by the phase sPP. Thus, the source depth is a major variable in the DS wavetrain. Note that the beginning portion of P is stable with the addition of multiples but that the later portion, PL part, is more complex requiring large numbers of mixed P-SV mode rays for its definition. These synthetics were generated by summing all 4094 rays as a check against a much smaller ray set which contains kinematic redundancies. For instance only 304 rays were used for the fifth bounce instead of 3072. Taking advantage of these symmetries allows for relatively inexpensive

seismograms, see Hron and Kanasewich (1971).

Another strategy for understanding these motions is to split these ray contributions into those starting upward as opposed to downward at the source as indicated in Fig. 5. The summation process suppresses the short periods in the SS case while emphasizing the long periods. The opposite effect is produced in the DS case. Changing the source depth shifts the upgoing trace relative to the downgoing trace and produces a dramatic effect in the DS case as displayed in Fig. 6. In fact, a good approximate seismogram for $h = 4$ and 16 can be obtained by simply shifting the $h = 8$ traces without recomputing the rays.

We can also use these split Green's functions to simulate directivity by assuming different source histories for upgoing versus downgoing traces; that is, perform the convolution given by (1) before summing the traces. This procedure neglects the dependence of directivity on ray parameter which is probably justified because the long period waveshape is almost entirely controlled by refracted energy which leaves the source with the same ray parameter.

A close examination of Fig. 6 reveals that increasing h has the effect of increasing the separation between P_n and direct P or increasing dispersion. A similar effect is produced by increasing the distance as can be seen in Figs. 7, 8 and 9 where we display P_{nL} as a

function of range.

The broad-band displacements given in Figs. 7, 8 and 9 suggest that the long period behavior is independent of the short periods at the larger ranges. Constructing synthetics appropriate for the WWSS long period and short period systems further emphasizes this independence as displayed in Fig. 10. Thus, long period synthetics (LP) are dominated by the interference of head waves while the short period synthetics (SP) are controlled mostly by interacting moho reflections.

APPLICATION TO REGIONAL DATA

In this section we will give a brief comparison of some of the regional observations from well-studied earthquakes with theoretical predictions. That is we will suppose that the fault parameters such as fault orientation, moment and time histories are adequately determined by teleseismic studies and perform the summations indicated by expressions (1) and (2) to generate the synthetic response. We will be primarily concerned with the Truckee earthquake which appears to have produced a fairly complete WWSS data set as discussed earlier.

Using the fault parameters reported on by Tsai and Aki (1970) and Burdick (1978) we generated the synthetics in Figs. 11 and 12. But, since the teleseismic data has been attenuated by the Earth and modeled

accordingly we would expect to see more short period motions in the regional records. Thus, to help equalize the data set we have applied a smoothing operator by convolving both data and synthetics with a two sec. triangle. This operator has a negligible effect in the synthetics but does remove some of the high frequency from the observed records which can be seen by comparing the waveforms in Fig. 3 with Figs. 11 and 12. Note that we did not generate the synthetics at the proper (Δ), but simply used the nearest Green's function in this preliminary analysis. This approximation is probably reasonable at the larger ranges but becomes questionable at the nearer ranges such as GSC. In general, the agreement is surprisingly good except perhaps at the nodal stations where the data is contaminated by noise. Note that the amplitude at TUC is a half order of magnitude down from ALQ and that the vertical record is mostly a noise sample which has been included here for completeness. The only WWSS records not shown here are those from BKS which were off-scale.

The predicted waveforms confirm the strike-slip nature of this event. If we scale the amplitude of each synthetic with the corresponding observed record and take the average we obtain a moment of $.97 \times 10^{24}$ ergs which is within 15% of the determination by Tsai and Aki (1970) and well within their error estimate.

Another example of a well studied strike-slip event is the Borrego Mountain earthquake of 1968, Allen et al. (1968). This event

produced an excellent set of teleseismic waveforms which have been modeled in great detail by applying a waveform inversion technique (see Burdick and Mellman, 1976). Their results indicate three individual events are involved with the first dominant event having a moment of 1.1×10^{26} ergs and a triangular source history specified by a .4 sec rise time followed by a 4.5 sec decay. Because of the large moment no surface waves were recoverable from WWSSN stations in the United States and only one P_{NL} waveform is completely on-scale. The observations from this station are given in Fig. 13 and should be viewed with some caution because of its proximity to a P-SV node (6 degrees off) which is the reason for its existence. Nevertheless, the predicted waveform and amplitude is quite good. Adding in the aftershocks proposed by Burdick and Mellman (1976) produced negligible changes in these synthetics.

For our final comparison, we chose the Oroville earthquake which has a normal mechanism ($\theta = 180^\circ$, $\delta = 65^\circ$, $\lambda = -70^\circ$), see Langston and Butler (1976). In general, shallow normal events and thrust events are not as well constrained by teleseismic data as strike-slip events. The difficulty arises from the azimuthal symmetry in the P-waveforms where the direct P does not change signs and pP and sP are nearly equal strength and inseparable in time. Thus, the rake angle becomes indeterminant to some degree depending on the quality of the S-waveforms. In this situation the P_{NL} waveforms appear quite useful as displayed in Fig. 14 in that a rake near -90° fits the data quite

well.

DISCUSSION

It seems rather surprising that a single layer over a halfspace can explain the long period P_{nl} waveform and amplitude behavior as well as demonstrated in the previous section. However, after conducting a few numerical experiments on more complicated structures it becomes clear why this simplification works. First, if we examine the behavior of the reflection coefficients R_{pp} , R_{ps} and R_{sp} for various assumptions about the crust-mantle boundary we find that adding a transition layer of up to 10 km does not drastically alter the long period behavior at post-critical angles. The numerical experiments presented by Shaw and Orcutt (1979) document this conclusion. At larger ray parameters or apparent crustal velocities a transition zone has more of an effect especially at small ranges and this may be the reason for the mismatch at GSC and DUG, see Figs. 11 and 12. Another stabilizing feature of P_{nl} is that we expect the multiple reflections to occur either near the source or near the receiver depending on the slopes of the moho. That is shooting up-dip, crust thinning towards receiver, bunches the reflections near the receiver and shooting down dip bunches the reflections near the source, see Hong and Helmberger (1978). Thus variations in the crustal thickness along the path is only sampled by the headwaves

which are not likely to be very sensitive. Large crustal changes such as proposed by Eaton (1963) under the Sierra Nevada Mountains may produce significant distortions and should be investigated further both theoretically and observationally.

Variations in crustal thickness and moho velocity does, obviously, alter the absolute P times and relative times between P_n and PL as discussed by Helmberger (1973) and York and Helmberger (1973). Note that in the comparisons displayed in Figs. 11 and 12 we shifted the theoretical shapes by the (δt 's) given in Fig. 3. The high P velocity appropriate for the Colorado plateau causes the negative (δt) or the early arrival time at ALQ relative to TUC. Note that observations to the northwest, namely COR and LCN, contain much more short period energy than do waveforms at other azimuths. One possible explanation is that the upper mantle contains a positive gradient along some azimuths which increases the frequency content of the individual headwaves, for example see Hill (1971). On the other hand, the same effect could be caused by differential attenuation along lines or perhaps source directivity. A study of the LRSM and WWSSN array measurements for the many events that crisscross this region could sort out these effects; such a study is in progress.

In conclusion, we have demonstrated that long period P_{nL} from earthquakes can be modeled quite successfully by assuming that: (1) the earth is a layer over a halfspace and (2) earthquakes can be

represented by point shear dislocations modeled by three fundamental fault types, strike-slip, dip-slip, and 45 degree dip-slip. The six components $W_{1,2,3}$ and $Q_{1,2,3}$ defined here can be used directly in inversion schemes of the type discussed by Mellman and Burdick (1976) or they can be used in moment tensor notation as discussed by Stump (1979).

ACKNOWLEDGMENTS

This research was supported by the Advanced Research Projects Agency of the Department of Defense and was monitored by the Air Force of Scientific Research under Contract No. F49620-77-C-0022. Contribution number 3393, Division of Geological and Planetary Sciences, California Institute of Technology, Pasadena, California 91125.

REFERENCES

- Allen, C. R. and J. M. Nordquist (1972). Fores shock, main shock and larger aftershocks of the Borrego Mountain earthquake, U.S. Geol. Surv. Prof. Paper 787, 16-23.
- Burdick, L. J. (1977). Broad-band seismic studies of body waves, Ph.D. Thesis, California Institute of Technology.
- Burdick, L. J. and D. V. Helmberger (1978). The upper mantle P velocity structure of the western United States, J. Geophys. Res., 83, 1699-1712.
- Burdick, L. J. and G. R. Mellman (1976). Inversion of the body waves of the Borrego Mountain earthquake to the source mechanism, Bull. Seism. Soc. Am., 66, 1485-1499.
- Eaton, J. P. (1963). Crustal structure from San Francisco, California, to Eureka, Nevada, from seismic refraction measurements, J. Geophys. Res., 68, 5789-5806.

Fukao, Y. (1971). Seismic body waves from surface faults, J. Phys. Earth, 19, 4, 271-281.

Harkrider, D. G. (1976). Potentials and displacements for two theoretical sources, Geophys. J. R. astr. Soc., 47, 97-133.

Helberger, D. V. (1972). Long-period body-wave propagation from 4° to 13°, Bull. Seism. Soc. Am., 62, 325-342.

Helberger, D. V. (1973). On the structure of the low-velocity zone, Geophys. J. R. astr. Soc., 34, 251-263.

Helberger, D. V. and G. R. Engen (1974). Upper mantle shear structure, J. Geophys. Res., 79, 4017-4028.

Helberger, D. V. and D. G. Harkrider (1978). Modeling earthquakes with generalized ray theory, Proceedings of IUTAM Symposium: Modern Problems in Elastic Wave Propagation, J.

Miklowitz and J. Achenbach (eds.), John Wiley and Sons, New York.

Helmberger, D. V. and S. D. Malone (1975). Modeling local earthquakes as shear dislocations in a layered halfspace, *J. Geophys. Res.*, 80, 4881-4888.

Hill, D. P. (1971). Velocity gradients and anelasticity from crustal body wave amplitudes, *J. Geophys. Res.*, 76, 3309-3325.

Hong, T. L and D. V. Helmberger (1977). Generalized ray theory for dipping structure, *Bull. Seism. Soc. Am.*, 67, 995-1008.

Eron, F. and E. R. Kanasewich (1971). Synthetic seismograms for deep seismic sounding studies using asymptotic ray theory, *Bull. Seism. Soc. Am.*, 61, 1169-1200.

Langston, C. A. and R. Butler (1976). Focal mechanism of the August 1, 1975 Oroville earthquake, *Bull. Seism. Soc. Am.*, 66, 1111-1120.

Langston, C. A. and D. V. Helmberger (1975). A procedure for modeling shallow dislocation sources, Geophys. J. R. astr. Soc., 42, 117-130.

Shaw, P. and J. Orcutt (1979). The influence of source parameters and crustal structure on PL propagation, Trans., AGU, 60, no. 46, 895.

Stump, B. W. (1979). Investigations of seismic sources by the linear inversion of seismograms, Ph.D. Thesis, University of California, Berkeley.

Tsai, Y. B. and K. Aki (1970). Source mechanism of the Truckee, California earthquake of September 12, 1966, B.S.S.A., 60, no. 4, 1199-1208.

York, J. E. and D. V. Helmberger (1973). Low-velocity zone variations in the southwestern United States, J. G. R., 78, no. 11, 1883-1886.

FIGURE CAPTIONS

Figure 1. Observation of the Truckee earthquake ($M = 5.7$) as recorded on a long period WWSS (30,90) instrument at Golden, Colorado.

Figure 2. Three component observation of the San Fernando earthquake recorded at ALQ, New Mexico, showing the motion to be almost entirely (P, SV) dominated.

Figure 3. Map of stations and event (indicated by the crossing fault plane lines). The numbers above the radial observations indicate the amplitudes ($\text{cm} \times 10^{-3}$) as measured peak-to-peak. The t 's are time delays, theoretical minus observed, to be discussed later in the text.

Figure 4. Vertical components of motion as a function of ray summation assuming a trapezoidal time function described by .5, .5, .5, for pure strike-slip and dip-slip orientations at $\Delta = 1000$ km.

Figure 5. Radial components of motion at $\Delta = 1000$ km in terms of upgoing, downgoing, and summed for trapezoidal time history (.5, .5, .5 sec).

Figure 6. Motions of all three types of faults at $\Delta = 1000$ km as a function of source depth. The numbers above each trace indicate the zero to peak amplitude in cm assuming $M_0 = 4\pi\rho_0 \times 10^{20}$ dyne-cm and trapezoidal time history (.5, .5, .5 sec).

Figure 7. Strike-slip synthetics as a function of range (Δ) assuming a trapezoidal time history (.5, .5, .5) and M_0 . The numbers indicate zero to peak amplitudes in cm.

Figure 8. Dip-slip synthetics as a function of range (Δ) assuming trapezoidal time history (.5, .5, .5) and M_0 . The numbers indicate zero to peak amplitudes in cm.

Figure 9. 45 degree dip-slip synthetics as a function of range (Δ) assuming trapezoidal time history (.5, .5, .5) and M_0 . The numbers indicate zero to peak amplitudes in cm.

Figure 10. The top traces are the radial displacements at $\Delta = 1000$ km. Middle set contain the results after convolving with the WWSSN short-period response and the bottom set the results after applying the long-period response.

Figure 11. Comparison of observed waveforms from the Truckee earthquake with synthetic predictions where the numbers above each trace indicate the maximum peak-to-peak amplitude ($\times 10$ cm). The assumed source parameters are: $M = .83 \times 10^{10}$ ergs, $\theta = 44^\circ$, $\delta = 80^\circ$, $\lambda = 0$, and triangular time history with $\delta t_1 = 1$. and $\delta t_2 = 2$. See Figure 3 for station locations.

Figure 12. Continuation of Truckee comparison.

Figure 13. Comparison of the Borrego Mountain observation obtained at GOL with synthetic prediction where the numbers above each trace indicate the maximum peak-to-peak amplitude ($\times 10^{-3}$ cm). The assumed source parameters are: $M_0 = 1.1 \times 10^{27}$ dyne-cm. $\theta = -45^\circ$, $\delta = 81^\circ$, $\lambda = 178^\circ$ and triangular time history with $\delta t_1 = .4$ and $\delta t_2 = 4.5$ sec.

Figure 14. Comparison of the observed P_{nl} at Pasadena on a long period (30,100) instrument and synthetics at various rake angles for the Oroville event. The numbers above each trace indicate the peak-to-peak amplitude in 10^{-3} cm. The assumed source parameters are: $M_0 = 5.7 \times 10^{24}$ ergs, $\theta = 180^\circ$, $\delta = 65^\circ$ and triangular time history with $\delta t_1 = 1.5$ and $\delta t_2 = 1.5$.

TABLE 1 - CRUSTAL MODEL

P _{VEC}	S _{VEC}	DENSITY	LAYER THICKNESS
6.2	3.5	2.7	3.2
8.2	4.5	3.4	

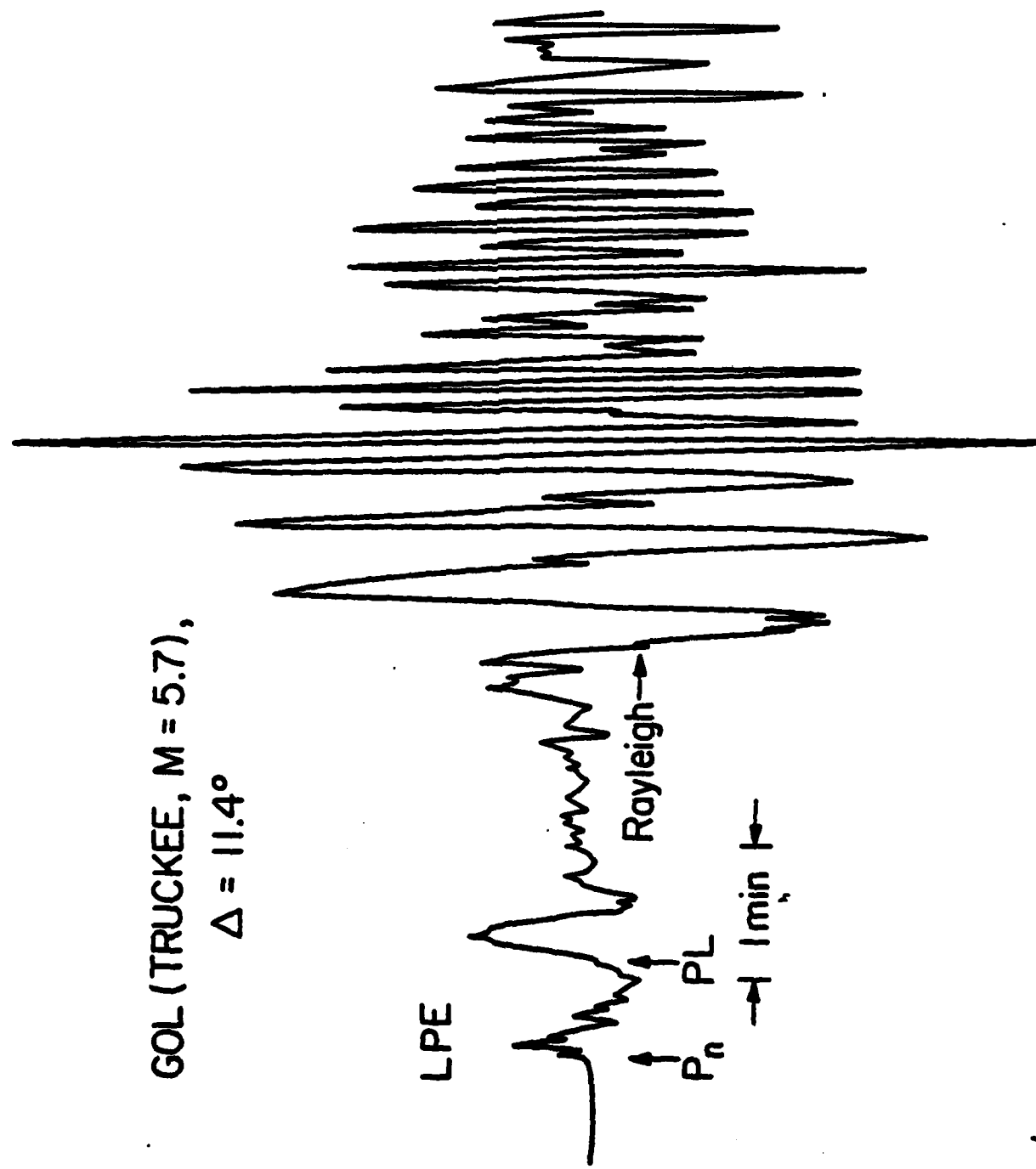


fig 1

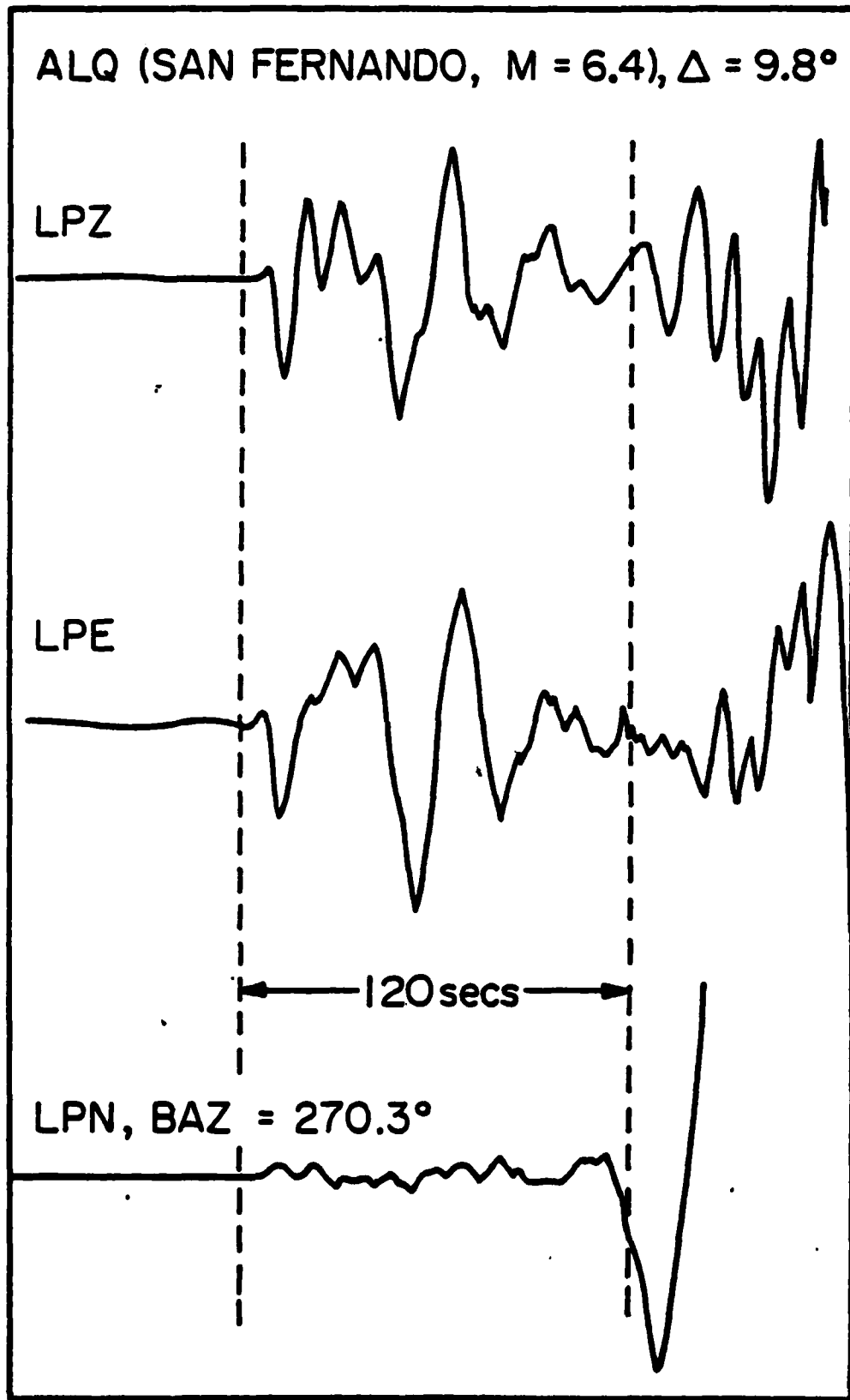


fig 2

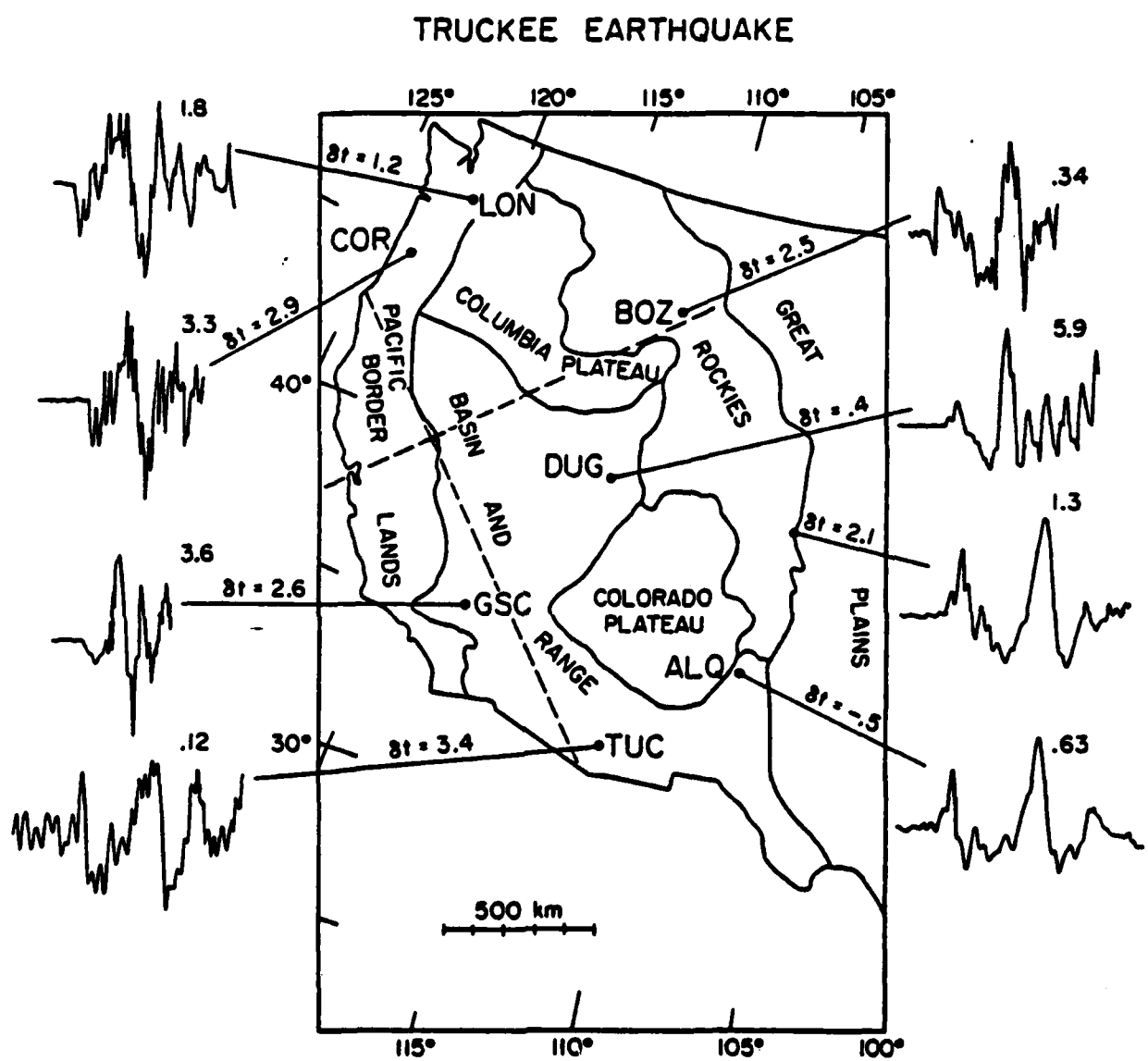


fig. 3

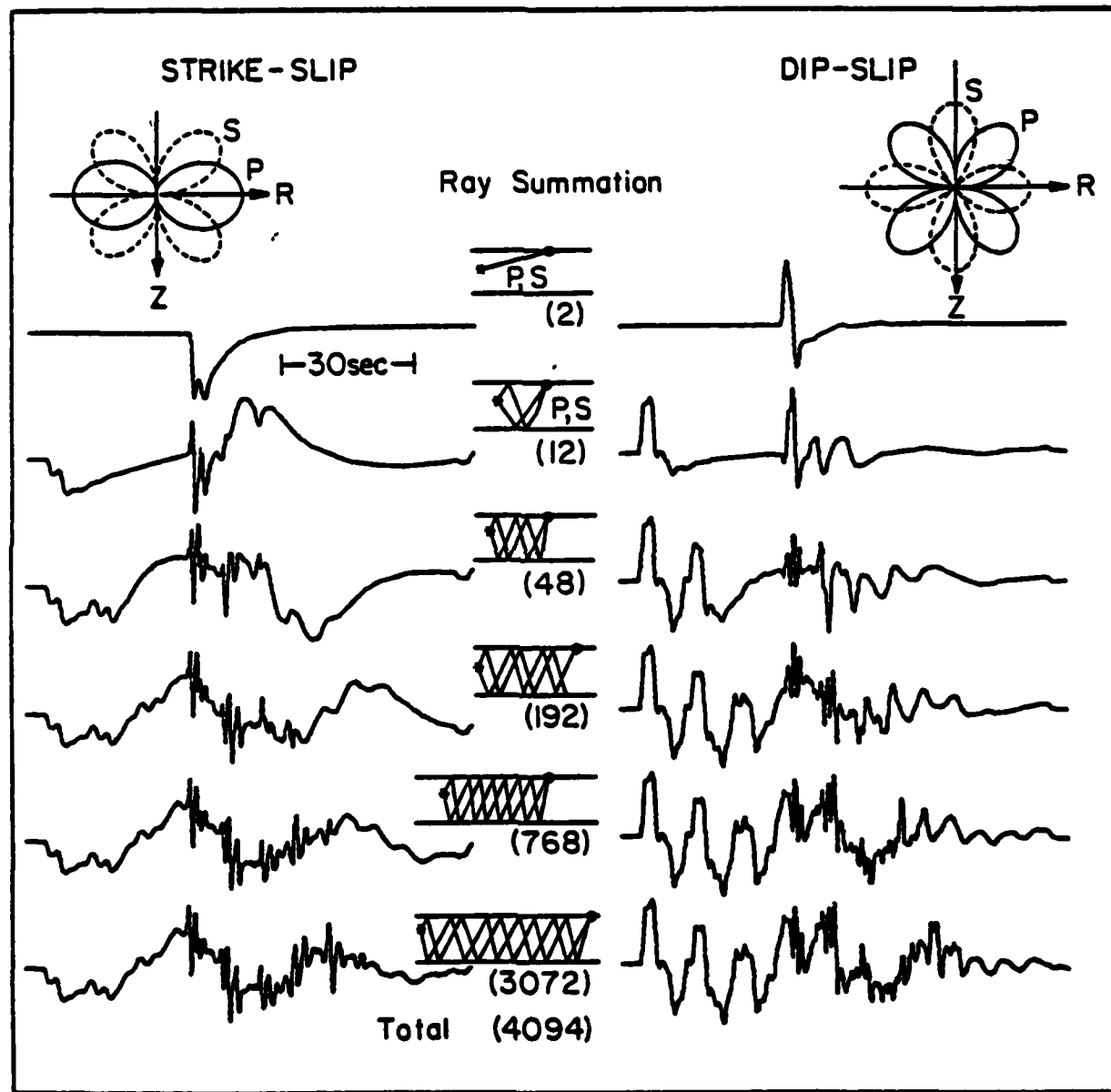


fig 4

STRIKE-SLIP

DIP-SLIP

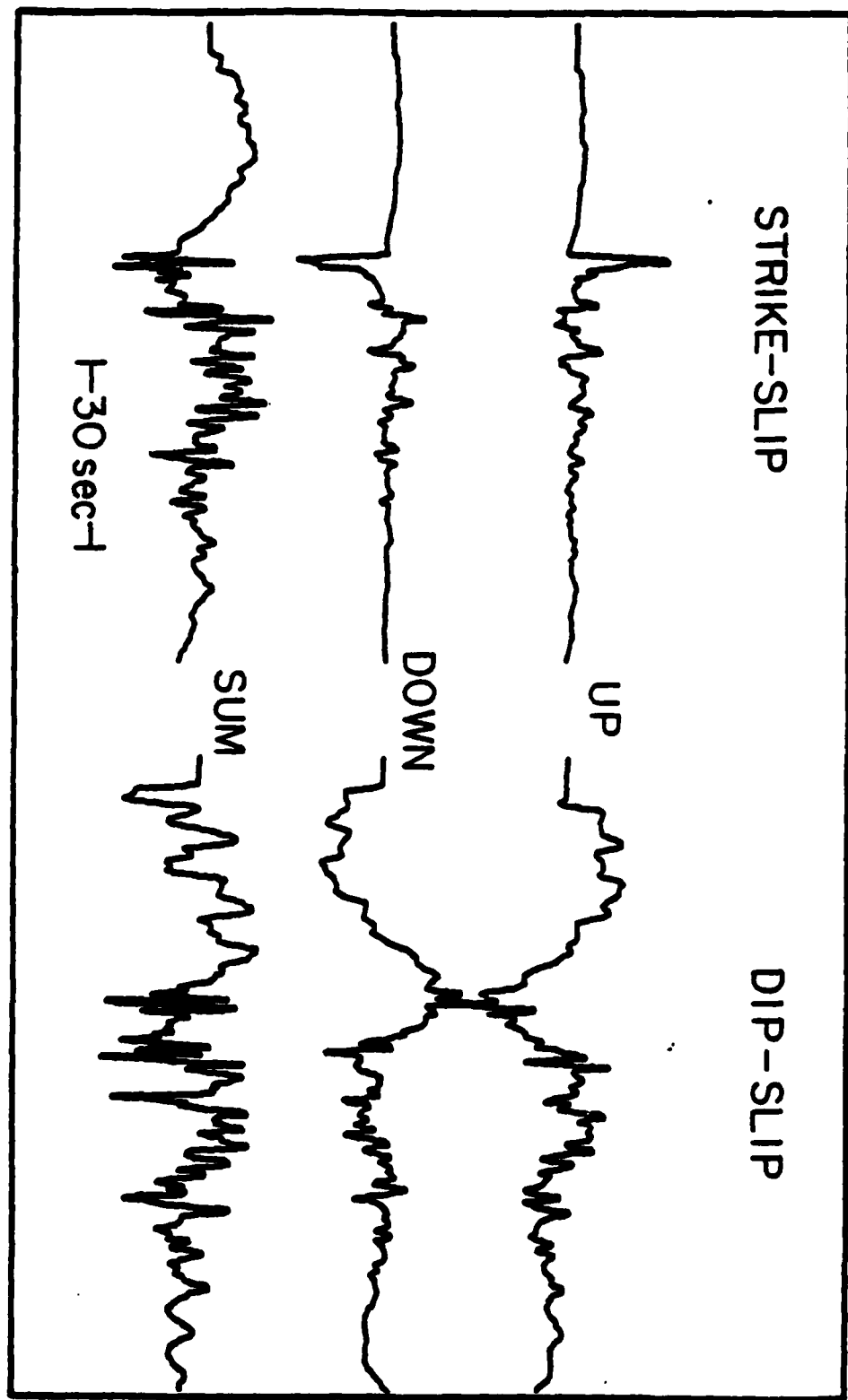


fig. 5

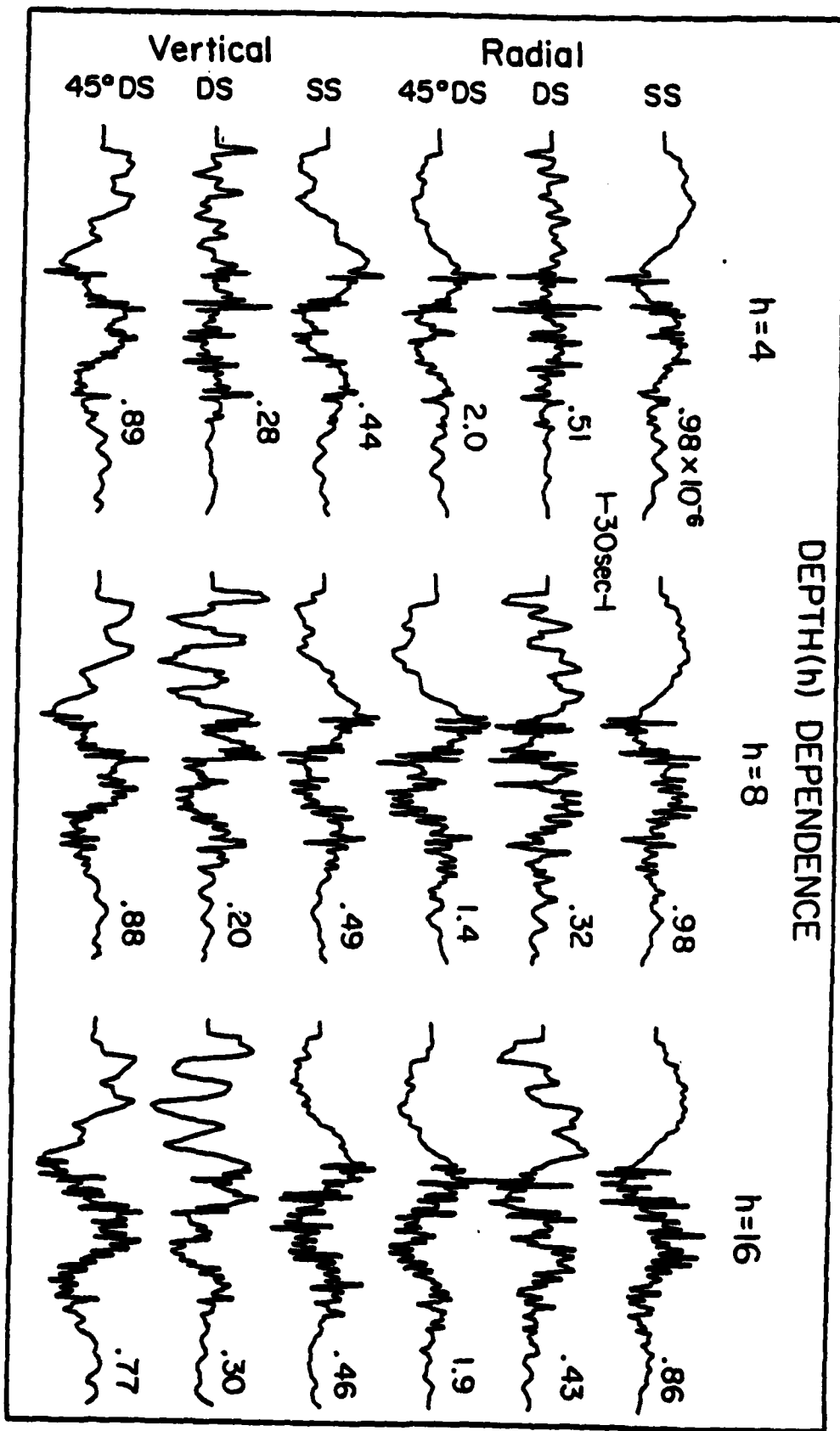


fig c

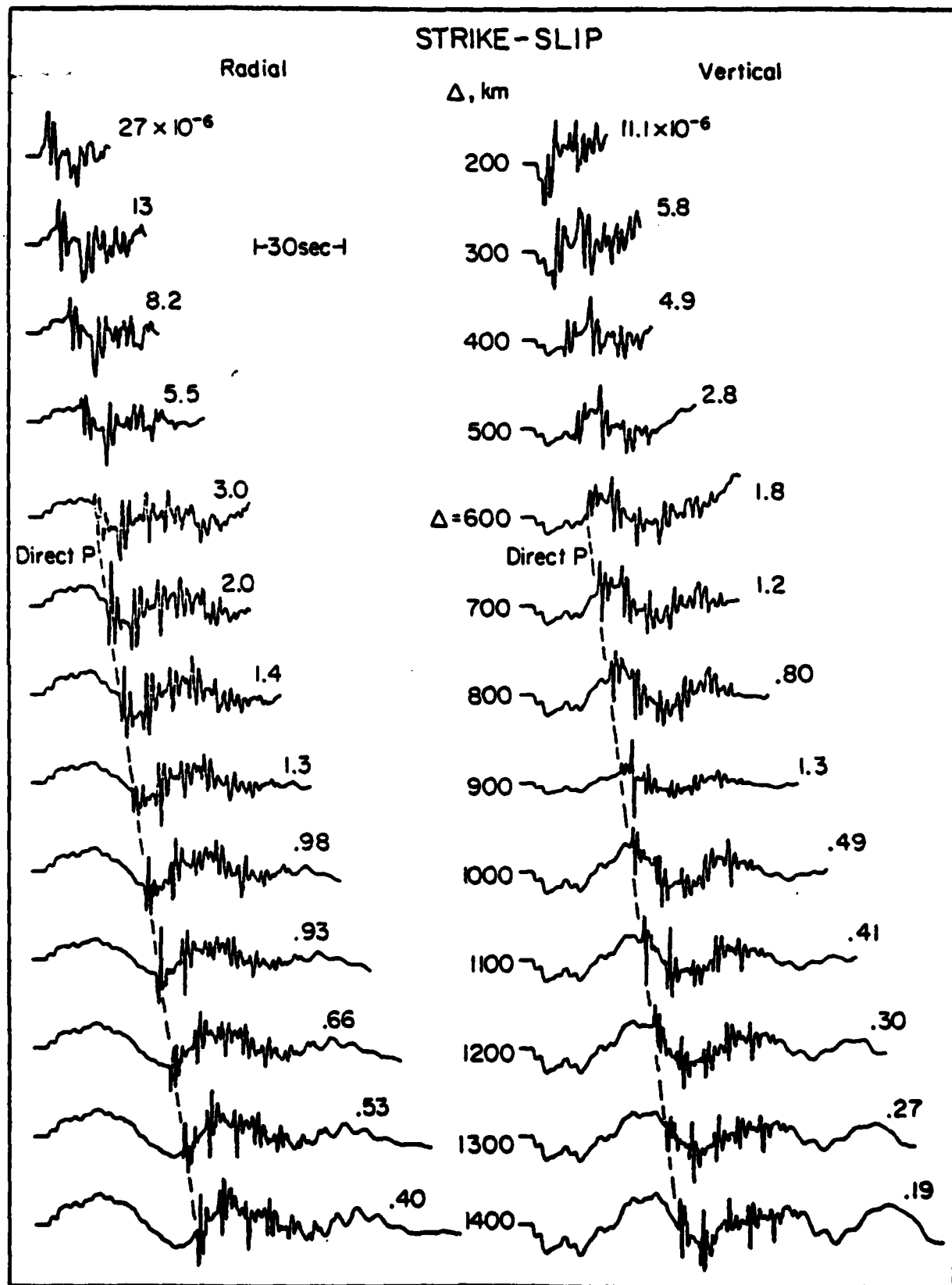


fig 7

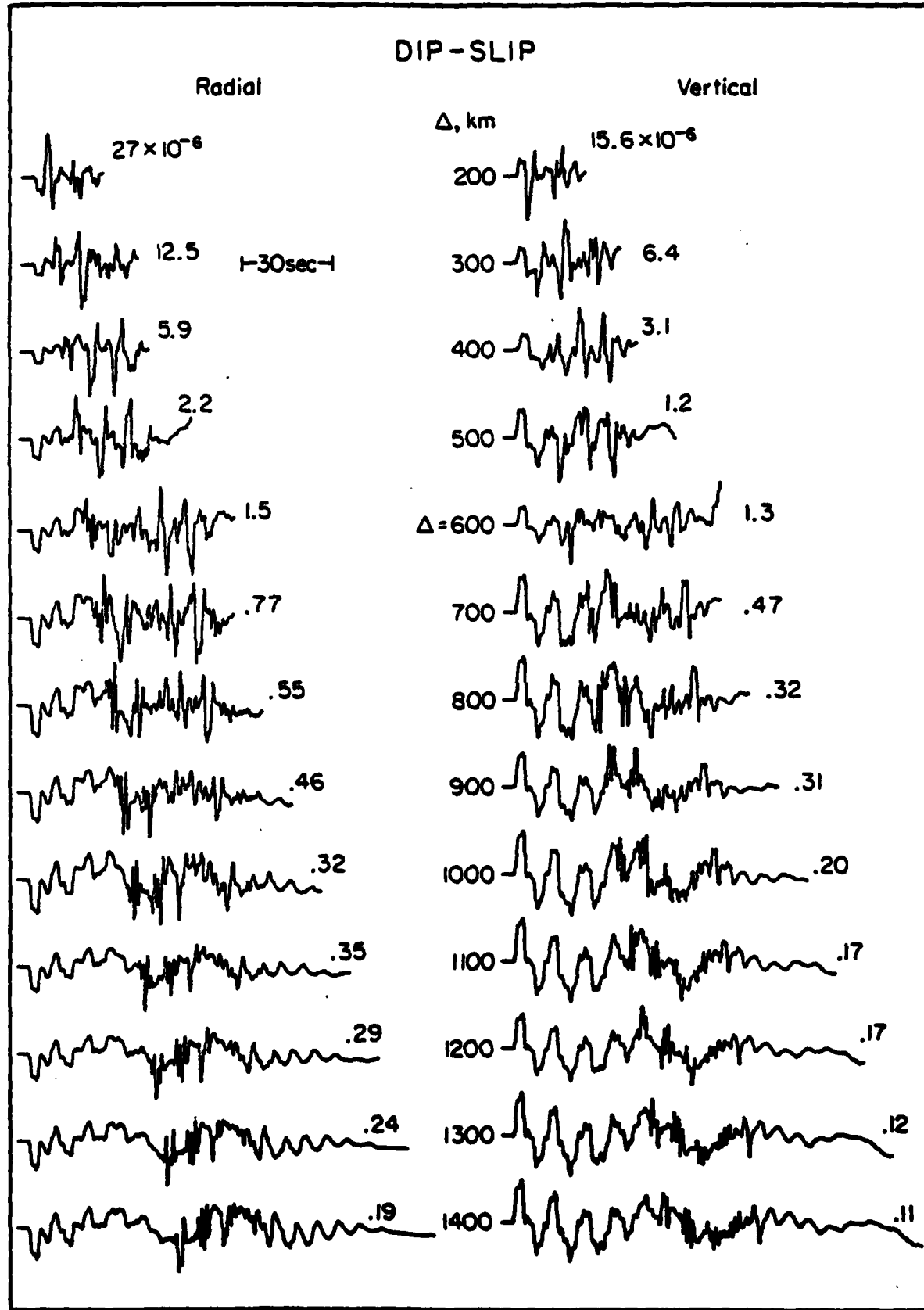


fig 8

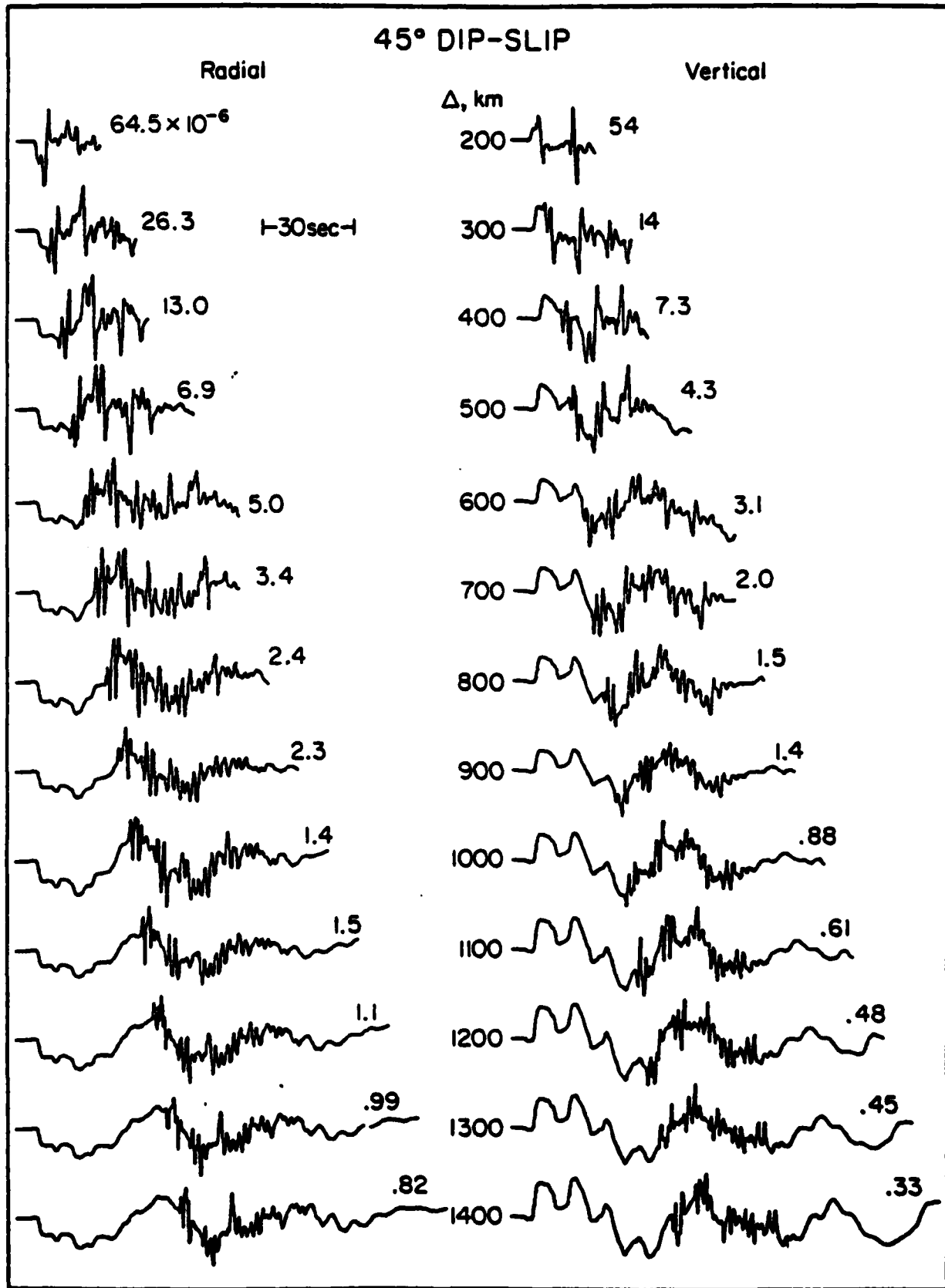


fig 9

STRIKE-SLIP

|-30sec-|

DIP-SLIP

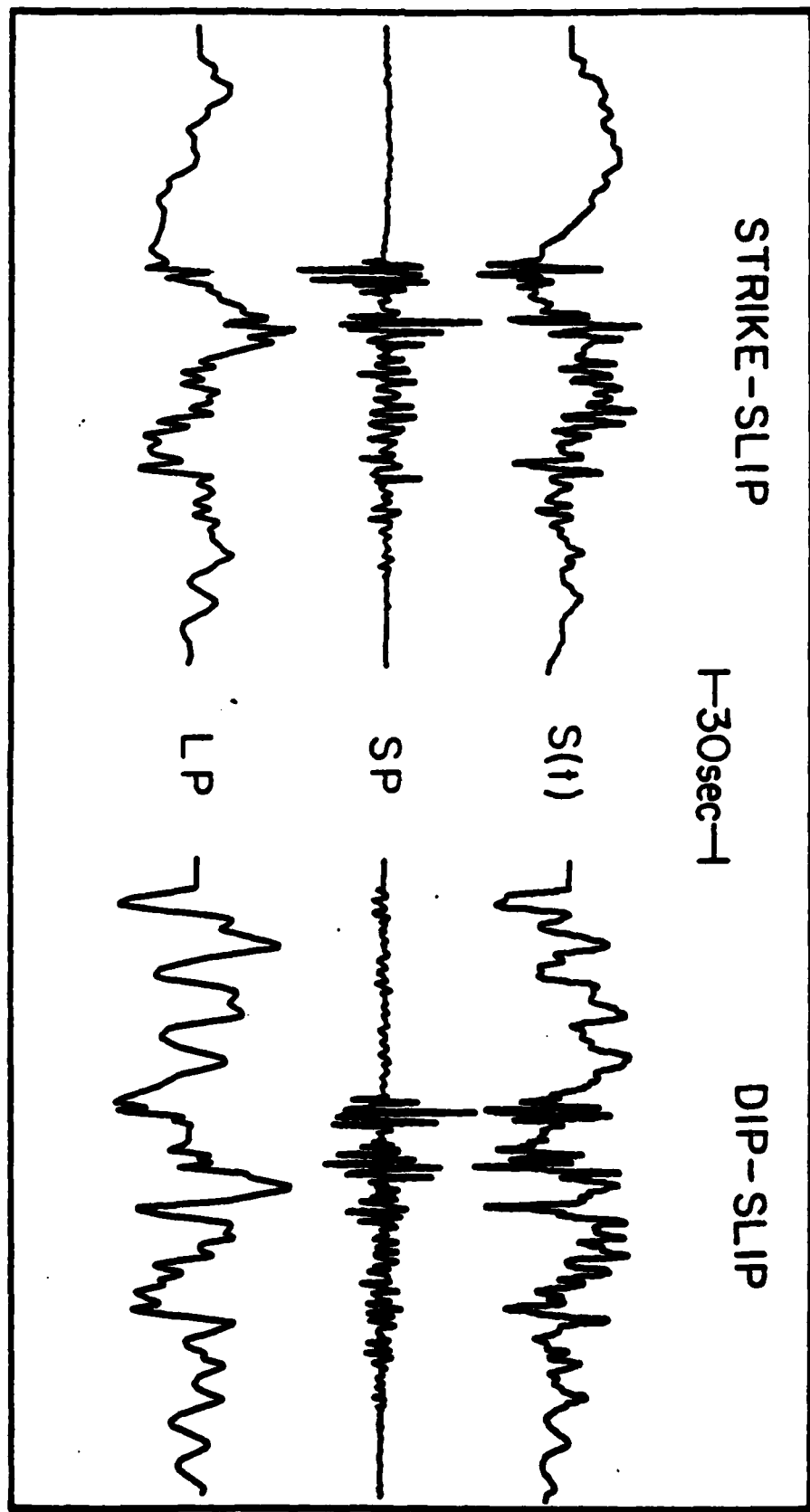


fig 10

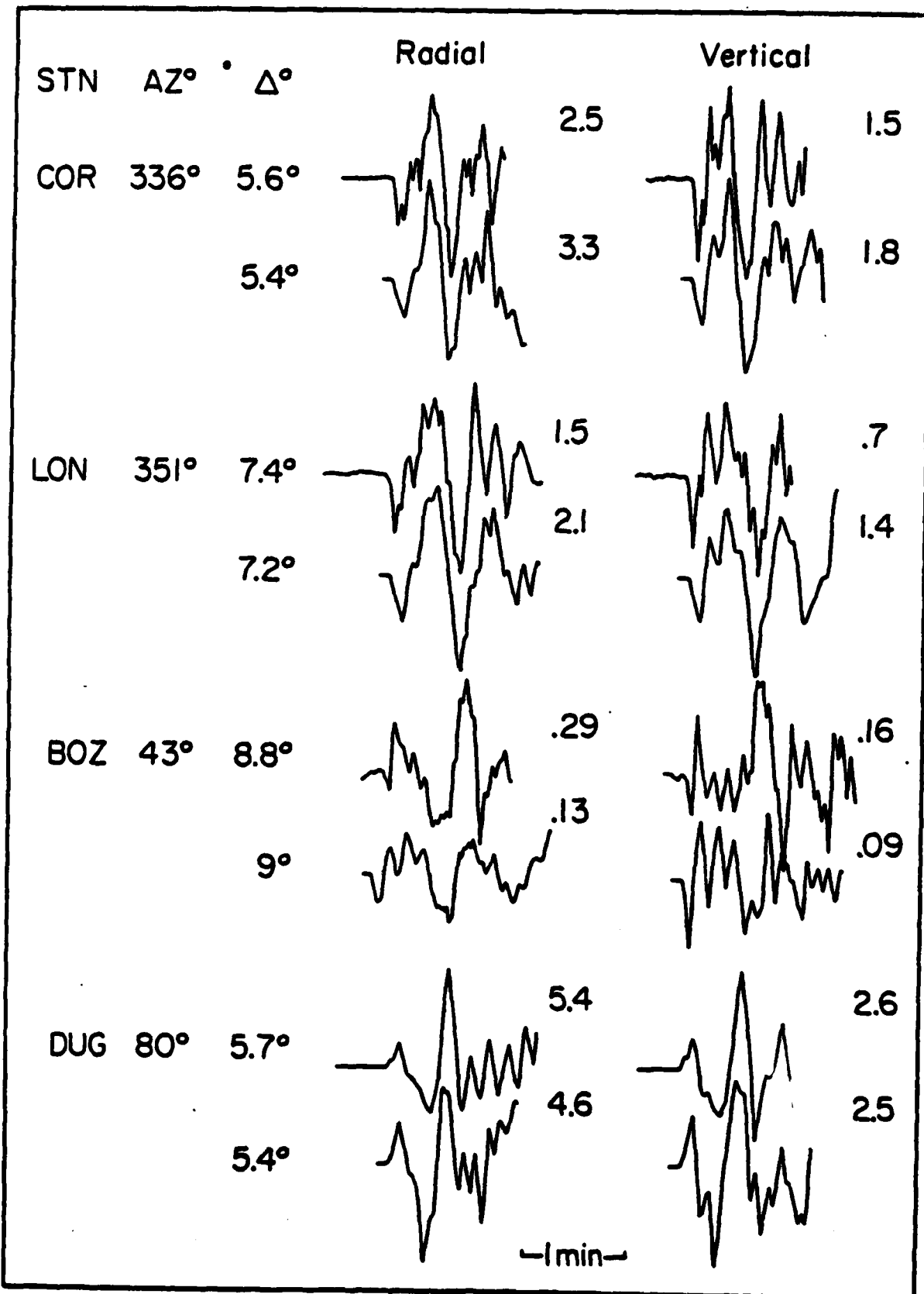


fig 11

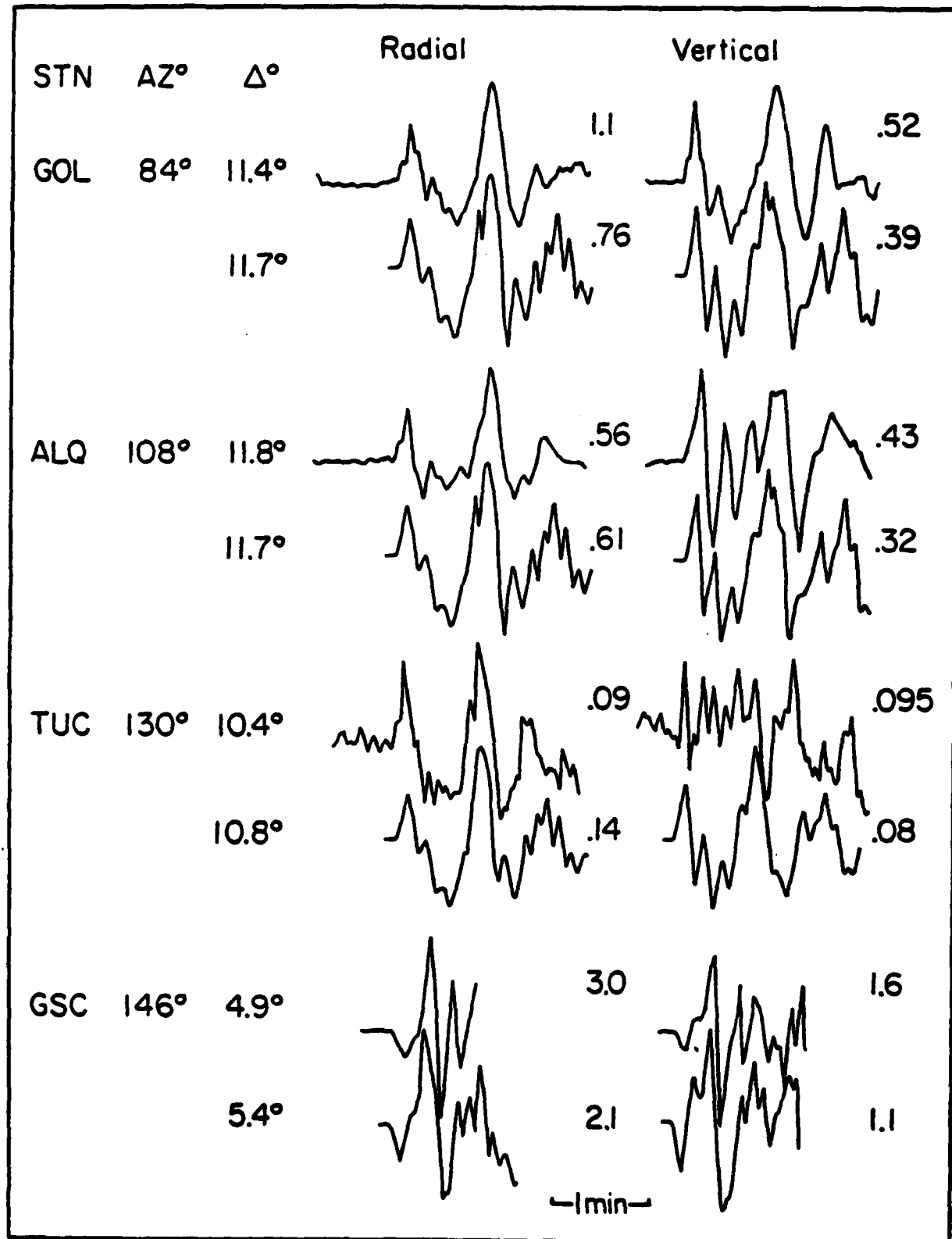


fig 12

Borrego Mountain, GOL

Radial

Vertical

2.1

OBS.

1.6

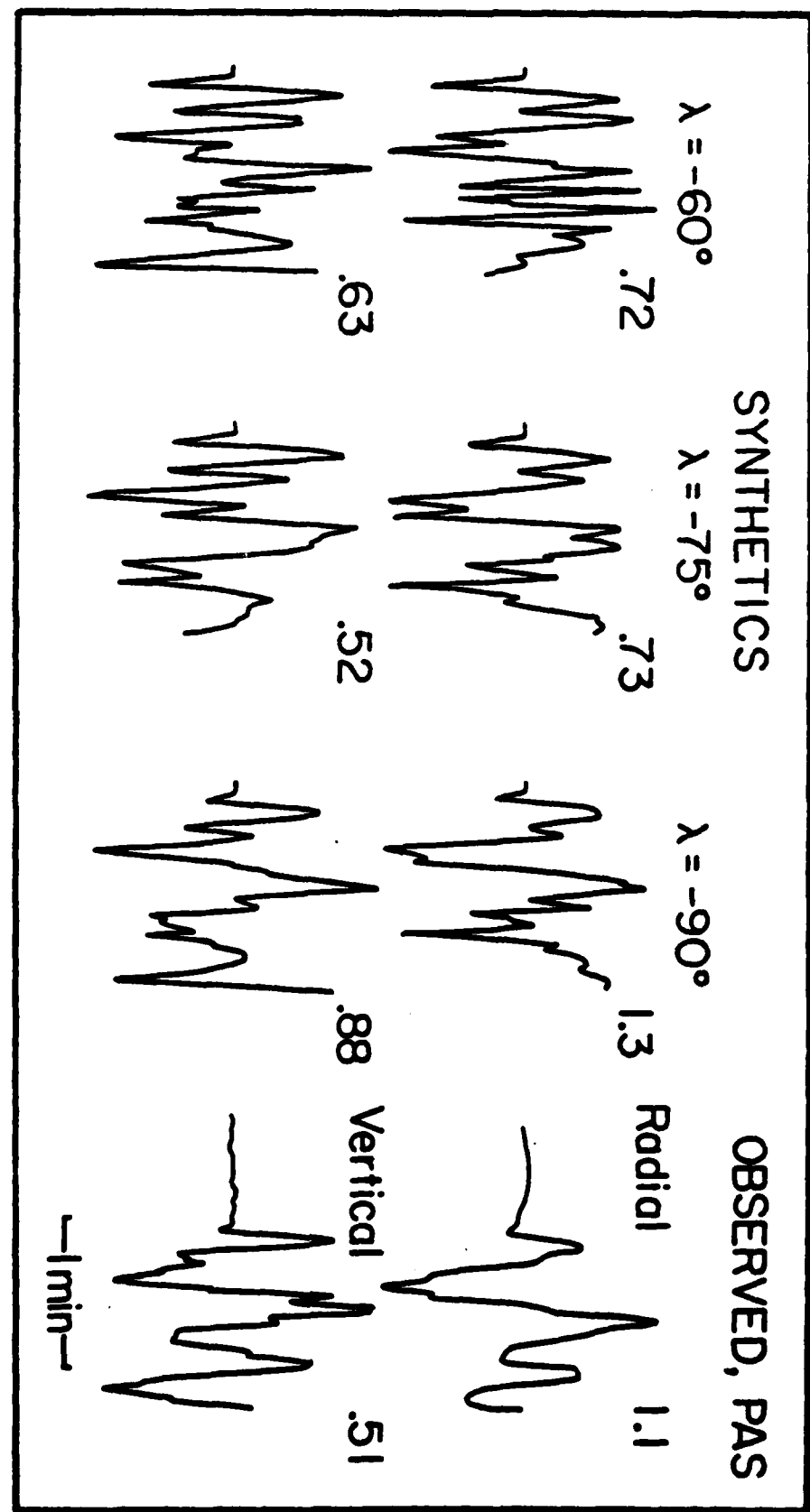
3.1

SYN.

1.6

—1 min—

fig 13



A TECHNIQUE FOR THE INVERSION OF REGIONAL DATA IN
SOURCE PARAMETER STUDIES

by

Terry C. Wallace

Don V. Helmberger

George R. Mellman

Seismological Laboratory
California Institute of Technology
Pasadena, California 91125

ABSTRACT

A technique is presented for the inversion of the beginning portion of vertical and radial seismograms containing P_n and PL (referred to as P_{nl}), to determine the source parameters of moderate size earthquakes. The P_{nl} section of a regional seismogram (ranges of 1 to 12 degrees) is used in a least squares waveform inversion. The technique involves an iterative scheme which makes use of an error function determined by the cross-correlation of a long-period P_{nl} and a synthetic. Both the data and the synthetics are normalized to make the solution insensitive to absolute amplitudes. The method utilizes the fact that for a given range, the synthetic waveform is constructed with the three fundamental faults. This means that the error functions can be written as a series of cross-correlations multiplied by constants corresponding to source orientation. Once the cross-correlations are computed, the source orientation is determined iteratively and only the constants have to be recalculated. This makes the procedure efficient. It is also possible to incorporate absolute amplitude information in the inversion depending upon the circumstances. The technique appears ideal for determining the source parameters of moderate size earthquakes. In addition, in the course

of inverting a number of events, anomalous travel paths will become apparent and can be investigated. The technique is applied to three western U.S. earthquakes.

Introduction

Determining the source parameters of shallow, moderate size earthquakes (in the magnitude range between 5 and 6) is an important problem for several reasons. Earthquakes of this type have wide spread geographic occurrence, and in some cases these earthquakes provide the only clue to the tectonics of a region. The wide spread occurrence makes these events desirable sources in crustal structure studies and are ideal for studying the upper mantle shear structure since they produce SH waves which are on scale at triplication distances. There has been considerable work done on modeling of the body wave phases from shallow earthquakes at teleseismic distances with synthetic seismograms. The procedures for these teleseismic modeling methods are outlined by Fukao (1971), Helmberger (1974), and Langston and Helmberger (1975). Unfortunately, for earthquakes to be sufficiently well recorded on the WWSSN network to apply these techniques (at distances beyond 30 degrees), they must have magnitudes which are larger than 6. At regional distances, 1° to 12° , the body waveforms become more complicated because of the waveguide properties of the crust. However, it appears that the long period information is sufficiently insensitive to the crustal details to allow extraction of source parameters, see Helmberger and Engen (1980).

In this paper we will present a technique for the inversion of regional phases to determine source parameters. The technique involves an iterative method which maximizes a normalized cross-correlation of

observed waveforms with synthetics to obtain the source parameters in a least squares operation. The method is similar to that originally proposed by Mellman, Burdick and Helmberger (1975). The usefulness of the technique is demonstrated by inverting the regional data from three western U. S. earthquakes. Two of these events, the Truckee, California ($M=5.7$), earthquake of 1966 and the 1975 Pocatello, Idaho ($M=6.1$), earthquake were used since they have published fault plane solutions and teleseismically determined moments. The third event, which is in the same region as the Pocatello earthquake occurred in 1962 and is small enough that it does not have well recorded teleseismic body waves.

P_{nl} Waveforms

At regional distances, out to about 12° , the P_{nl} waveform is that part of the seismogram which arrives before the surface waves. The first part of P_{nl} is dominated by P-waves; moving back into the record the waveform contains progressively more SV (PL) contributions corresponding to rays bouncing in the crust. Under ideal conditions P_{nl} is polarized in the vertical and radial planes, with the vertical component being the most important. In general, we can simply use geometry to determine the relative strengths of the horizontal seismograms from the radial motions, and conversely the radial motion can be found by the summation of the two horizontal components. Figure 1 shows a representative P_{nl} waveform.

Helmberger and Engen (1980) have successfully modeled the $P_{n\ell}$ section of long period seismograms with a point shear dislocation in a layer (corresponding to the crust) over a half-space (mantle) with the crustal model shown in Table 1. They used generalized ray expansions in conjunction with the Cagniard-deHoop technique to formulate the vertical and radial displacements in cylindrical coordinates as

$$w(r, z, \theta, t) = \frac{M_0}{4\pi\rho} \left(\dot{D}(t) * \sum_{i=1}^3 W_i(t) A_i \right) \quad (1)$$

$$q(r, z, \theta, t) = \frac{M_0}{4\pi\rho} \left(\dot{D}(t) * \sum_{i=1}^3 Q_i(t) A_i \right) \quad (2)$$

where

$\dot{D}(t)$ = far field time history

ρ_0 = source region density

M_0 = the seismic moment

The A 's are coefficients determined by source orientation and are given by

$$A_1(\theta, \lambda, \delta) = \sin 2\theta \cos \lambda \sin \delta + 1/2 \cos 2\theta \sin \lambda \sin \delta$$

$$A_2(\theta, \lambda, \delta) = \cos \theta \cos \lambda, \cos \delta - \sin \theta \sin \lambda, \cos 2\delta$$

$$A_3(\theta, \lambda, \delta) = 1/2 \sin \lambda \sin 2\delta$$

where

θ = strike from fault plane

λ = rake angle

δ = dip angle

The W_i and Q_i are the Green's functions appropriate for the vertical and radial step dislocations respectively. The W_i 's for the crustal model in Table 1 computed as a function of range are displayed in Figure 2. We will assume that regional observations can be modelled by rounding-off the epicentral distance to an even 100 km and choosing the proper $D(t)$ and A combination. The Table 1 model was shown to be adequate for modeling a number of western U.S. events but its suitability for other regions is not known, although the general P_{nl} waveform pattern observed in other regions appear quite similar. Figure 3 shows one such example comparison for a Buffin Island earthquake.

The numbers on the vertical traces in Figure 3 are maximum peak to peak amplitudes. Note agreement in observed amplitude and predicted P_{nl} . The prediction was based on the moment of 1.7×10^{25} dyne-cm determined teleseismically by Liu and Kanamori (1980). The main difference between the data and the synthetics is the high frequency content. Thus, it appears that the source parameters can be systematically determined by using the long-period P_{nl} waveform information.

Inversion Procedure

The least squares waveform inversion is similar to a technique proposed by Mallman et al. (1975). The technique makes use of an error

function as shown in equation 3,

$$e = 1 - \frac{\int fg}{(\int f^2)^{1/2} (\int g^2)^{1/2}} \quad (3)$$

where f is a long-period seismogram, g is a synthetic, and the integral is a zero log cross-correlation. The denominator serves to normalize both the data and the synthetics. The normalization makes the error function insensitive to the absolute amplitudes. We want to minimize the error which corresponds to maximizing the correlation, which is to say we allow f and g to optimally align themselves with regard to waveform. f and g are aligned apriori in time by matching first breaks and without regard to absolute travel time. Equation 3 can be rewritten considering that a synthetic seismogram can be constructed with the three fundamental faults:

$$e = 1 - \frac{\sum_1^3 A_i \int u_{di} f}{\left(\sum_i^3 \sum_k^3 A_i A_k \int u_{di} u_{dk} \right)} \quad (4)$$

Now f is a normalized seismogram. The u_{di} where $d = w$ or q corresponds to $W_i(t)$ and $Q_i(t)$ convolved with $D(t)$ respectively. The A_i 's are the coefficients shown in Equation 2. For a given range the cross-correlations are constant and the errors can be minimized by varying the A_i 's.

An objective function, which is the sum of the squares of the error functions, is minimized in terms of the three fault parameters. We can state the problem formally by taking a starting model vector \underline{m}^0 with an associated waveform error vector \underline{e}^0 , then we want to find a model change $\delta \underline{m}$ that minimizes the objective function:

$$\underline{\epsilon}^2 = \sum_j^N \underline{e}_j^2 \quad (5)$$

$$\underline{\epsilon}^2(\delta \underline{m}) = (\underline{e}_j^0 + \delta \underline{e}_j)(\underline{e}_j^0 + \delta \underline{e}_j)$$

Now consider $\delta \underline{e}_j$; from equation (4) we can write

$$\frac{\delta \underline{e}_j}{\delta \theta_k} \delta \theta_k = \delta \underline{e}_j \quad (6)$$

where θ_k is the three fault parameters strike, rake and dip. We can write the partials of the error functions with respect to the fault parameters as an $N \times 3$ matrix A where N is the number of error functions, and we can write $\delta \theta_k$ as a vector.

$$\underline{A} \delta \theta = \underline{A} \phi = \delta \underline{e}_j \quad (7)$$

so we can rewrite (5) as

$$\underline{\epsilon}^2 = (\underline{e} + \underline{A} \phi)^T (\underline{e} + \underline{A} \phi) \quad (8)$$

which can be expanded

$$\underline{\epsilon}^2(\delta \underline{m}) = \underline{e}^T \underline{e} - \underline{e}^T \underline{A} \phi - \phi^T \underline{A}^T \underline{e} + \phi^T \underline{A}^T \underline{A} \phi \quad (9)$$

Now performing a first order perturbation in $\delta \phi$ of equation (9) and setting to zero yields

$$\phi = (\underline{A}^T \underline{A})^{-1} \underline{A}^T \underline{e} \quad (10)$$

which is the result we require. This is the classical linear least squares solution, see Wiggins (1972). This gives us an inversion which is non-linear, but a simple iterative technique is used to converge on the correct fault parameters. On each step the error functions and their partials must be recalculated; but the cross-correlations only have to be calculated once. This makes recalculating the error functions and partials fast, and the procedure is efficient. In practice we usually weight the data station by station, and add some factor stabilizing the inverse, so we write (10) as

$$\phi = (A^T W^2 A + \sigma I)^+ A^T W e \quad (11)$$

It is also possible to incorporate absolute amplitude information in the inversion depending upon the circumstances. This is done by calculating a second error function for amplitude, and the partial is computed for the dependence of amplitude rather than waveform on source orientation. The Green's functions described in the previous section are used for the synthetics. The far field time history, $D(t)$, is fit independently. It has been found that for most moderate size earthquakes a trapezoid with a 1 second rise, 1 second top and 1 second fall time is adequate. An attenuation operator is not used on the synthetics; the principal difference between the data and synthetics is high frequency content, so both the data and the synthetics are low passed filtered. Usually, a filter whose impulse response is a triangle with a 2 or 3 second rise and fall time is sufficient.

Figure 4 shows a test of the program. The data were generated at various ranges and azimuths for a source with a strike of 10° , a rake of 80° and a dip of 50° . Stations 1, 4 and 5 are long-period WWSSN (15-100) records, while stations 2 and 3 are long-period LRSM records. Since the data was dip-slip the starting model was backed off to a strike slip orientation. The cross-

correlation coefficients between the data and the model are shown on the front of each trace. At the top of each column is the sum of the error functions. How rapidly this sum decreases is a measure of the rate of convergence. After three iterations the strike has essentially been picked, and after six iterations the waveforms are in fair agreement. After nine iterations there is no difference between the data and the model.

The moment of an earthquake can be determined by comparing the amplitude of the synthetics and the data. Adopting the units of Helmberger and Malone (1975), and expressing r in km, time in seconds, density in gm/cm^3 , velocity in km/sec , the moment in dyne-cm and displacements in cm, yields

$$M_0 = 4\pi p_0 \times 10^{20} \left(\frac{\text{data amplitude}}{\text{synthetic amplitude}} \right) \quad (12)$$

The ratio of the moment at each station to the mean is a measure of the amplitude stability. In general the moments determined from P_{nl} waveforms are in very good agreement with those determined teleseismically.

Using Helmberger and Engen's (1980) models, Green's functions were generated every hundred km for a source which was 8 km deep. In computing the cross-correlations, the set of Green's functions which are closest to the range are used (which may result in an error of up to 50 km). Using Green's functions at this spacing is usually adequate since increasing range usually just increases the separation between P_n and direct P. Obviously, imperfections in the Green's functions will be observed due to non-ideal structure, varying crustal thickness, directivity, etc., but usually these are small; travel paths which routinely cause waveforms which deviate from the ideal case will be used to map the moho and upper mantle structure. The fact that the Green's functions are only generated for one depth at this time somewhat limits the applicability to earthquakes with depths between 6 and 10 km. Synthetics appropriate for other depths can be obtained by

splitting the Green's function into those rays which start upward and those that start downward and applying a shift operator, see Helmberger and Engen (1980). It becomes relatively easy to invert to source depth as well as crustal thickness by working with split Green's functions. These embellishments as well as others will be added as the data sets are developed.

Application to Regional Data

To test the program we inverted the P_{nl} waveforms of three western U.S. earthquakes. Two of these earthquakes, the Truckee and Pocatello earthquakes, are well-studied, and should provide comparisons for the inversion solutions. The third event occurred in the same region as the Pocatello earthquake, and is therefore likely to have a similar mechanism, although this event is small enough not to be well-recorded teleseismically.

Truckee (9/12/66)

The Truckee earthquake ($m_b = 5.7$) provides a good test since it has been studied by numerous authors (Ryall, Van Wormer and Jones, 1968; Tsai and Aki, 1970; Burdick, 1979). Tsai and Aki (1970), from first motion studies and modeling of surface waves, determined this event to be pure strike-slip on a fault plane striking N 44° E and dipping 80° SE. From surface wave data they determined the moment to be $.83 \times 10^{25}$ dyne-cm, and the depth to be 10 km. Since this is a strike-slip event, and much less energy is radiated down than for a dip-slip event, only a few high quality teleseismic records are available. From these, Burdick (1977) determined a body wave moment of $.6 \times 10^{25}$ dyne-cm, and a triangular time function with a 1 second rise and a 2 second fall. Figure 5 shows the location and data for Truckee, and Figure 6, shows the filtered data and synthetics for the inversion results. The event was also recorded at BOZ and TUC (LPZ). These records are very nearly nodal, and it was judged that

the waveform amplitudes were not sufficiently above the noise to be useful in the inversion.

The inversion result for Truckee was very similar to the solution of Tsai and Aki (1970); a strike of N 43° E, dip of 76° SE and a rake of -11°. The only significant difference is the slight dip-slip component, which is also acceptable on the basis of the first motion data. The moment determined from the inversion is $.87 \times 10^{25}$ dyne-cm, which is in excellent agreement with Tsai and Aki's (1970) moment. Shown with each trace in Figure 6 is the ratio of the station moment to the average moment. Note the low amplitude at LON in comparison with the other stations as well as the large P_n to PL ratio at TUC. Both of these features occur for the other events suggesting anomalous structure.

Pocatello (3/28/75)

The Pocatello ($m_b = 6.1$) earthquake was a dip-slip event in eastern Idaho, and again is well-studied (Bache, Lambert and Barker, 1980; Arabast, Richins and Langers, 1975). This earthquake occurred in a region which is frequented by moderate sized events. Bache *et al.* (1980) determined the fault plane to be striking N 45° E, dipping 39° to the west and with a rake of -53° (the fault plane is shown in Figure 7), and they determined a focal depth of 8.7 km. Using long-period teleseismic data only, they obtained a moment of 2.2×10^{25} dyne-cm, and with their preferred model using both short- and long-period data obtained a moment of 1.5×10^{25} dyne-cm. Williams (1979) obtained a moment of 1.2×10^{25} dyne-cm from surface waves.

The inversion solution for Pocatello appears superficially different from that of Bache *et al.* (1980), but Figure 7 shows both their fault plane solution and ours; in fact the solutions are very similar. We found a strike

of N 20° E, a dip of 38° to the west and a rake of -110°. The moment determined from the inversion is 1.6×10^{25} dyne-cm which is in good agreement with the various authors' determinations. Figure 8 shows the data and the synthetics, and again the ratio of moments is shown as a measure of amplitude stability. Figure 9 shows why Bache et al. (1980) solution was altered in the inversion. Although most stations were fit well by either model, PAS and TUC were fit poorly by the Bache et al. (1980) solution as compared to the inversion solution. The predicted amplitudes are good for all stations with the exception of LON, which is again off by a factor of 2.

Idaho-Utah (8/30/62)

The Idaho-Utah event occurred within 60 km of the Pocatello earthquake in the Cache Valley, and was well recorded on the LRSM network. The magnitude was 5.7 and a fault plane solution has been determined by Smith and Sbar (1974). We would expect the regional stress pattern to be similar in this region to that in the Pocatello Valley. The data and location of the event and stations is shown in Figure 10. Although the depth of the earthquake is not precisely known, it is assumed that it is shallow from the similarity of the waveforms to that of the Pocatello earthquakes. The inversion yields a solution with a fault plane striking N 33° E, dipping 34° to the east and with a rake of -64°, which is similar to Smith and Sbar (1974). The moment determination is $.71 \times 10^{25}$. Figure 11 shows the filtered data and synthetics, with the ratio of the moments.

Discussion

This least squares waveform inversion makes it possible to use the regional phases to determine the source parameters of moderate size earthquakes. One of the advantages of this technique is that it is based on a cross-correlation between a normalized long-period seismogram and Green's function for the three fundamental faults and therefore is insensitive to absolute amplitude information. In comparison, most other inversion methods, such as moment tensor inversion (see Stump and Johnson, 1977; and Langston, 1980) use absolute amplitude information. Although the inversion is iterative, the cross-correlations only have to be calculated once which makes the system fast. For the three test earthquakes used the inversion usually converged on a solution within 15 iterations. This technique is practically ideal for shallow moderate size earthquakes in continental regions where a small number of long-period stations will be available at regional distances.

One result from the three earthquakes investigated was the stability of the amplitudes. In general, the stability is better than that of teleseismic waveforms where factors of 2 between predicted and observed amplitudes are common. This is remarkable considering the plane layer over a half-space approximation for the crust mantle system. Helmberger and Engen (1980) found that for their models the long-period behavior of $P_{n\ell}$ is independent of the short periods at the longer ranges, and that the long-period synthetics are dominated by the interference of head waves. Since we expect the moho to be approximately planar, $P_{n\ell}$ should act like the model except for variations in crustal thickness; the head waves should be pretty insensitive to these variations.

The most obvious problem in modeling the moho is that it is probably dipping. But still $P_{n\ell}$ should be stable since we expect multiple reflections

corresponding to the SV-legs to occur either near the source or near the receiver depending on the slope of the moho. Hong and Helmberger (1978) address this problem and show that shooting up-dip (crust thinning towards receiver) bunches the reflections near the receiver and down-dip near the source. So our Green's functions should be sufficient to use in the inversion of most P_{nl} waveforms. The high Q of the crust makes it possible to ignore attenuation. The main difference between the synthetics and the observations is high frequency content. Convolving a simple triangle with both the observations and synthetics is sufficient to give good waveform matches and take the place of any Q operator.

When we have inverted the P_{nl} waveforms from a large number of earthquakes certain travel paths will consistently appear anomalous. An example of this might be very large crustal variations, say associated with a deep root of the Sierra Nevada mountains or crustal transitions along the continental oceanic boundaries. These paths can be identified by discrepancies within the P_{nl} waveform and then investigated more fully. We ignore absolute travel time, but obviously variations in crustal thickness and crustal and mantle velocities will affect travel times. By fitting the waveform and then comparing the theoretical to observed travel times, we can identify these anomalies.

Although in this paper we have presented the inversion technique for regional data, in fact the program can be used for any waveform in which an appropriate set of Green's functions can be generated. For example, we should be able to use earthquakes which are recorded at upper mantle distances and use upper mantle models such as Burdick's (1977) T7, or Given and Helmberger's (1980) K8 to generate Green's functions. This should make it possible to determine the source parameters of any moderate size earthquake. Also imperfections in the Green's functions should become evident, and anomalous regions can be

studied in detail.

In conclusion, we have developed a least-squares inversion which can be used to model moderate size earthquakes recorded at regional distances. This is possible since P_{nl} is stable and can be modeled with simple structure. The program makes use of a cross-correlation between the long-period data and the Green's functions corresponding to the three fundamental faults. Once these correlations are calculated, a simple iterative procedure is used to determine the fault parameters. The use of P_{nl} opens up several doors of research: crustal and upper mantle structure, tectonics of inaccessible but moderately seismic regions, and source parameter studies.

Acknowledgment

This research was supported by the Advanced Research Projects Agency of the Department of Defense and was monitored by the Air Force Office of Scientific Research under Contract No. F49620-77-C-0022.

Contribution No. 3454, Division of Geological and Planetary Sciences, California Institute of Technology, Pasadena, California 91125.

References:

- Arabasz, W. J., W. D. Richins and C. J. Langer (1975). Detailed characteristics of the March 1975 Idaho-Utah border earthquake sequence, EOS, 56, 1022.
- Bache, T. C., D. G. Lambert and T. G. Barker (1980). A source model for the March 28, 1975 Pocatello Valley earthquake from time-domain modeling of teleseismic P waves, Bull. Seism. Soc. Am., 70, 405-418.
- Burdick, L. J. (1977). Broad-band seismic studies of body waves, PhD Thesis, California Institute of Technology.
- Fukao, Y. (1971). Seismic body waves from surface faults, J. Phys. Earth, 19, 271-281.
- Given, J. W. and D. V. Helmberger (1980). Upper mantle structure of northwestern Eurasia, Jour. Geophys. Res., in press.
- Helmberger, D. V. (1974). Generalized ray theory for shear dislocations, Bull. Seism. Soc. Am., 64, 45-64.
- Helmberger, D. V. and G. R. Engen (1980). Modeling the long-period body-waves from shallow earthquakes at region ranges, Bull. Seism. Soc. Am., in press.
- Helmberger, D. V. and S. D. Malone (1975). Modeling local earthquakes as shear dislocations in a layered half-space, Jour. Geophys. Res., 80, 4881-4888.
- Hong, T. L. and D. V. Helmberger (1977). Generalized ray theory for dipping structure, Bull. Seism. Soc. Am., 67, 995-1008.
- Langston, C. A. and D. V. Helmberger (1975). A procedure for modeling shallow dislocations, Geophys. Jour. R. astr. Soc., 42, 117-130.
- Langston, C. A. (1980). Source inversion of seismic wave forms; the Kogna, India, earthquakes of September 13, 1967, in preparation.
- Liu and H. Kanamori (1980). Determination of source parameters of midplate earthquakes from the wave forms of body waves, Bull. Seism. Soc. Am., in press.

- Mellman, G., L. Burdick and D. Helmberger (1975). Determination of source parameters from body wave seismograms, Earthquake Notes, 40, p. 44.
- Ryall, A., J. D. Van Warmer and A. J. Jones (1968). Triggering of micro-earthquakes by earthtides, and other features of the Truckee, California, earthquake sequences of September, 1966, Bull. Seism. Soc. Am., 215-248.
- Smith, R. B. and M. L. Sbar (1974). Contemporary tectonics and seismicity of the western United States with emphasis on the Intermountain Seismic Belt, Geol. Soc. Am. Bull., 85, 1205-1218.
- Stump, B. and L. Johnson (1977). The determination of source properties by linear inversion of seismograms, Bull. Seism. Soc. Am., 60, 1199-1208.
- Tsai, Y. B. and K. Aki (1970). Source mechanism of the Truckee, California earthquake of September 12, 1966, Bull. Seism. Soc. Am., 60, 1199-1208.
- Wiggins, R. (1972). The general linear inverse problem: Implications of surface waves and free oscillations for earth structure, Reviews Geophys. Space Physics, 10, 251-285.

TABLE 1 - CRUSTAL MODEL

P _{vel} (km/s)	S _{vel} (km/s)	Density (gm/cc)	Layer Thickness (km)
6.2	3.5	2.7	32
8.2	4.5	3.4	

FIGURE CAPTIONS

- Figure 1 A typical P_{NL} wave form recorded on a horizontal instrument. The beginning of P_{NL} is dominated by P_n ; moving back in the record PL dominates. The record is a long-period WWSSN recording of the Truckee earthquake at Golden Colorado.
- Figure 2 Profiles of the vertical displacements for the three fundamental faults. The numbers above each trace indicate the zero to peak amplitude in cm assuming $M_0 = 4\pi\rho_0 \times 10^{20}$ dyne-cm and trapezoidal time history (.5, .5, .5 sec). This time history was convolved with the delta function response to reduce the high-frequency spike created by the post-critical reflections so that the longer periods become more apparent.
- Figure 3 A comparison of the observed wave forms from the Buffin Island earthquake (4 Sept. 1963) with the synthetic predictions. The numbers on the vertical traces indicate the maximum peak-to-peak amplitude ($\times 10^{-3}$ cm). The mechanism is that of a normal fault, with a strike of 98° , dip of 66° and slip angle of -94° . The depth of the event is 7 km and $M_0 = 1.7 \times 10^{25}$ as modeled by Liu and Kanamori (1980).
- Figure 4 A test of the inversion program. The data was generated for a dip-slip earthquake and starting model has a strike-slip orientation. The cross-correlation coefficients between data and model are shown before each trace. At the top of each column is the sum of the error functions.

- Figure 5 The location of the Truckee earthquake and the data used in the inversion. The dashed lines show the P nodal planes of this pure strike-slip event.
- Figure 6 The filtered data and synthetics from the inversion solution for the Truckee earthquake. Along each trace the ratio of the station moment to the average moment is shown as a measure of amplitude stability. Also shown is the cross-correlation coefficient for the data and synthetic.
- Figure 7 Fault plane solutions of the Pocatello earthquake. The solid line gives Bache et al. (1980) solution, while the dashed lines give our solution.
- Figure 8 The filtered data and synthetics from the Pocatello earthquake. The data and synthetics are filtered with a 3 second triangle. Along each trace is the ratio of the station and average moment, as well as the cross-correlation coefficient.
- Figure 9 The filtered data and synthetics using Bache et al. (1980) fault plane solution. Note the first motion is incorrect at TVC and the relative amplitudes at PAS are bad.
- Figure 10 Location of the Idaho event and the stations recording it. The stations with two letter abbreviations are long-period LRSM instruments, and the others are WWSSN instruments. All records shown are vertical components.

Figure 11

The filtered data and synthetics for the 1962 Idaho earthquake. The moment was determined from the WWSSN stations, and the moment ratios are shown for these stations. The cross-correlation coefficients are shown.

GOL (TRUCKEE, M = 5.7),
 $\Delta = 11.4^\circ$

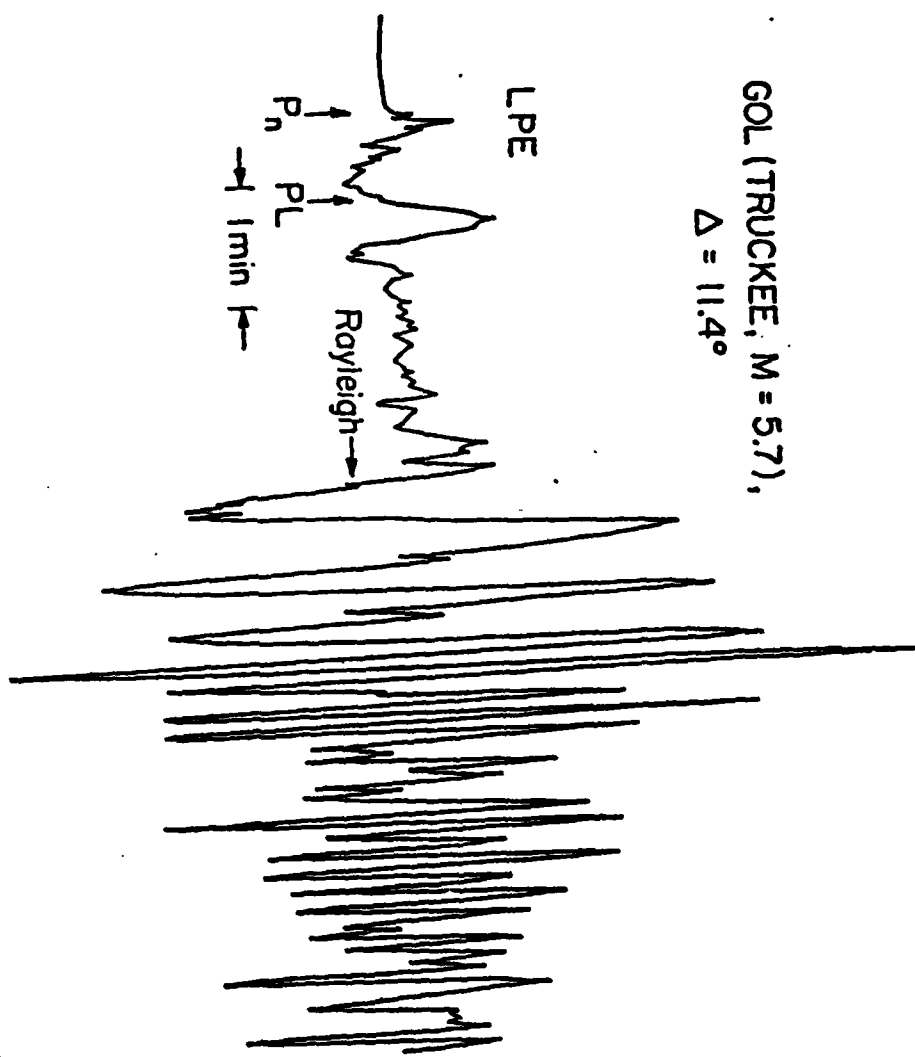


Figure 1 A typical P_n wave form recorded on a horizontal instrument.

The beginning of P_n is dominated by P_n ; moving back in the record PL dominates. The record is a long-period WSSN recording of the Truckee earthquake at Golden, Colorado.

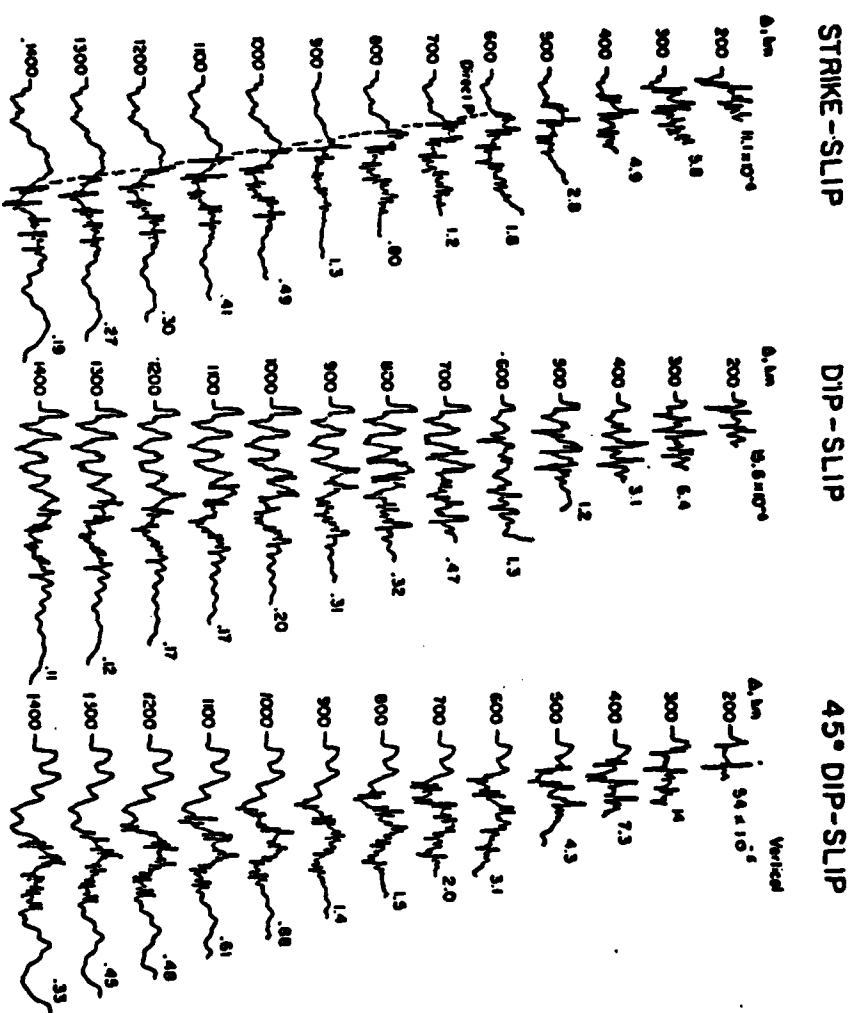
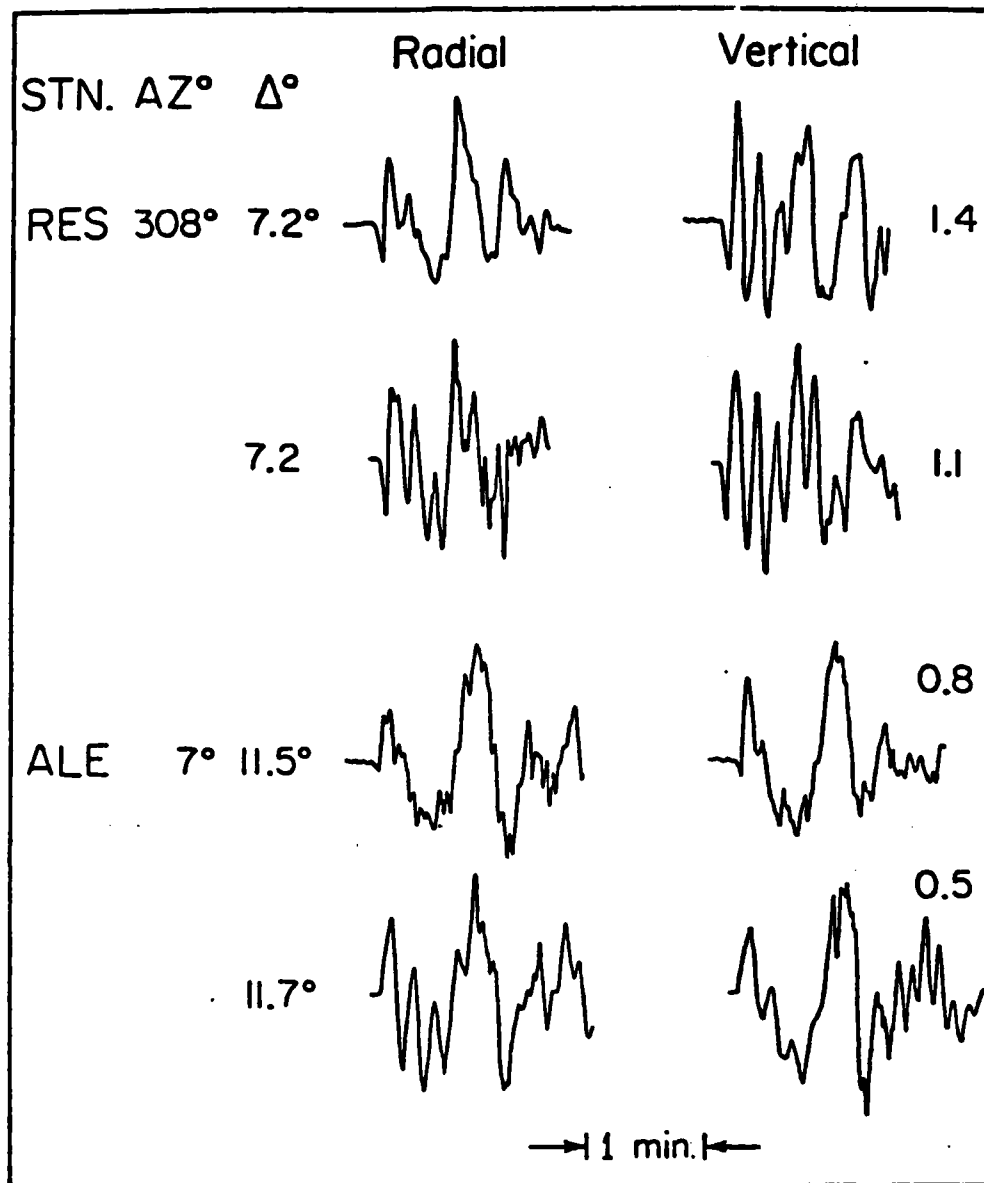


Figure 2 Profiles of the vertical displacements for the three fundamental

faults. The numbers above each trace indicate the zero to peak amplitude in cm assuming $M_0 = 4\pi p_0 \times 10^{20}$ dyne-cm and trapezoidal time history (.5, .5, .5 sec). This time history was convolved with the delta function response to reduce the high-frequency spike created by the post-critical reflections so that the longer periods become more apparent.

**Figure 3**

A comparison of the observed wave forms from the Buffin Island earthquake (4 Sept. 1963) with the synthetic predictions. The numbers on the vertical traces indicate the maximum peak-to-peak amplitude ($\times 10^{-3}$ cm). The mechanism is that of a normal fault, with a strike of 98°, dip of 66° and slip angle of -94°. The depth of the event is 7 km and $M_o = 1.7 \times 10^{25}$ as modeled by Liu and Kanamori (1980).

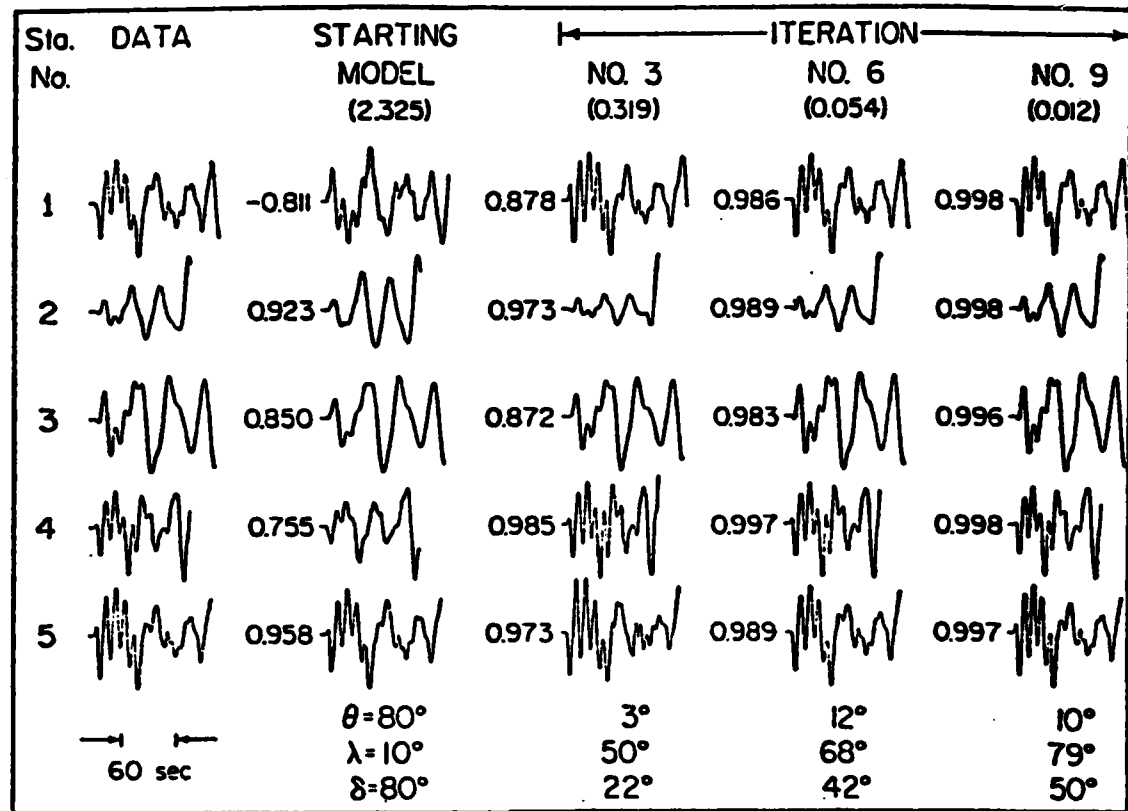
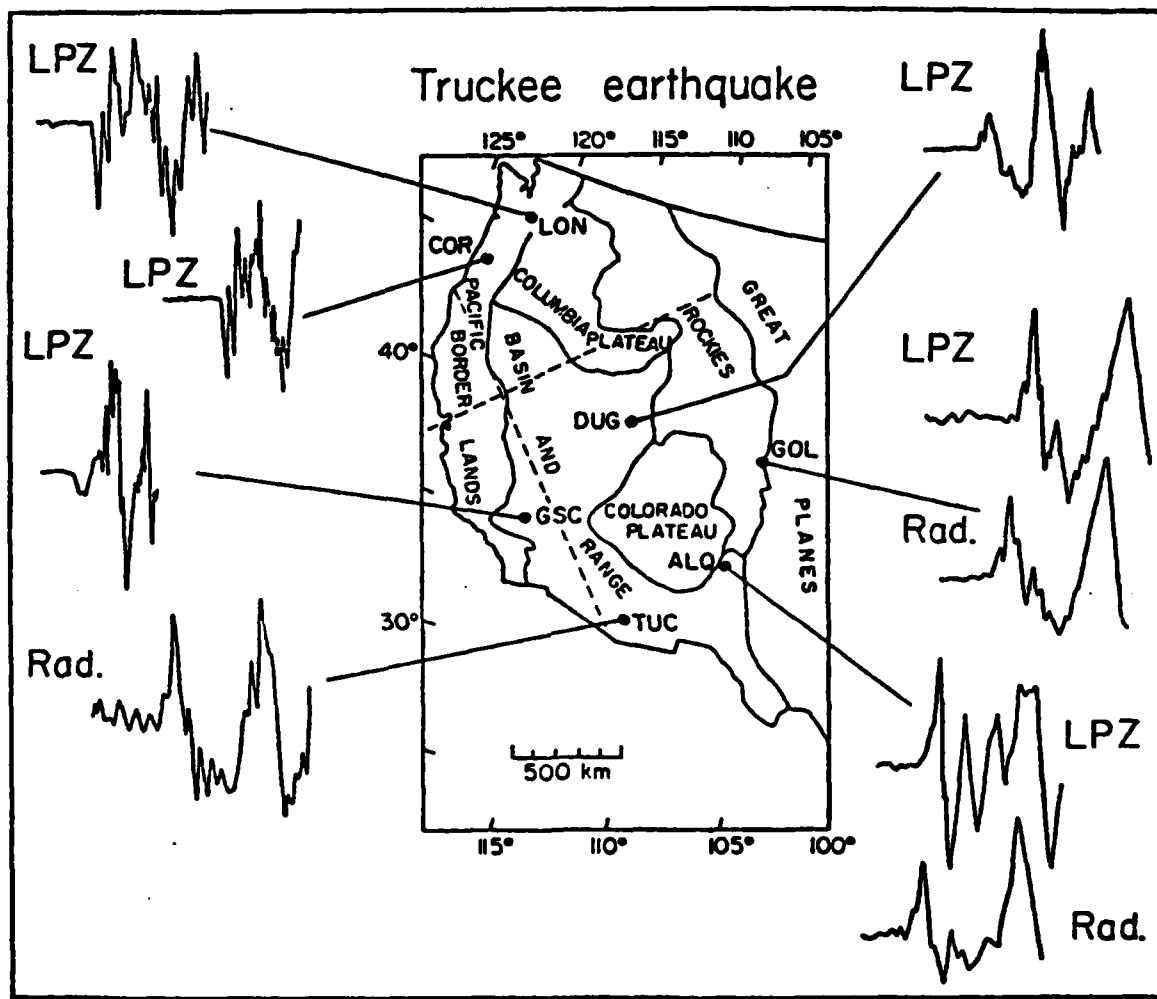
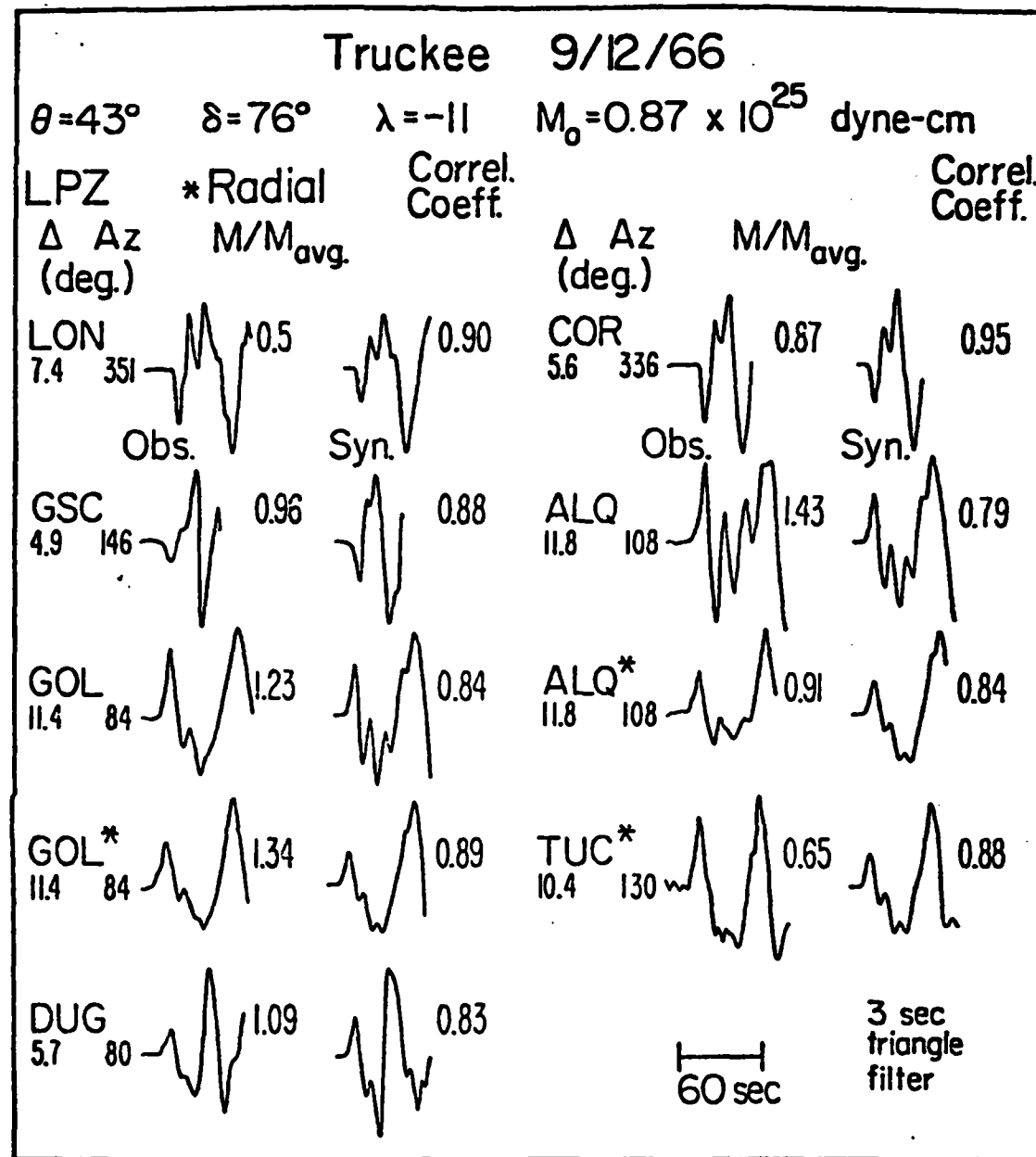


Figure 4 A test of the inversion program. The data was generated for a dip-slip earthquake and starting model has a strike-slip orientation. The cross-correlation coefficients between data and model are shown before each trace. At the top of each column is the sum of the error functions.

**Figure 5**

The location of the Truckee earthquake and the data used in the inversion. The dashed lines show the P nodal planes of this pure strike-slip event.

Figure 6

The filtered data and synthetics from the inversion solution for the Truckee earthquake. Along each trace the ratio of the station moment to the average moment is shown as a measure of amplitude stability. Also shown is the cross-correlation coefficient for the data and synthetic.

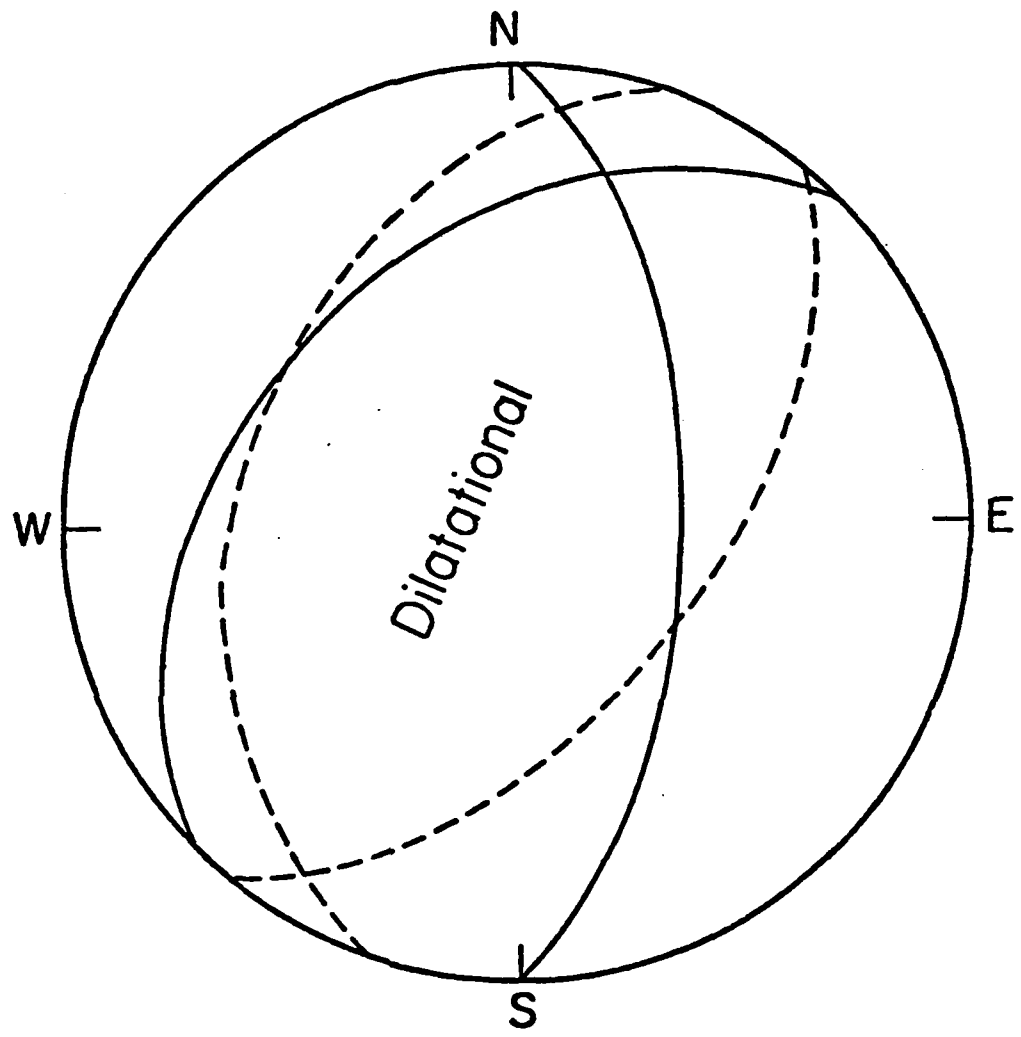
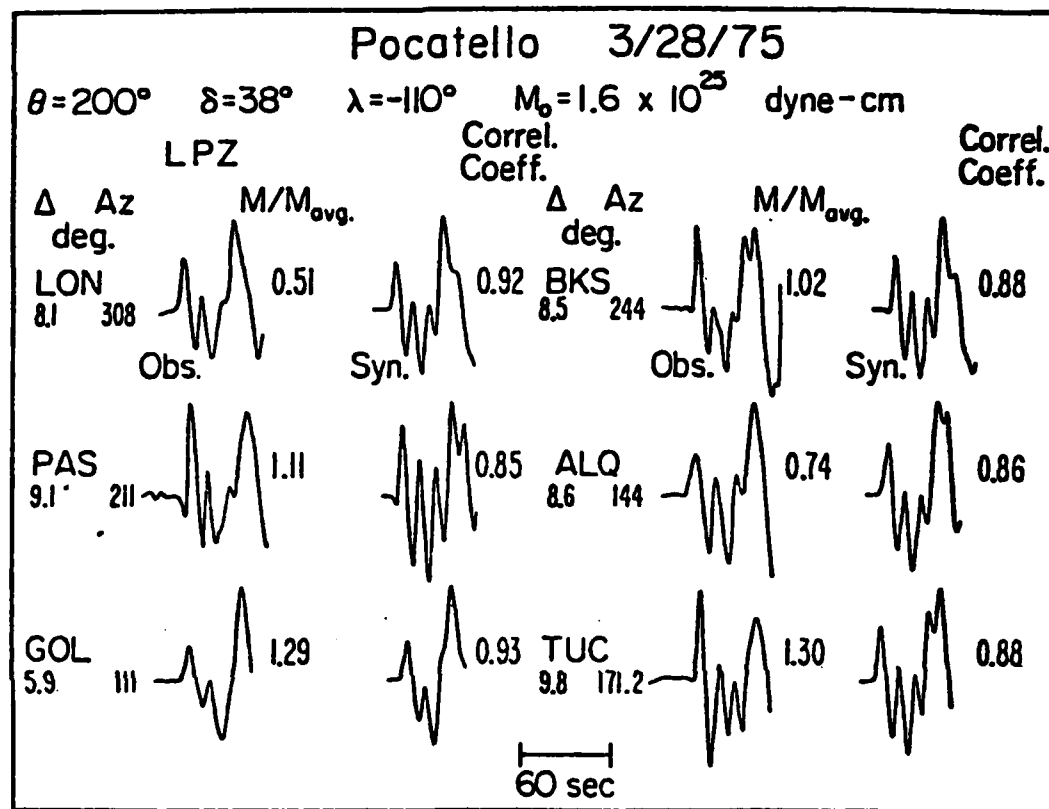
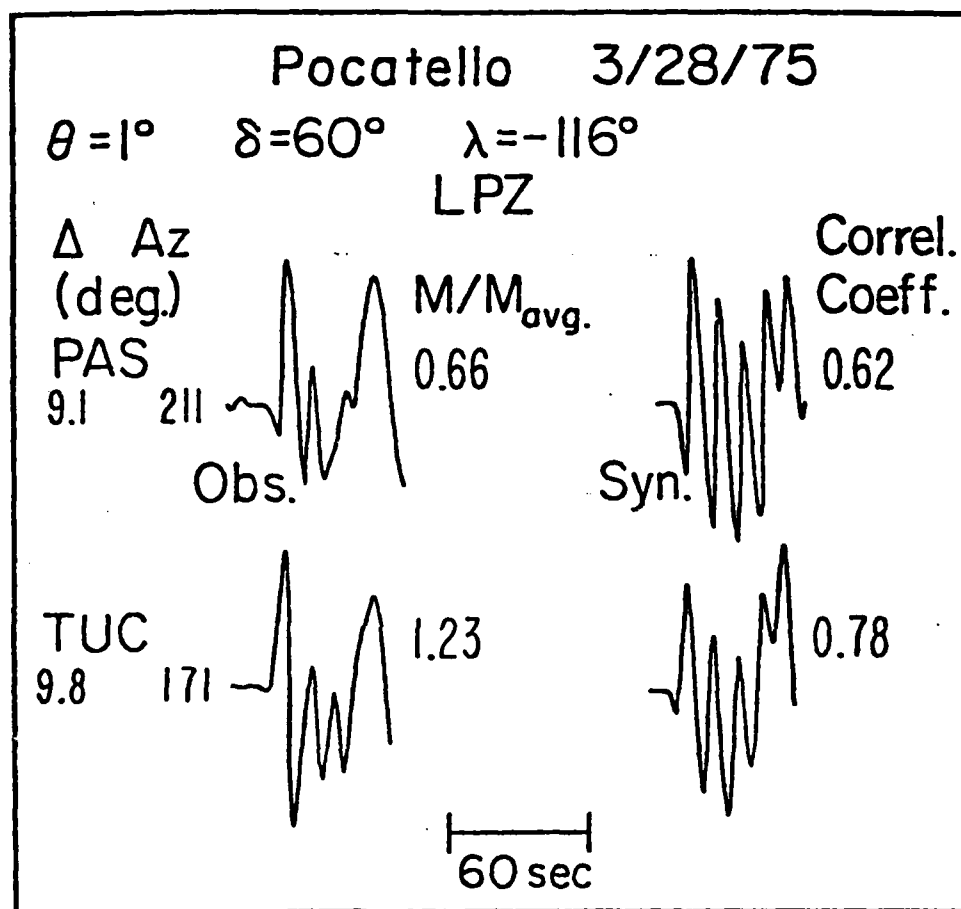


Figure 7 Fault plane solutions of the Pocatello earthquake. The solid line gives Bache et al. (1980) solution, while the dashed lines give our solution.

Figure 8

The filtered data and synthetics from the Pocatello earthquake. The data and synthetics are filtered with a 3 second triangle. Along each trace is the ratio of the station and average moment, as well as the cross-correlation coefficient.

**Figure 9**

The filtered data and synthetics using Bache *et al.* (1980) fault plane solution. Note the first motion is incorrect at TVC and the relative amplitudes at PAS are bad.

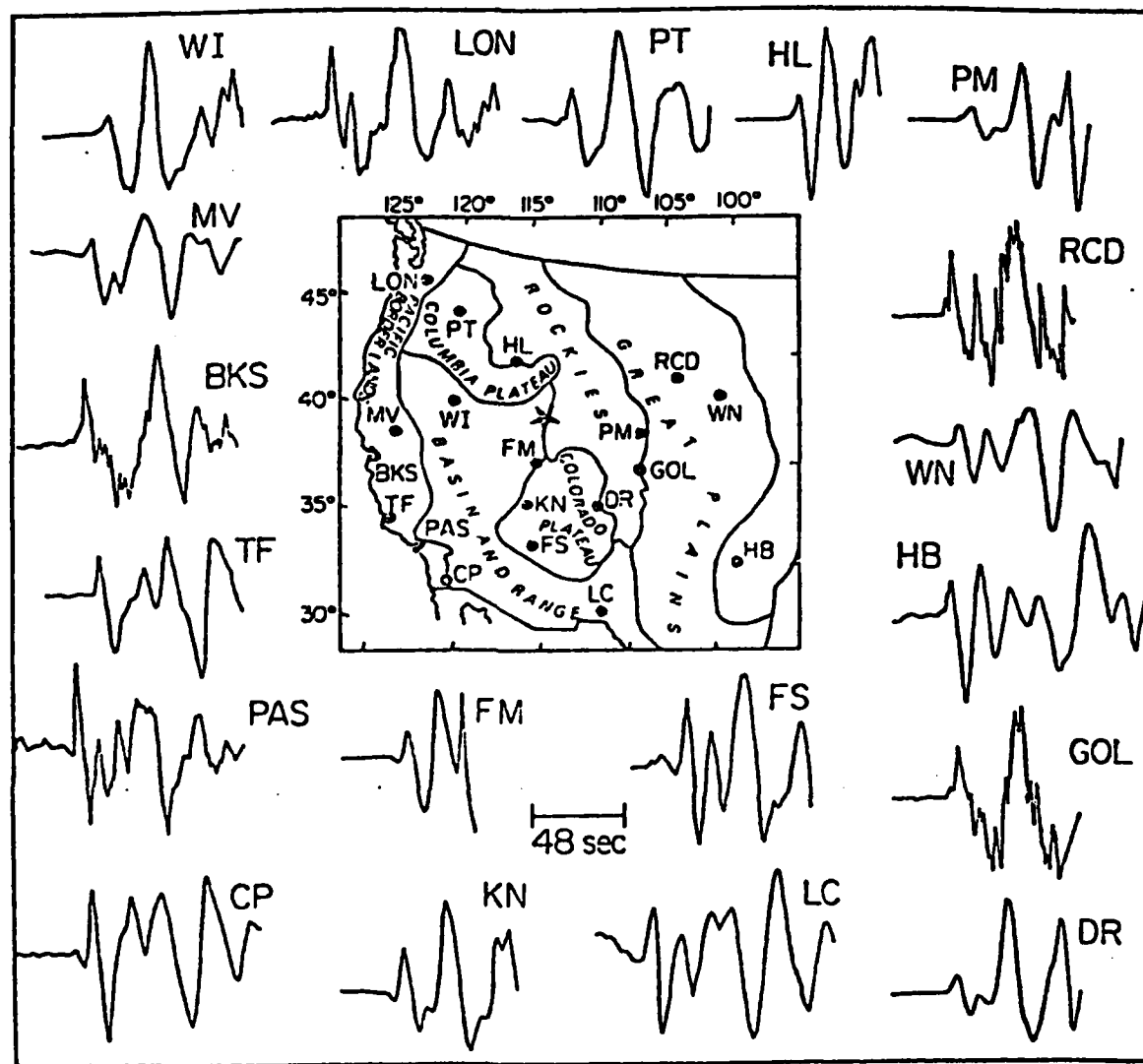
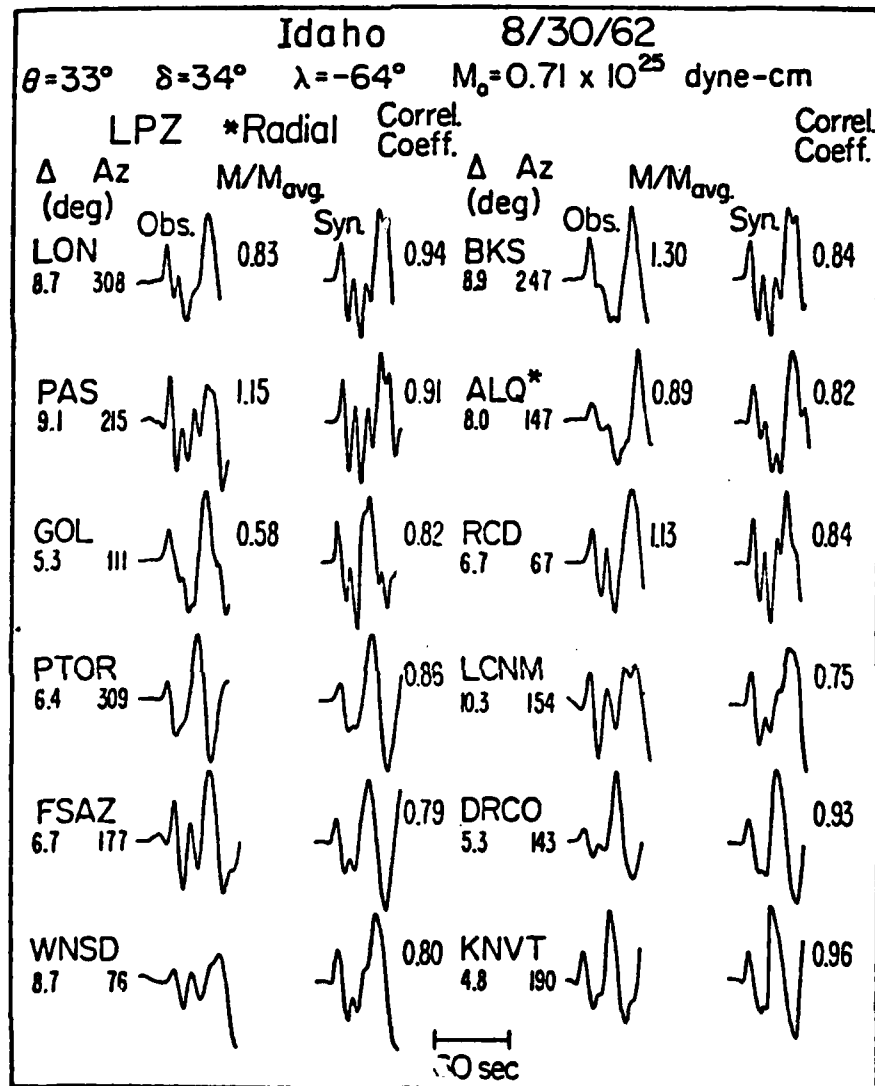


Figure 10 Location of the Idaho event and the stations recording it. The stations with two letter abbreviations are long-period LRSM instruments, and the others are WWSSN instruments. All records shown are vertical components.

Figure 11

The filtered data and synthetics for the 1962 Idaho earthquake.

The moment was determined from the WWSSN stations, and the moment ratios are shown for these stations. The cross-correlation coefficients are shown.

Teleseismic Observations of the
1976 Friuli, Italy Earthquake Sequence
John Cipar

ABSTRACT

Teleseismic long-period body and surface waves radiated by the May 6, 1976 Friuli, Italy earthquake and its principal aftershock of September 15, 1976 (09h 21m) are studied to determine source characteristics. Focal mechanisms along with geological evidence suggest that both events represent the underthrusting of the Friuli plain beneath the Southern Alps. The depths of both earthquakes, estimated by matching synthetic body wave seismograms to observations, are found to lie between 6 and 10 km. It is not possible to discern any evidence of source directivity in the observed main shock body waves. Synthetic seismogram calculations which include rupture effects suggest that the fault length of the main shock could not be much larger than 16 km for a unilaterally propagating fault or about 24 km for a symmetrical rupture assuming a rupture velocity of 3.0 km/sec. Observations of 100 sec Rayleigh waves confirm the focal mechanism deduced from body waves, but suggest that the seismic moment of the main shock is 5×10^{25} dyne-cm compared to 2.9×10^{25} dyne-cm estimated from body waves. The P-wave moment of the aftershock is 1×10^{25} dyne-cm. The aftershock studied in this paper is one of four large events which occurred in the epicentral area of the main shock more than four months after the main shock. These aftershocks had a combined seismic moment over twice that of the main shock. It is suggested that these earthquakes represent deformation in a different part of the seismic zone than the main shock. Large earthquakes with series of severe aftershocks are well known in the historical record of the Friuli region. The average displacement and stress drop are estimated to be 33 cm and 12 bars for the main shock and 33 cm and 24 bars for the aftershock.

INTRODUCTION

One of the most damaging earthquakes in the European area in recent years struck the Friuli region of northeastern Italy on May 6, 1976. The main shock caused heavy loss of life and a great amount of property damage and was followed by an aftershock sequence of unusual severity.

The seismograms written by the Friuli earthquake and its aftershocks present an opportunity to understand the dynamics of faulting in a continental environment. The main shock and several aftershocks were well recorded teleseismically. Moreover, accelerograms were obtained for the main shock and aftershocks from stations in the epicentral area. This data set provides an opportunity to view the earthquakes in four spectral bands: long-period surface waves, long and short period teleseismic body waves and near field ground displacement. In addition, the large magnitude of several of the aftershocks relative to the main shock is a feature of this earthquake sequence that is not commonly observed in other seismic zones. From a tectonic point of view, knowledge of the mechanism of the earthquake is important in elucidating the mechanics of the collision of Africa and Eurasia.

This paper discusses various features of the source properties of the mainshock and aftershock of September 15, 1976 (09h 21m) which can be inferred from teleseismic long-period body wave and surface wave data. Fault mechanism, source depth and nature of fault rupture can be deduced from body waves. Additional data on the long-period nature of the source is available from surface waves. Finally, the long term pattern of seismic strain release in the region is revealed by the aftershock sequence.

TECTONIC SETTING

The Friuli-Venezia-Giulia Region of northeastern Italy extends from Austria on the north to the Adriatic Sea on the south and is bordered on the east by Yugoslavia. The region can be divided into several distinct topographic elements (Martinis, 1975). Along the Austrian border are the Carnic Alps, composed principally of Paleozoic rocks. South of the Carnic Alps are the largely Mesozoic Tolmezzo Alps in the western part of the area and the Julian Alps in the east. South of the latitude of the Tagliamento River, the mountains become lower in elevation. These ranges, known as the Pre-Alps, are underlain by Cenozoic flysch and molasse deposits. Between the Pre-Alps and the Adriatic Sea is the extensive Friuli Plain of Quaternary sediments. To the east, in Yugoslavia, the Dinaric Alps trend southeastward down the Balkan Peninsula.

The Carnic, Tolmezzo and Julian Alps, together with the Pre-Alps, constitute the Southern Alps in a geological sense (Angenheister et al., 1972). The Southern Alps are separated from the Eastern Alps by an important structural boundary (heavy dashed line in Fig. 1), the Periadriatic Line, which forms the northern boundary of the Carnic Alps (Angenheister et al., 1972; Martinis, 1975). In general, the Southern Alps have suffered less metamorphism and tectonism than the rocks north of the Periadriatic Line (Angenheister et al., 1972). In the Friuli region, the structural grain changes from northwest-southeast Dinaride trends near the border with Yugoslavia to more east-west trending structures of the Southern Alps in the west.

Throughout much of the Mesozoic, shallow water deposition of calcareous rocks occurred through the Friuli region (Martinis, 1975) although the presence of deep basins is indicated by pelagic sedimentation. Beginning in early Cenozoic times, the tectonic environment became more unstable.

Eocene flysch deposits, which now outcrop at the edge of the Friuli plain, mark the beginning of the Alpine orogeny which culminated in the Upper Miocene and Pliocene (Amato et al., 1976). Subaerial depositional environment has prevailed over the Friuli region from the Oligocene to the present.

The most important structural feature in the epicentral area is the so-called "Periadriatic Thrust" (Amato et al., 1976; Martinis, 1975) which is a complex zone of northward dipping thrust faults (Fig. 1). The Periadriatic Thrust is not to be confused with the Periadriatic Line (heavy dashed line in Fig. 1) mentioned above which structurally separates the Eastern and Southern Alps. In addition to the mapped faults which outcrop, a number of similar structures have been found in the subsurface of the Friuli Plain on seismic reflection profiles (Amato et al., 1976).

In a larger context, McKenzie (1972) suggests that the Adriatic Sea and the coastal areas of Italy and Yugoslavia form a tongue of the African plate which is underthrusting Eurasia in northeastern Italy and Yugoslavia. The African-Eurasian plate boundary is inferred from seismicity (Papazachos, 1973) to extend from Tunisia, through Sicily and the toe of Italy, up the Italian peninsula, across the southern Alps and down the coast of Yugoslavia (Fig. 1). Lort (1971) on the other hand, suggests that the Adriatic Sea is a separate microplate, the Apulian plate which may move independently of the larger plates. Except for the existence of a plate boundary across the mouth of the Adriatic Sea, the interpretations of Lort and McKenzie are similar. In both cases, compressional tectonics would be expected in northeastern Italy and adjacent Yugoslavia.

SEISMICITY

Northern Italy including the Friuli region was characterized as an area of low to moderate seismicity by Gutenberg and Richter (1954), although Karnik (1971, p. 184) was impressed with the activity in the Friuli region. Reports of historical earthquakes before 1900 have been collected by Ambraseys (1976a) and Karnik (1971). The most notable earthquakes were the shocks of 1348 and 1511. While the amount of damage due to these shocks was severe, both authors believe that none of the events exceeded magnitude 6-3/4. The severe damage caused by earthquakes in this region is due not so much to the large magnitude of the events but more because of poor construction techniques (Ambraseys, 1976a). The seismic activity of Friuli can be characterized by the occurrence of infrequent moderate earthquakes ($M_s < 7$) separated by long quiescent periods, with only minor seismicity.

According to Ambraseys (1976a) there have been only two earthquakes since 1900 with surface wave magnitude greater than 5.0 prior to the 1976 events (Table 1). An $m_b = 4.2$ (U.S.G.S.) shock occurred on March 24, 1975 and was followed by a series of shocks which were felt in the Tolmezzo region through April 25 (I.S.C. reports). The I.S.C. does not report any further events in the epicentral area until the foreshock of the Friuli earthquake on May 6, 1976.

The main shock (May 6, 1976, 20h 00m) was preceded by an $M_L = 4.5$ foreshock at 19h 59m and followed by a numerous series of aftershocks which decreased in magnitude and frequency until September 1976. The normal decay of the aftershock sequence was shattered by two pairs of strong earthquakes on September 11 (16h 31m and 16h 35m) and September 15 (03h 15m and 09h 21m). Seismic activity declined markedly after these earthquakes although a magnitude 5.1 shock occurred one year later in September 1977.

Unfortunately, there is some ambiguity concerning the location on the epicenter of the main shock relative to the aftershock distribution. Table 2 gives the hypocenter determinations of various agencies which are shown as stars on Fig. 3. The I.S.C.

locations of the larger aftershocks are shown in Fig. 2. While there is activity over a broad area, most aftershocks are concentrated within a roughly elliptically shaped region 30 km long by 18 km wide. Referring to Fig. 3, note that most of the agencies place the main shock near the eastern edge of the aftershock distribution (outlined by the dashed line), except Rome which puts the epicenter in the center of the distribution. To see if there are any systematic differences between Rome and I.S.C. locations, the positions of several of the larger, and presumably better located, aftershocks as reported by each group are plotted in Fig. 3. The arrows point from the I.S.C. location to the Rome location. There seems to be no consistent shift of epicenters determined by one agency to the epicenters computed by the other.

To help resolve these discrepancies in locations, the mainshock and two aftershocks were relocated relative to a third aftershock. Note that the Rome and I.S.C. epicenters of event 36 (September 11, 16h 31m) are quite close. This event was large and well recorded and was chosen as the master event. Using the relative location method implemented by Chung and Kanamori (1976) the locations of the main shock and aftershocks 46 and 13 relative to aftershock 36 were computed (shown as boxes in Fig. 3). There seem to be no gross errors in the method since in both cases, the relative location of the aftershocks are in the vicinity of the absolute locations determined both by Rome and I.S.C. The relative location places the main shock on the eastern edge of the aftershock distribution nearer to the I.S.C. location than to the epicenter of Rome.

There are several other points to be made about the aftershock distribution. First, the larger first-day aftershocks (shown as solid dots in Fig. 2) occur along the margins of the aftershock zone. Second, the September earthquakes (open boxes in Fig. 2) occur within the aftershock zone of the main event. These observations are in agreement with the conclusions of a more complete study of aftershock locations

by Cagnetti and Console (1977) who also show that the location of activity shifts during the course of the aftershock sequence. In a later section, the temporal pattern of energy release during the aftershock sequence will be examined.

BODY WAVE DATA

Many of the results of this paper are obtained by matching synthetic seismograms to observed records. To create synthetic seismograms, the response of a layered medium is convolved with operators describing source time history, attenuation and instrument response. The medium response can be computed using either generalized rays (Helmberger, 1974; Langston and Helmberger, 1975) or layer matrices (Haskell, 1962). At distances closer than about 30° , upper mantle structures create arrivals on seismograms which are not associated directly with the source properties of the earthquake. At distances greater than 85° , core effects begin to influence records. Thus, the distance window for P-wave observations is 30° to 85° and 45° to 80° for S-waves. Within these distance ranges, the effect of the mantle on the records is mainly due to anelastic attenuation and geometrical spreading. Futterman's (1962) Q-operator was used to construct the attenuation operator. Initially $T/Q = 1.0$ sec for P-waves and $T/Q = 4.0$ sec for S-waves was used. Because of the uncertainty of the S-wave attenuation, other values of T/Q were tried; the results of these experiments are described later.

The main shock on May 6, 1976 and the aftershock of September 15, 1976 were, at best, moderate sized earthquakes but nonetheless were well recorded by WWSSN stations around the world. Stations to be used for the body and surface wave analysis were chosen based on clarity of recording and absence of long-period noise. Station information is listed in Table 3. Relevant portions of the seismograms were digitized on an electronic digitizing table and then detrended and interpolated by computer.

P and S waves were corrected for instrumental magnification and plotted at uniform time scale. East-west and north-south components of the S-waves were rotated to obtain pure SH and SV records.

LONG-PERIOD BODY WAVES

The first step in computing synthetic body-wave seismograms is to prepare a focal mechanism solution. P-wave first motions were read on long-period vertical seismographs of the WWSSN and other stations. For the main shock (Fig. 4), the available data define the steeply dipping nodal plane quite well, while the other plane is almost completely unconstrained.

In cases in which the orientation of one nodal plane is ambiguous, S-waves can often be used to fix the location of the unknown plane. The technique of S-wave polarization is well-known (e.g., Muller, 1977). In this paper, SV and SH synthetic seismograms will be computed for various trial orientations and compared to the observed records. The trial mechanism which gives the most consistent fits is inferred to be the correct focal mechanism. This procedure is really an extension of the polarization method in that the whole wave-form and not just certain amplitude measurements are used.

Because factors such as source depth and duration, in addition to focal mechanism, influence the wave forms of S, it is necessary to have some estimates of these quantities before determining the mechanism. Fortunately, the focal mechanism and station distribution for the main shock allow us to pick stations at which the P-wave is not particularly sensitive to the orientation of the shallowly dipping (and originally unknown) nodal plane. Examining the focal mechanism on Fig. 7 we can see that stations such as MSO, BLA, HKC will always be near the maximum of the P-wave radiation pattern for any possible orientation of the shallowly-dipping plane. By calculating synthetic P-waves

for various depth and time function combinations (an example is shown in Fig. 5) we find that the observed records are best fit with a 4.5 sec trapezoidal time function at a source depth of 8 to 10 km.

With the source depth, time function and orientation of one nodal plane known, S-waves can be used to determine the position of the second nodal plane in the manner described above. Figure 6 shows representative SH and SV waves for various rake angles corresponding to different orientations of the shallowly dipping nodal plane; the steep plane is fixed at strike = 76° and dip = 75° S. The best agreement is for a rake of about 80° , corresponding to a plane striking 86° and dipping 15° N.

Console (1976), Ebblin (1976) and Muller (1977) have also published mechanisms for the main shock. In each mechanism, the position of the steep, southeast dipping plane is in good agreement with the results of this study. Muller used S-wave polarization techniques to determine the orientation of the second plane which he finds dips shallowly to the northwest. In Ebblin's mechanism, the second plane dips shallowly west-northwest, constrained by a single nearby station. In contrast, the results of this paper indicate that the fault plane dips almost due north at a very shallow angle.

After the mechanism and depth of the earthquake have been determined, the next step is to include the effect of crustal structure in the synthetic waveforms. Angenheister et al. (1972) have published a north-south velocity profile for the southern Alps based on nearby refraction lines. Their structure has an upper crustal velocity of 6.0 km/sec extending to about 23 km interrupted by a low-velocity layer from 12 to 20 km. This low-velocity zone is quite prominent near the Alpine axis, but rather weak in the Friuli region. Below 23 km, the velocity increases to 6.8 km/sec at 30 km, to 7.0 km/sec at 36 km and finally 8.0 km/sec at about 44 km. A model based on

an unreversed refraction profile through the epicentral area has been published by Finetti and Morelli (1972). Their model has an upper crustal velocity of 5.85 km/sec to 12.4 km, below which 6.2 km/sec material extends to 28 km. The lower crust has a velocity of 7.0 km/sec. Mantle velocity of 8.0 km/sec is reached at 45 km. In most important respects this model is similar to the model of Angenheister et al. (1972). In particular, the presence of rather high velocity (7.0 km/sec) material just above the Moho in both models is required to reduce strong phases reflected between the Moho and the free surface which are then radiated to teleseismic distances. These phases arise on synthetic records when there is too large a velocity contrast across the Moho; they are not observed on the real seismograms. The Angenheister et al. (1972) model was divided into discrete layers for use in the synthetic seismogram program and the low-velocity zone, which is not very pronounced in the Friuli region, was eliminated. S-wave velocities were calculated from the P-wave velocities by assuming a Poisson's ratio of 0.25. The resulting model is given in Table 4.

The matrix method of Haskell (1962) was used to compute the response of the layered crust to an embedded point source. By convolving the crustal response with a Q-operator, far-field source time history and instrument response, realistic synthetic seismograms are created which can be compared directly to the observed records.

Figure 7 shows the observed records (heavy lines) and synthetics (light lines) computed for a source at 8 km depth in the Angenheister et al. (1972) structure. The overall agreement between synthetic and observed records is quite good indicating that the basic parameters of the model are reasonable. Rather significant discrepancies occur for stations near nodal lines (AAE, BUL, SHI) and for most stations after the first 15 sec. Nodal stations are

especially sensitive to radiation pattern and undoubtedly some of these discrepancies are due to the simple point source model used to compute the synthetics. It is easy to imagine irregular fault propagation with the fault orientation changing as the rupture proceeds. In addition, the real earth is certainly not as simple as the structure used nor have any effects of the crust at the receiving station been taken into account.

S-wave data has already been used to constrain the focal mechanism. Figures 8a and b show the observed synthetic SH and SV waves for the main shock. The synthetics have been computed for the same model used for the P-waves except that the length of the time function has been increased to 5.5 sec to better match the observed S-wave duration. The overall fit between observed S-waves and synthetic records is good indicating that the source model is reasonable. With the exception of the SH-wave at PRE (Fig. 8a), which is on a nodal line, the seismic moments calculated from the SH data are somewhat low compared to the P-wave moments. The above calculations were done assuming $T/Q = 4.0$ sec. Burdick and Mellman (1976) have suggested that T/Q for S-waves should be 5.3 sec from the study of the Borrego Mountain, California earthquake. S-wave synthetics for the model with $T/Q = 5.3$ sec and $t_c = 4.5$ sec (the P-wave value) are almost indistinguishable from the model presented in Fig. 8a ($T/Q = 4.0$, $t_c = 5.5$), except that the SH moments for the $T/Q = 5.3$ sec model are in somewhat better agreement with the P-wave moments.

The interpretation of the body wave seismograms of the aftershock of September 15, 1976 at 09h 21m proceeds in the same manner as for the main shock. Like the mainshock, the orientation of the steeply dipping plane of the aftershock was fixed by P-wave observations and the orthogonal plane was determined from S-waves. The mechanism is shown in Fig. 9. The strike and

dip of the steep plane are 56° and 67°S , respectively. The shallowly dipping plane shown in Fig. 9 corresponds to a rake of 70° . Observed and synthetic P and S waves are compared in Figs. 10 and 11. The mechanisms of the mainshock and aftershocks are similar, as are the depths, around 8 km. The far-field time function of the aftershock has a duration of 3 to 3.5 sec whereas the mainshock is about 4.5 sec duration. The aftershock P-wave moment is 1.0×10^{25} dyne-cm compared to 2.9×10^{25} dyne-cm for the mainshock.

The regional tectonics, in particular the mapped east-west striking thrust faults (Fig. 1), suggest that for both the mainshock and aftershock the shallow, northward dipping nodal plane is the fault plane. In the case of the main shock, the roughly elliptically shaped aftershock distribution (Fig. 2) also suggests that the shallowly dipping nodal plane is the fault plane (Cagnetti and Console, 1977). In this case, the fault motion is nearly pure dip-slip with the northern block (Alps) overthrusting the sedimentary basin. The shallowly dipping plane of the 09h 21m aftershock mechanism is similar in orientation to that of the main shock, but the slip vector is more oblique.

A focal mechanism has also been prepared for the large aftershock which occurred at 03h 15m on September 15 (Fig. 9). Because the P-waves are small to begin with and because they are somewhat obscured by noise from a previous event, good first-motion readings are rare. Nevertheless, it is clear that the mechanism of this earthquake is somewhat different than the others studied in this paper. Certain stations are clearly reversed. An important observation was made by Ritsema (1976) on long-period vertical seismographs at de Bilt, the Netherlands. He observed a clear change in polarity between the main shock and 09h 21m aftershock on one hand and the

03h 15m shock on the other. Focal mechanisms for both aftershocks are shown in Fig. 9. Because of the noise present on the seismograms, no attempt was made to model the long-period body waves.

The mechanism of the 03h 15m aftershock appears to represent predominantly dip-slip fault motion, but with a considerable strike-slip component. In contrast to the other mechanism in which the nodal planes strike nearly east-west, the focal planes of this aftershock strike north and northeast. There are no major northeast-southwest striking structures in the area, although Marinis (1975, his Fig. 13) does indicate several minor north-south trending lineations.

The mechanisms determined in this paper are somewhat different from mechanisms published for earlier earthquakes in the Friuli region. McKenzie (1972) suggests that the event of October 18, 1936 had a normal faulting mechanism, although Ahorner et al. (1972) present a strike-slip mechanism for this earthquake. Mayer-Rosa et al. (1976) studied the mechanism for the event of March 24, 1975 ($m_b = 4.2$, U.S.G.S.). Because it was quite small, there is considerable ambiguity in the solution. The event is either strike-slip or, as Mayer-Rosa et al. prefer, thrust on an almost east-west striking fault plane.

FINITE FAULT

Up to this point, the body wave records have been interpreted using synthetic seismograms computed for a point source in a layered halfspace. Two assumptions are made in computing point source synthetics. The first is that the same time function is used for each ray (e.g., P, pP, sP, etc.) and the second is that the same time function is used for all azimuths and take-off angles. For an arbitrarily oriented, propagating shear fault, these assumptions are invalid. In the first place, P and S rays each require a

different time function and secondly, the time function observed at any point is dependent on the angle between the direction of rupture propagation and the take-off angle (Savage, 1966).

It is the purpose of this section to investigate the nature of fault propagation during the Friuli main shock using the formulation of Heaton (1978) which allows arbitrarily complex faulting histories. In the present discussion, we will try to place constraints on the fault area and mode of rupture propagation, either unilateral or bilateral. To simplify the problem, it is assumed that the shallowly dipping nodal plane of Fig. 4 is the fault plane, that the dislocation is uniform over the entire fault surface and that the rupture velocity is 3.0 km/sec. Furthermore, the shape of the fault plane is a square and the dislocation rise time is 1 sec. The six cases investigated are shown in Fig. 12; the heavy broken line is the approximate limit of aftershock concentration from Fig. 2, and the stars represent the epicenters as determined by various agencies. In the

upper part of Fig. 12, the square fault planes are centered on the epicenter determined by Roma which is near the middle of the aftershock distribution. Three cases, fault lengths of 8, 16 and 24 km, are computed. The superposition of the theoretical fault planes on the aftershock distribution is rather arbitrary, but it does give a sense of scale. The lower part of Fig. 12 shows the case in which the fault originates at one corner of the fault plane and propagates unilaterally updip and towards the west. The NEIS and ISC epicenters are near the northeast (down-dip) corner of the aftershock distribution.

Synthetics for the six cases are shown in Figure 13 and 14. The model which best fits the P-waves seems to be case c. The observed data do not change very much with azimuth. As expected, the symmetrically expanding cases (a,b,c) reproduce this effect quite well. This is in contrast to the unilateral faults, especially case f, which exhibit strong azimuthal variation. Unilateral propagation cannot be ruled out, however. For instance, case e fits the P-wave data almost as well as case c. What can be said instead is that there cannot be a strong propagation effect. Nor can the fault plane be substantially smaller than the aftershock area. Cases a and d give rise to synthetic seismograms which are much too narrow in duration compared to the observed data. From these results the probable fault length is 16 to 24 km but whether faulting initiated at the center or edge of the zone cannot be determined.

Additional constraint on the rupture mechanism is provided by SH waves (Figure 14). Again, case f with strong azimuthal variation is ruled out by the data as are the cases with small fault planes (cases a, d). It must be kept in mind that the uncertainty in the value of attenuation for S-waves can have considerable effect on pulse width.

RAYLEIGH WAVE DATA

An independent estimate of the focal mechanism and seismic moment is provided by surface waves. In this study, the observed spectral density of 100 second Rayleigh waves are compared to theoretical values calculated using the tables published by Ben Menahem et al. (1970). The observed data were prepared by first digitizing the seismogram in a group velocity window between 4.0 and 3.5 km/sec, then detrending and interpolating to a uniform time interval. The spectral density was obtained by a fast Fourier transform program. The spectrum was corrected for instrument response according to the formulation of Hagiwara (1958) and normalized to a propagation distance of 90° using the equation.

$$\sqrt{\frac{\sin \frac{\Delta}{a}}{\sin \frac{\Delta_0}{a}}} \exp [\gamma(\Delta - \Delta_0)]$$

where Δ = epicentral distance

Δ_0 = normalized distance ($= 90^\circ$)

a = Earth radius

γ = attenuation coefficient

The attenuation coefficients of Ben Menahem et al. (1970) are used.

In Figure 15 the observed values of spectral density for 100 sec Rayleigh waves are compared to the theoretical radiation pattern computed for the source model found using body waves (strike = 76°, dip = 75°, rake = 80°, depth = 10 km). The good agreement between the observed data and theoretical calculations indicate that the overall deformation recorded by 100 sec waves is the same as that recorded by ~15 sec waves.

However, the seismic moment determined from 100 sec surface waves is 5×10^{25} dyne-cm, somewhat higher than the value of 2.9×10^{25} dyne-cm found for body waves.

DISCUSSION

A notable feature of the Friuli earthquake sequence is the large size of the September aftershocks relative to the mainshock. The seismic moment of the September 15 (09h 21m) aftershock studied in this paper is nearly one-third the moment of the mainshock. Besides that earthquake, there were three other large events between September 11 and 15, 1976 (Table 1). To provide a quantitative measure of the energy release of the aftershock series, the seismic moment (M_o) can be estimated from local magnitude (M_L) using the relation $\log M_o = 15 + 1.7 M_L$ (Wyss and Brune, 1968). The moment sum of the Friuli earthquake sequence from May 1976 through December 1977 is slightly over 8×10^{25} dyne-cm, of which 3×10^{25} dyne-cm was released during the main shock (Fig. 16). Thus, the aftershock sequence was considerably more energetic than the main shock. In contrast to the Friuli series, Hadley and Kanamori (1978) estimated the moment sum of the aftershocks of the 1971 San Fernando earthquake to be about 3.5×10^{24} dyne-cm, nearly two orders of magnitude smaller than the main shock. Also shown in Fig. 16 is an enlargement of the energy-release curve for the first 100 days of aftershock activity. This curve is directly comparable to Fig. 2 of Hadley and Kanamori (1978). Comparing the two diagrams, note that moment sum for Friuli sequence is somewhat larger than for San Fernando, and that most of the energy release came during two large earthquakes. It appears that the mechanical properties of the San Fernando and Friuli seismic zones are rather different. In the case of San Fernando, most of the energy was released by a single large earthquake. For Friuli, the seismic energy was liberated in a series of smaller earthquakes.

There are tantalizing hints of similar behavior during past earthquakes. For the earthquake of March 26, 1511, in particular, felt reports collected by Ambraseys (1976a,b) mention that the main shock was followed by a series of strong aftershocks, especially those of June 6 and August 8, 1511.

Finetti et al. (1979) have postulated a rather detailed history for the Friuli sequence involving various mapped tectonic structures. Given the uncertainty in depth and location of the earthquakes (Cagnetti and Console, 1977), it is premature to try to assign any one shock to any particular structure. It is reasonable to propose, however, that the mainshock relieved the stress in one part of the fault zone and that the large September aftershock occurred in another part of the fault zone.

The historic earthquakes are not concentrated just in the Friuli region, but scatter over a wide area, about 200 km east to west (Ambraseys, 1976a). Ambraseys noted that activity seemed to alternate from one region to another over a period of several hundred years. Perhaps just as significant is that the events more or less span the width of the plate margin postulated by Lort (1971) and McKenzie (1972) (Fig. 1). This is certainly not a subduction zone in the classical sense. More likely, this zone of seismicity is one of several areas of crustal shortening caused by the collision of Africa and Eurasia.

Knowing the seismic moment and fault area, the dislocation (D_0) and stress drop ($\Delta\sigma$) can be estimated for the mainshock and aftershock. Using the formula for moment:

$$M_0 = \mu D_0 S = 4 \times 10^{25} \text{ dyne-cm}$$
 where S is the fault area (about 20 km by 20 km) and μ is the rigidity ($= 3 \times 10^{11}$ dynes/cm 2), D_0 is calculated to be 33 cm for the mainshock. For a circular fault, the stress drop is given by
$$\Delta\sigma = (7\pi/16)(\mu D_0/a)$$
 where a is the fault radius (Kanamori and Anderson, 1975). Using this formula, the stress drop is estimated to be 12 bars, with $a = 11.3$ km (the radius of a 400 km 2 circle) and the above value of D_0 . These values of dislocation and stress drop are similar to those computed by Caputo (1976), using somewhat different methods.

For the aftershock, the fault area is about 10 km x 10 km from a comparison of observed records to finite fault models. Using the moment

of 1×10^{25} dyne-cm, the dislocation is estimated to be 33 cm, with a stress drop of 24 bars. It is interesting to note that these stress drops are similar to stress drops of inter-plate earthquakes (Kanamori and Anderson, 1975) even though the plate margin here is not well-defined.

CONCLUSIONS

In this paper, I have presented source models for two earthquakes of the 1976 Friuli, Italy sequence: the main shock and aftershock of September 15, 09h 21m. The mechanisms of both earthquakes are similar. Regional geology and aftershock distribution suggests that the plane which dips gently to the north is the fault plane. This plane represents thrusting of the Alps over the sedimentary basin to the south. Both events occur at about 6 to 10 km depth and have moments of 3×10^{25} dyne-cm for the main shock and 1×10^{25} dyne-cm for the aftershock. No strong effects of fault propagation are present in the data suggesting either that the rupture began near the middle of the fault plane and expanded outward uniformly or if the rupture began at one edge of the plane, the length of fault propagation was rather small. Synthetic seismogram calculations including the effect of source finiteness indicate that the fault length for the main shock is about 16 to 20 km. Using the above values of seismic moment and fault area, the dislocation is estimated to be 33 cm and the stress drop 12 bars for the main shock. For the aftershock, these quantities are 33 km and 24 bars, respectively.

The large size of the aftershock series which began in September suggests that these events occurred in another part of the fault zone than the main shock. Energy release during the Friuli earthquake sequence occurred in a main shock followed by several large aftershocks over the course of several months. In contrast, most of the energy released during the 1971 San Fernando, California earthquake was liberated by the main shock, with only a minor

contribution from the aftershock sequence. The mechanism determined for the mainshock is consistent with plate tectonic interpretations of Lort (1971) and McKenzie (1972).

ACKNOWLEDGEMENTS

The author wishes to thank John Ebel, Don Helmberger, Jim Pechmann, and Terry Wallace for critically reading the manuscript. Tom Heaton generously provided his program to compute finite fault synthetics. Laszlo Lenches and Joe Galvan drafted the figures.

This research was sponsored by National Science Foundation Grant No. EAR78-14786. Contribution No. 3320, Division of Geological and Planetary Sciences, California Institute of Technology, Pasadena, California 91125.

REFERENCES

- Ahorner, L., H. Murawski and G. Schneider (1972). Seismotektonische traverse von der Nordsee bis zum Apennin, Geol. Runds., 61, 915-942.
- Amato, A., P. F. Barnaba, I. Finetti, G. Groppi, B. Martinis and A. Muzzini (1976). Geodynamic outline and seismicity of Friuli-Venetia-Julia region, Bull. Geof. Teor. ed. Appl., 18, 217-256.
- Ambraseys, N. N. (1976a). The Gemona di Friuli earthquake of 6 May 1976, in The Gemona di Friuli Earthquake of 6 May 1976, UNESCO Technical Report RP/1975-76/2.222.3, Paris, France.
- Ambraseys, N. N. (1976b). Engineering seismology aspects of the Gemona-Friuli earthquake, Bull. di Geof. Teor. ed Appl., 18, 257-272.
- Angenheister, G., H. Bögel, H. Gebrände, P. Giese, P. Schmidt-Thomé and W. Zeil (1972). Recent investigations of surficial and deeper crustal structures of the Eastern and Southern Alps, Geol. Runds., 61, 349-395.
- Ben Menahem, A., M. Rosenman and D. G. Harkrider (1970). Fast evaluation of source parameters from isolated surface-wave signals, Bull. Seism. Soc. Am., 60, 1337-1387.
- Burdick, L. J. and G. R. Mallman (1976). Inversion of the body waves from the Borrego Mountain earthquake to the source mechanism, Bull. Seism. Soc. Am., 66, 1485-1499.
- Cagnetti, V. and R. Console (1977). Space-time distribution of the Friuli (1976) earthquakes, Ann. di Geof., 30, 107-184.
- Caputo, M. (1976). The area of the fault, the dislocation, the stress drop and the seismic moment of the Friuli earthquake of May 6th, 1976, Ann. di Geof., 29, 171-178.
- Chung, W. Y. and H. Kanamori (1976). Source process and tectonic implications of the Spanish deep-focus earthquake of March 29, 1954, Phys. Earth and Planet. Int., 13, 85-96.

- Console, R. (1976). Mecchanismo focale dal terremoto del Friuli del 6 Maggio 1976, Ann. di Geof., 29, 165-170.
- Console, R. and C. Gasparini (1976). Hypocentral parameters for the Friuli, May 6th 1976 earthquake, Ann. di Geof., 29, 153-159, in Italian.
- Ebblin, C. (1976). Orientation of stresses and strains in the Piedmont area of eastern Friuli, NE Italy, Boll. di Geof., 18, 559-579
- Finetti, I. and C. Morelli (1972). Deep seismic refraction exploration on Eastern Alps, Bull. Geof. Teor. ed Appl., 14, 59-66.
- Finetti, I., M. Russi and D. Slepko (1979). The Friuli earthquake (1976-1977), Tectonophysics, 53, 261-272.
- Futterman, W. I. (1962). Dispersive body waves, Jour. Geophys. Res., 67, 5279-5291.
- Gutenberg, B. and C. F. Richter (1954). Seismicity of the Earth, Hafner Publ. Co., New York, 310 pp.
- Gwinner, M. P. (1971). Geologie der Alpen, Schweizesbart, Stuttgart, 477 pp.
- Hadley, D. and H. Kanamori (1978). Recent seismicity in the San Fernando region and tectonics in the west-central Transverse Ranges, California, Bull. Seism. Soc. Am., 68, 1449-1457.
- Hagiwara, T. (1958). A note on the theory of the electromagnetic seismograph, Bull. Earthq. Res. Inst., 36, 139-164.
- Haskell, N. A. (1962). Crustal reflection of plane P and SV waves, J. Geophys. Res., 67, 4751-4767.
- Heaton, T. H. (1978). Ph.D. Thesis, California Institute of Technology, Pasadena, California 91125.

- Heimberger, D. V. (1974). Generalized ray theory for shear dislocations, Bull. Seism. Soc. Am., 64, 45-64.
- Kanamori, H. and D. L. Anderson (1975). Theoretical basis for some empirical relations in seismology, Bull. Seism. Soc. Am., 65, 1073-1095
- Karnik, V. (1971). Seismicity of the European Area, Part II, D. Reidel Publ. Co., Dordrecht-Holland, 218 pp.
- Langston, C. A. and D. V. Heimberger (1975). A procedure for modeling shallow dislocation sources, Geophys. J. Roy. astr. Soc., 62, 117-130.
- Lort, J. M. (1971). The tectonics of the eastern Mediterranean: a geophysical review, Rev. Geophys. Space Phys., 9, 189-216.
- Martinis, B. (1975). The Friulian and Julian Alps and Pre-Alps, Chapter 2 in Structural Model of Italy, L. Ogniben, M. Parotto and A. Procurton (eds.), Consiglio Nazionale delle Ricerche, Rome.
- Mayer-Rosa, D., N. Pavoni, R. Graf and B. Rast (1976). Investigations of intensities, aftershock statistics and the focal mechanism of Friuli earthquakes in 1975 and 1976, Pure and Appl. Geophys., 114, 1095-1103.
- McKenzie, D. P. (1972). Active tectonics of the Mediterranean Region, Geophys. J. Roy. astr. Soc., 30, 109-185.
- Muller, G. (1977). Fault-plane solution of the earthquake in northern Italy, 6 May 1976, and implications for the tectonics of the eastern Alps, J. Geophys., 42, 343-349.
- Papazachos, B. C. (1973). Distribution of seismic foci in the Mediterranean and surrounding area and its tectonic implications, Geophys. J. Roy. astr. Soc., 33, 421-430.
- Ritsema, A. R. (1976). Preliminary analysis of Friuli earthquake records, Bull. di Geof. Teor. ed Appl., 18, 875-887.
- Savage, J. C. (1966). Radiation from a realistic model of faulting, Bull. Seism. Soc. Am., 56, 577-592.
- Wyss, M. and J. N. Brune (1968). Seismic moment, stress and source dimensions for earthquakes in the California-Nevada region, J. Geophys. Res., 73, 4681-4695

Table 1. Significant Earthquakes in the Friuli Region.

No.	Year	Month	Day	Hour	Min	Lat., °N	Long., °E	Depth	m_b	M_s	Ref.
1348		Jan.	25			46.5	13.4				Ambraseys, 1976
1511		March	26			46.2	13.6				"
1928		March	27	08h	32m	46.41	13.08	25	5.8		"
1936		Oct.	18	03h	10m	46.04	12.40	15	5.7		"
1975		March	24	02h	33m	46.29	13.13	21			NEIS
0	1976	May	6	19h	59m	46.201	13.262	33N	4.5		"
1		May	6	20h	00m	46.36	13.28	9	6.0	6.5	"
13		May	11	22h	44m	46.27	12.99	11	5.2		"
36		Sept.	11	16h	31m	46.28	13.16	16	5.2	5.5	"
37		Sept.	11	16h	35m	46.30	13.20	20	5.3	5.4	"
42		Sept.	15	03h	15m	46.30	13.20	10G	5.7	6.0	"
46		Sept.	15	09h	21m	46.32	13.13	17	5.4	5.9	"
1977		Sept.	16	23h	48m	46.27	12.97	25	5.1	5.1	"

Table 2. Main Shock Hypocenter Determinations, May 6, 1976

Agency	hour	min	sec	Lat., °N	Long., °E	Depth	m_b	M_s	M_L
NEIS	20h	00m		11.6	46.356	13.275	9	6.0	6.5
ISC				12.5	46.35	13.26	12	5.9	
Rome #1				12.2	46.15	13.11	26		6.2
Rome #2				8.6	46.29	13.13		Mag=6.4	
CSEM				14.7	46.31	13.31	10		
C.&G. #1				11.278	46.253	13.240		8.19	
C.&G. #2				12.585	46.250	13.231		9.995	

NEIS: National Earthquake Information Service, Preliminary Determination of Epicenters, Monthly Listing

ISC: International Seismological Centre, Edinburgh, Scotland

Rome: Istituto Nazionale di Geofisica, Rome

CSEM: Centre seismologique Europeo-Mediterranean

C.&G.: Console and Gasparini (1976)

Table 3. Station Data

105

Station	Delta (deg)	Azimuth (deg)	Back Azimuth (deg)	Station	Delta (deg)	Azimuth (deg)	Back Azimuth (deg)
AAE	43.1	141.5	334.2	SHA	75.6	299.5	44.4
ALQ	82.5	314.0	37.3	SHI	34.7	104.7	309.8
ANP	83.7	59.8	318.7	SNG	83.0	86.8	315.9
BEC	59.6	286.4	51.7	WES	57.8	299.4	54.5
BLA	66.5	299.8	48.8				
BOG	84.9	271.5	44.0				
BUL	67.6	164.4	348.6				
CAR	75.7	270.4	44.7				
CHG	73.7	79.6	314.1				
COR	81.6	330.3	28.7				
COL	68.1	351.4	14.0				
DAV	99.9	68.6	319.5				
DUG	81.3	321.3	34.4				
GOL	78.3	316.4	38.3				
HKC	81.3	66.8	316.6				
KTG	29.6	336.8	125.9				
LON	79.3	330.5	29.8				
LPB	96.0	252.7	43.6				
MAT	83.8	41.5	325.3				
MSH	35.7	89.4	301.0				
MSO	76.3	325.8	34.5				
NAT	51.8	149.4	339.4				
PRE	73.0	163.9	349.2				
QUE	44.3	91.9	307.0				

Table 4. Crustal Model (after Angenheister et al., 1972)

Layer	P-Wave Vel. (km/sec)	S-Wave Vel. (km/sec)	Density (gr/cc)	Thickness (km)	Depth (km)
1	6.0	3.47	2.60	22.0	0.0
2	6.2	3.58	2.66	2.4	22.0
3	6.4	3.70	2.72	1.2	24.4
4	6.6	3.81	2.78	2.4	25.6
5	6.8	3.93	2.84	6.0	28.0
6	7.0	4.05	2.90	8.0	34.0
7	8.0	4.62	3.20	-	42.0

Figure 1. Geological and plate tectonic setting of the Friuli earthquake sequence. The upper figure shows the geology after Gwinner (1971). The star near the center of the figure shows the ISC location of the main shock. The heavy dashed line along the Gail River is the Periadriatic Lineament (see text). Geological units are: (1) Quaternary; (2) Miocene molasse, (3) Eocene-Oligocene flysch, (4) Cretaceous carbonate, (5) Jurassic undivided, (6) middle and upper Triassic, (7) Triassic and Permian, (8) Paleozoic of the Carnic Alps, (9) quartz phyllite, (10) crystalline rocks of the eastern Alps, (11) thrust fault. The lower figure shows the plate tectonic interpretation of McKenzie (1972) and Lort (1971). The dashed line represents the inferred southwestern boundary of the Apulian plate. Arrows indicate direction of plate motion.

Figure 2. Epicenters of the main shock and larger aftershocks of the Friuli earthquake sequence as reported by the ISC. Large star indicates the main shock. Closed circles represent aftershocks which occurred within the first twenty-four hours and open circles are later aftershocks up to September 11. Smaller stars are epicenters of the two largest earthquakes on September 15. Open squares are aftershocks of these events. Focal mechanisms are determined in this paper with compressional quadrants shaded. Heavy dashed line denotes the approximate limit of aftershock concentration. Triangles are accelerograph stations.

Figure 3. Locations of the main shock and largest aftershocks. Main shock epicenters determined by various agencies are indicated by stars (Table 2). Aftershock epicenters (numbers correspond to Table 1) calculated by ISC and Roma are indicated by open circles; arrows point from ISC location to Roma location. Filled squares

indicate locations of main shock and aftershocks 13 and 46 relative to aftershock 36 determined in this paper.

Figure 4. P-wave focal mechanism of main shock of May 6, 1976. Data read on WWSSN long-period vertical seismographs and on other long-period stations in Europe and plotted on lower half of focal sphere. Shallowly dipping plane is constrained by S-wave data.

Figure 5. Examples of synthetic wave-forms computed for several combinations of source depth (h) and time function (t_c).

Figure 6. Determination of shallowly dipping nodal plane using S-wave data. Note variation of SH-wave synthetics at MSO and SV-wave synthetics at BLA with change in rake angle. Best estimate is that the rake angle lies between 80° and 90° , corresponding to almost pure dip-slip fault mechanism.

Figure 7. Observed P-waves (dark line) for main shock compared to synthetics (light line) computed for a point source at 8 km depth within the structure given in Table 4. Strike (ϕ), dip (δ), rake (λ), depth (h), average moment (M_0) and time function (t_c) are indicated.

Figure 8. SH and SV waves recorded from the Friuli earthquake compared to (a,b) synthetics computed for a point source within a halfspace. Attenuation is controlled by the ratio T/Q which is 4.0 sec for this case; time function is 5.5 sec duration. Other notation same as Fig.7.

Figure 9. P-wave nodal diagram for September 15, 1976 aftershocks at 03h 15m and 09h 21m. Data read from WWSSN long-period vertical records along with some auxiliary stations and plotted on lower half of focal sphere.

Figure 10. Observed and synthetic P-waves for the aftershock of 09h 21m, September 15, 1976. Synthetics are computed for a point source at 6 km depth in the Angenheister et al. (1972) structure (Table 4). Notation is the same as Figure 7.

Figure 11. S-waves for the aftershock of 09h 21m showing observed and synthetic records and SH and SV radiation patterns.

Figure 12. Fault models used for the finite fault calculations. Six cases are shown corresponding to square faults of length 8, 16 and 24 km. In the upper part of the figure, the theoretical fault planes are centered on the epicenter determined by Rome which lies near the center of the aftershock distribution. The lower part shows the same fault planes, only now aligned so that the upper right corner (northeast) is near the NEIS and ISC epicenters. Dashed line indicating the limits of aftershock concentration gives a sense of scale.

Figure 13. Observed P-waves of four stations compared to synthetics computed for finite fault models a through f.

Figure 14. Observed SH-waves compared to synthetics computed for the finite fault models.

Figure 15. Observed spectral density of 100 sec Rayleigh waves radiated by main shock compared to theoretical pattern for focal mechanism shown in Fig. 4. Seismic moment is 5×10^{25} dyne-cm.

Figure 16. Summation of seismic moment with time for earthquakes of the Friuli sequence calculated from an empirical relation between local magnitude and seismic moment.

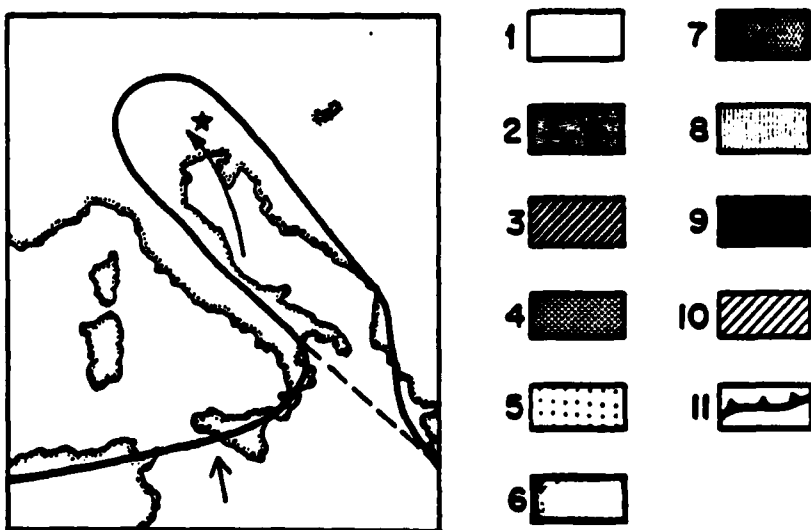
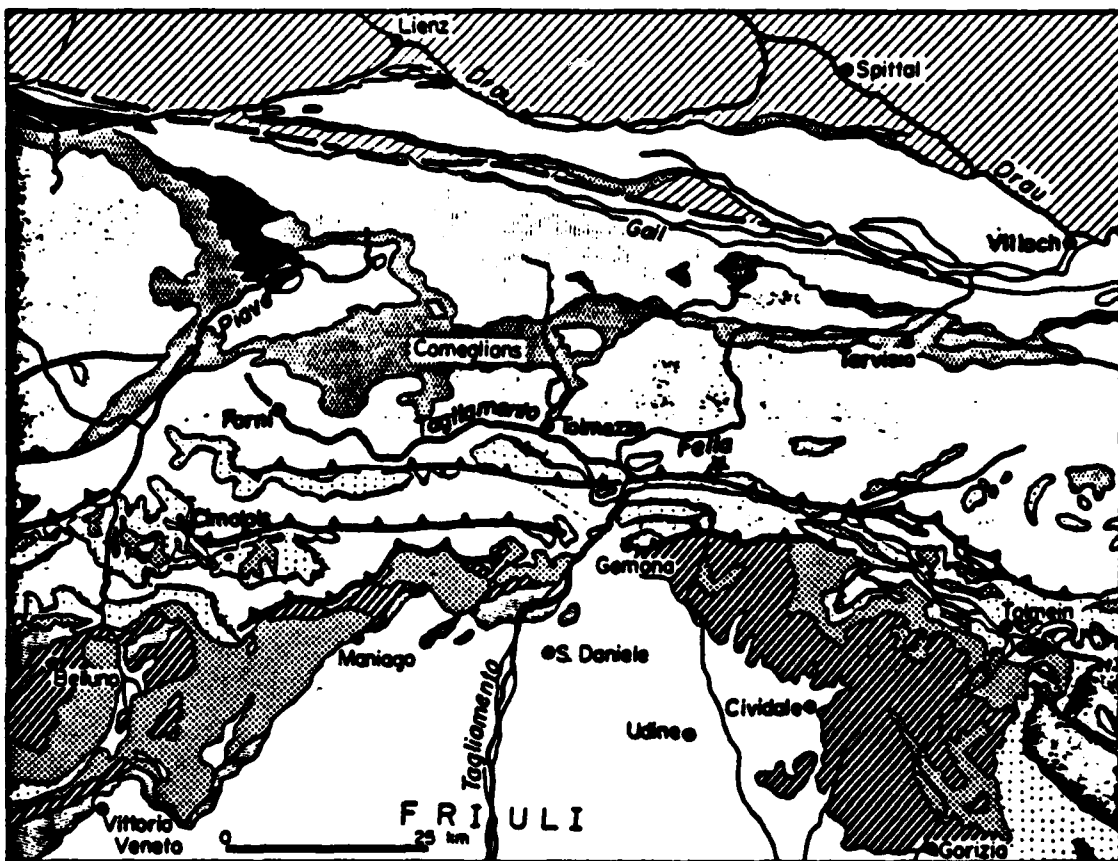


Fig. 1

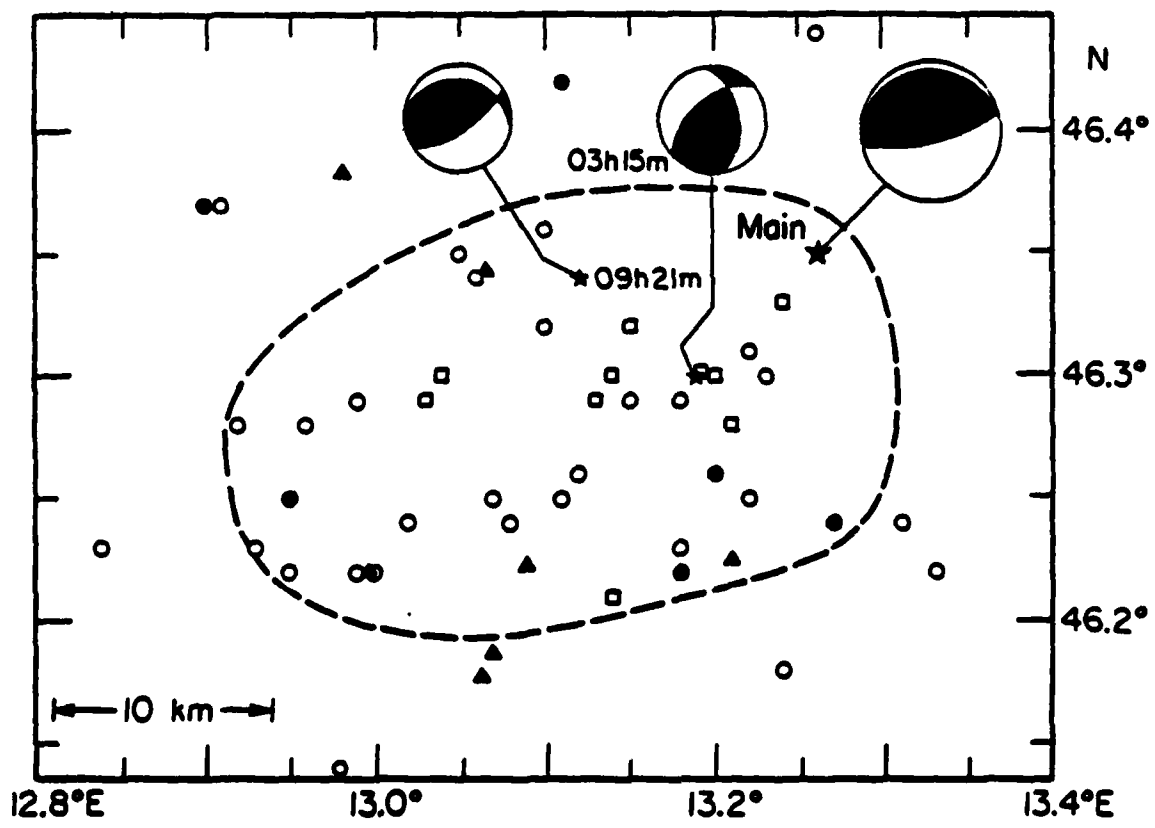


Fig. 2

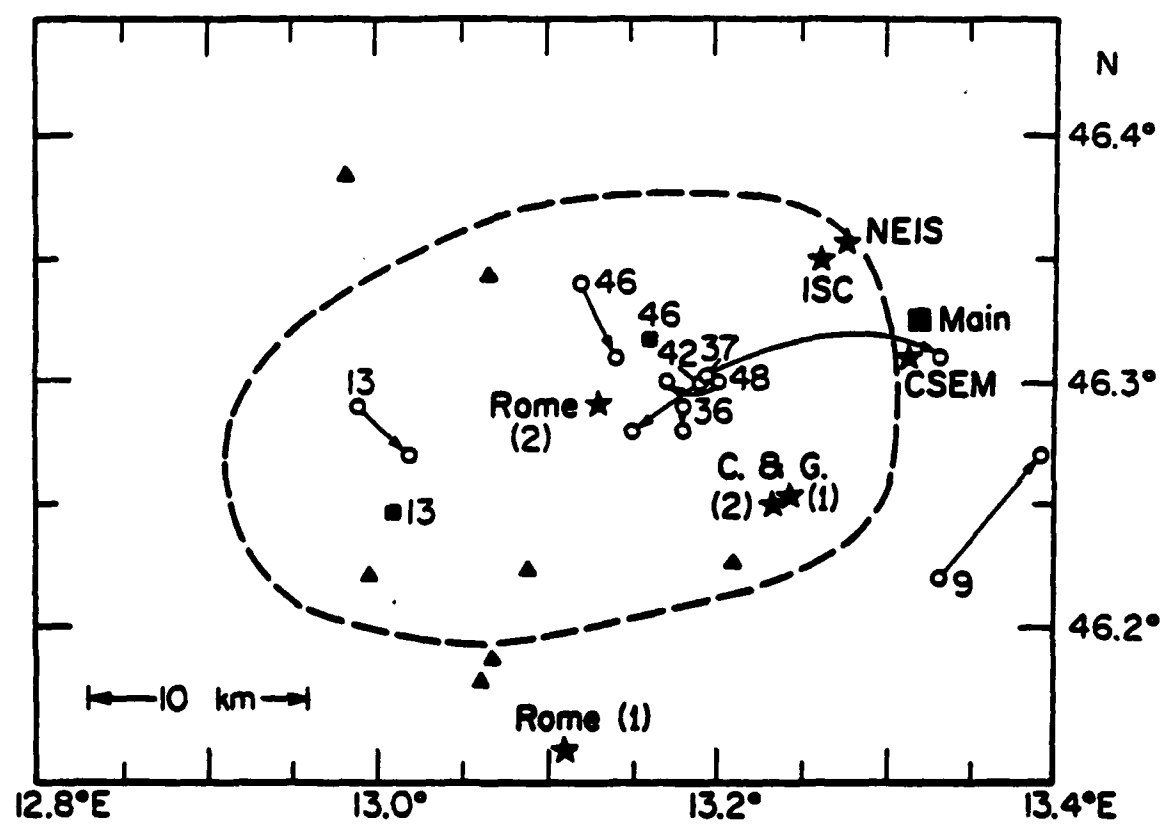


Fig. 3

FRIULI, ITALY

compression •
dilatation ○

$\phi = 76^\circ$
 $\delta = 75^\circ S$
 $\lambda = 80^\circ$

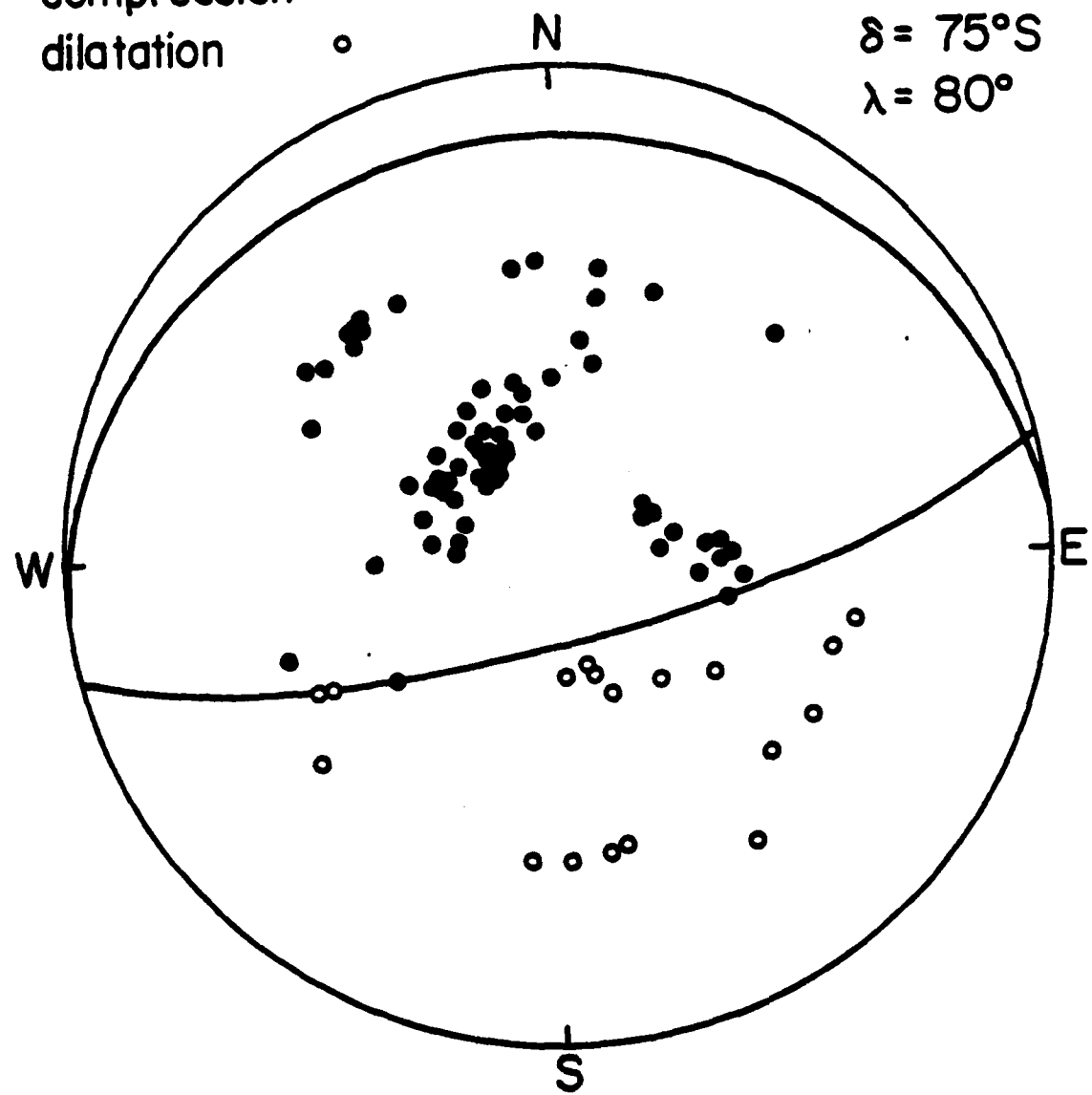


Fig. 4

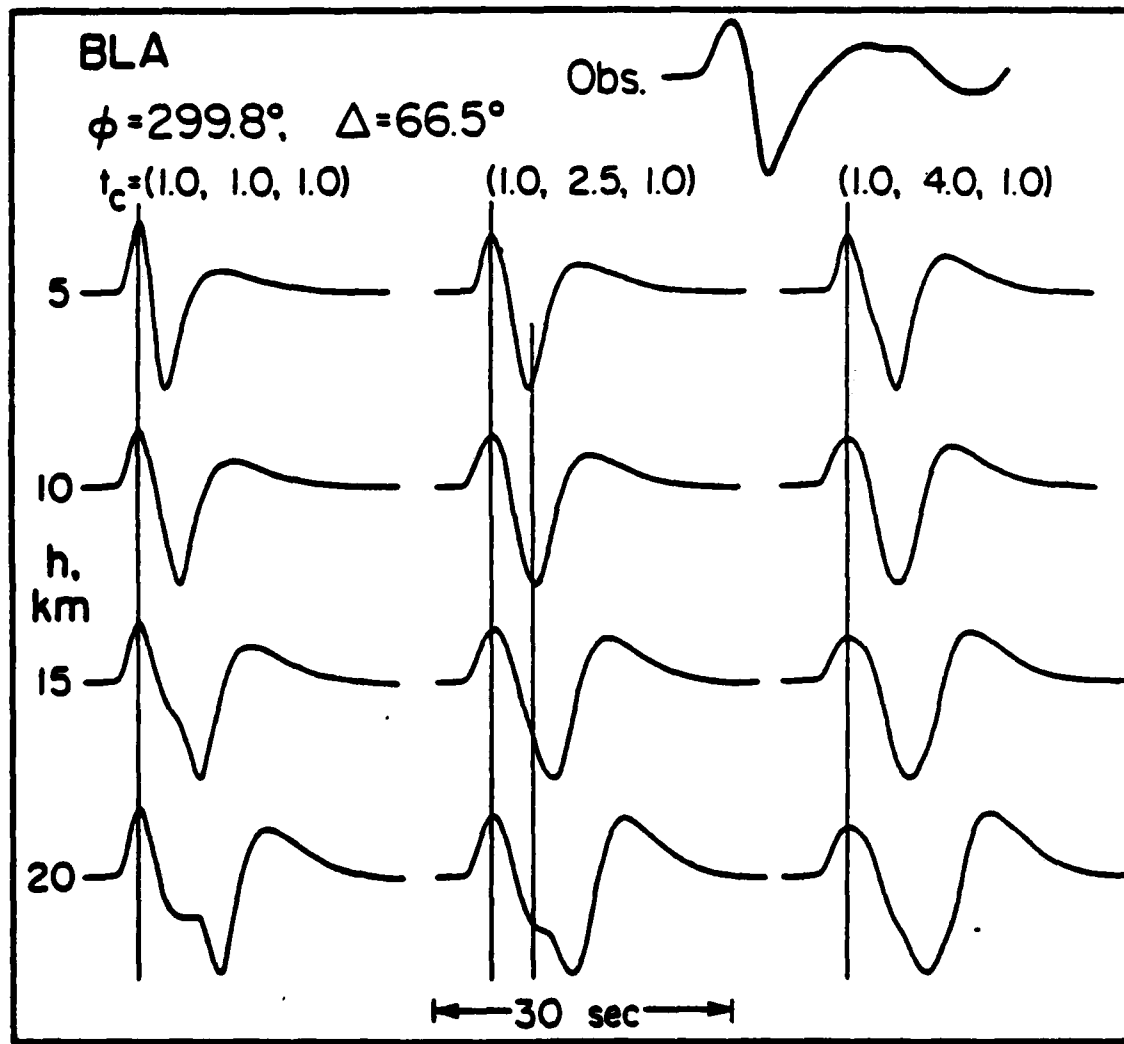


Fig. 5

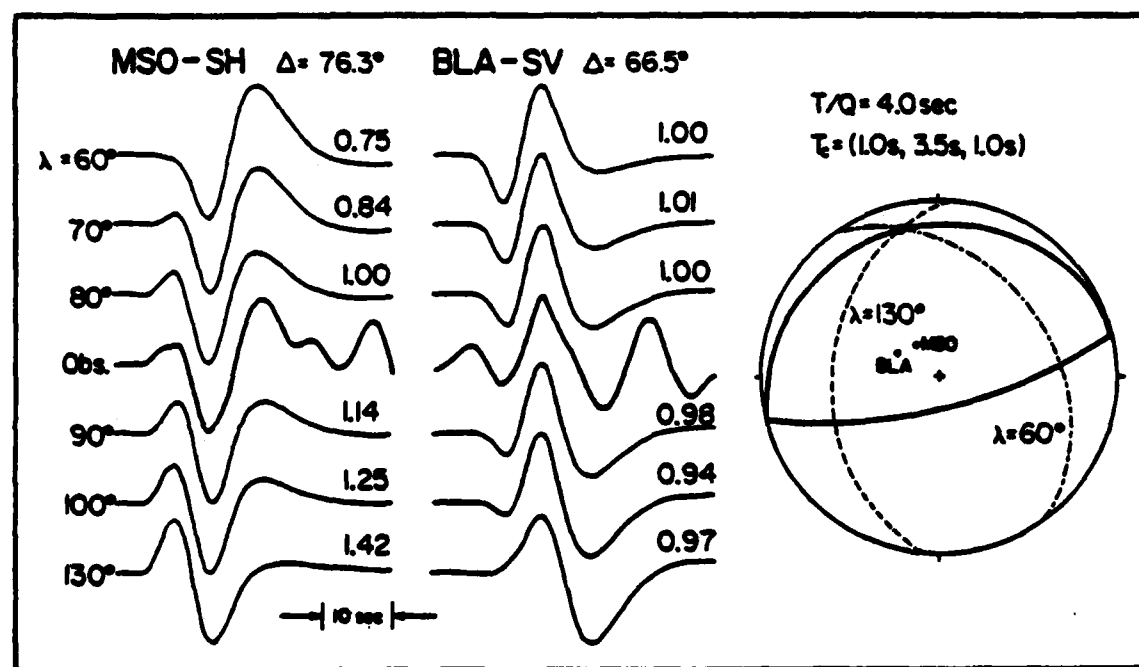


Fig. 6

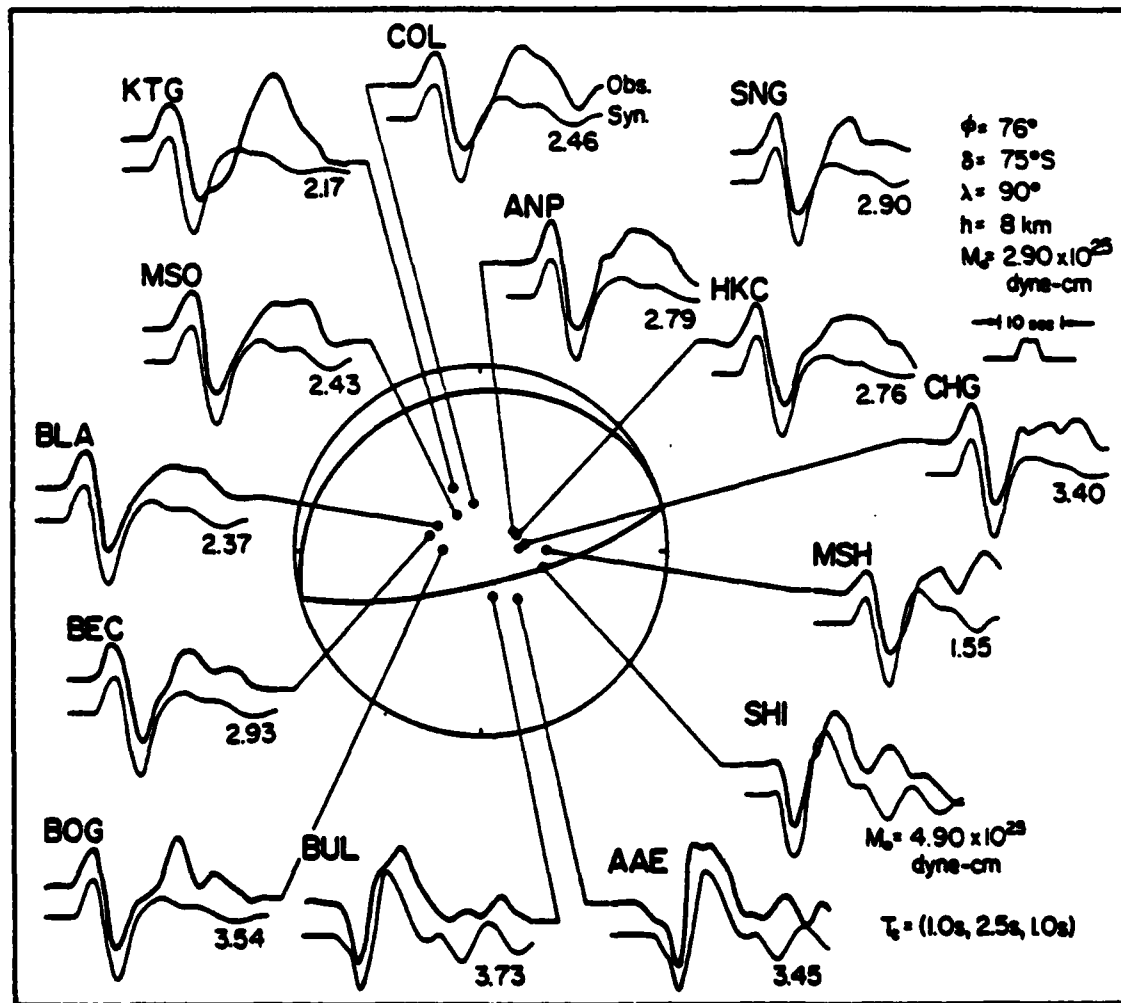


Fig. 7

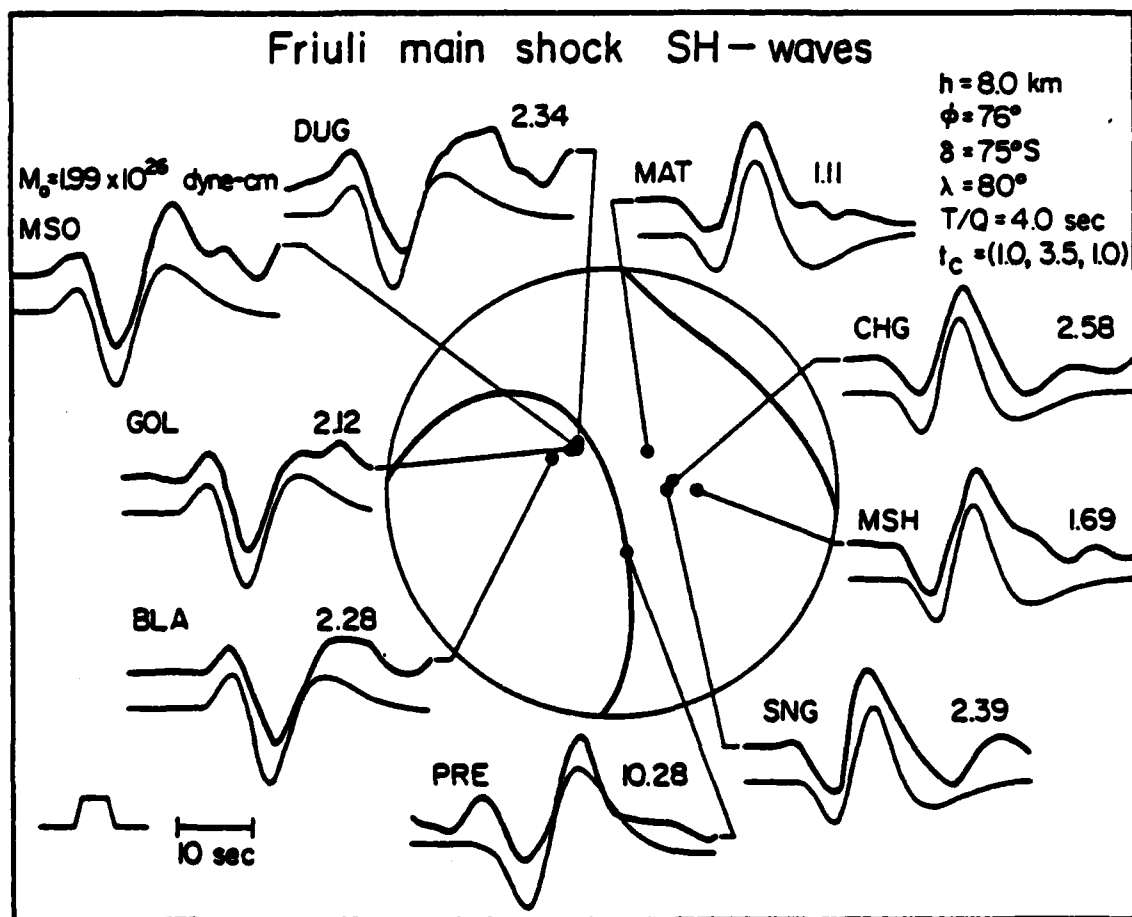


Fig. 8a

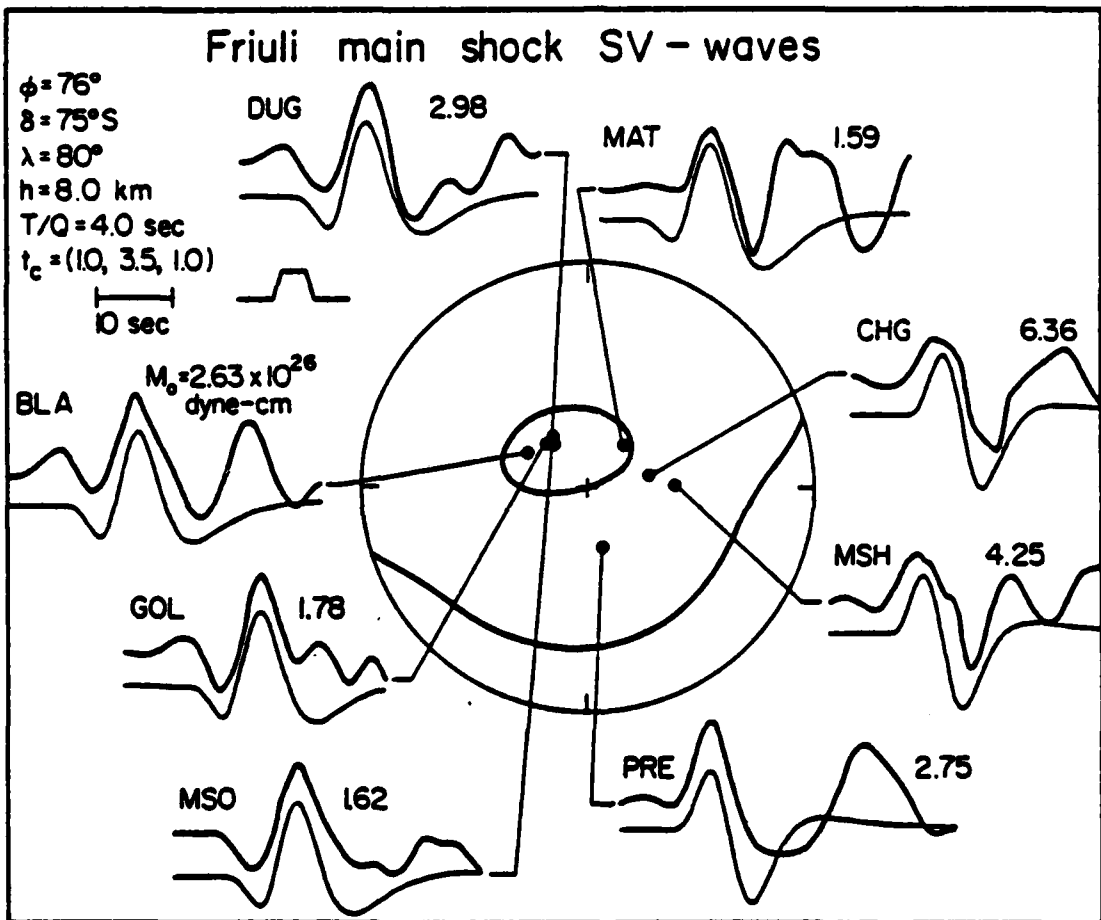


Fig. 8b

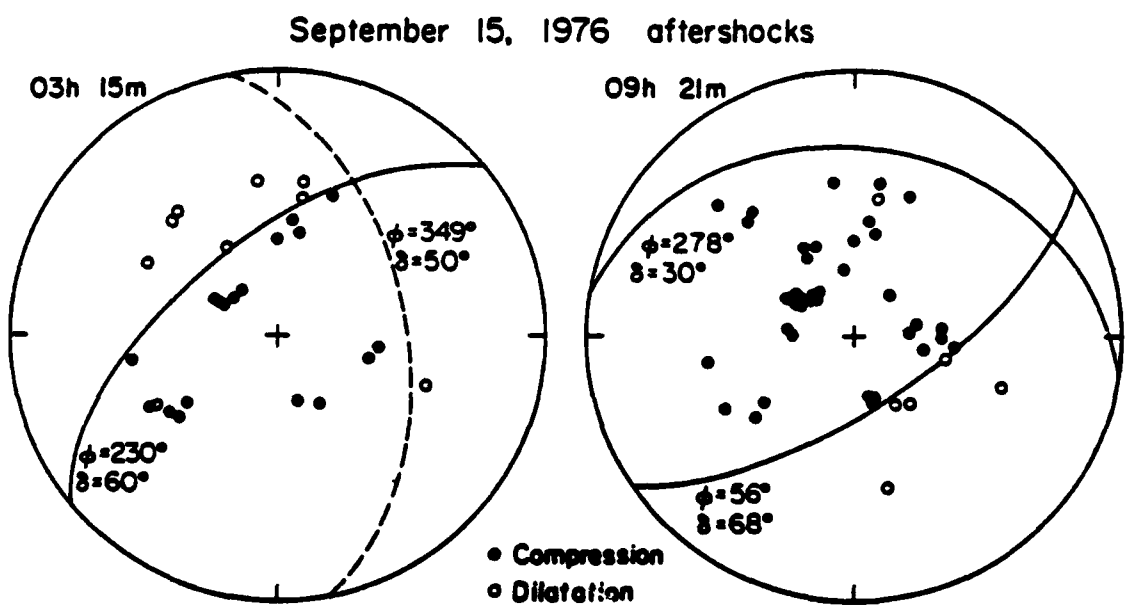


Fig. 9

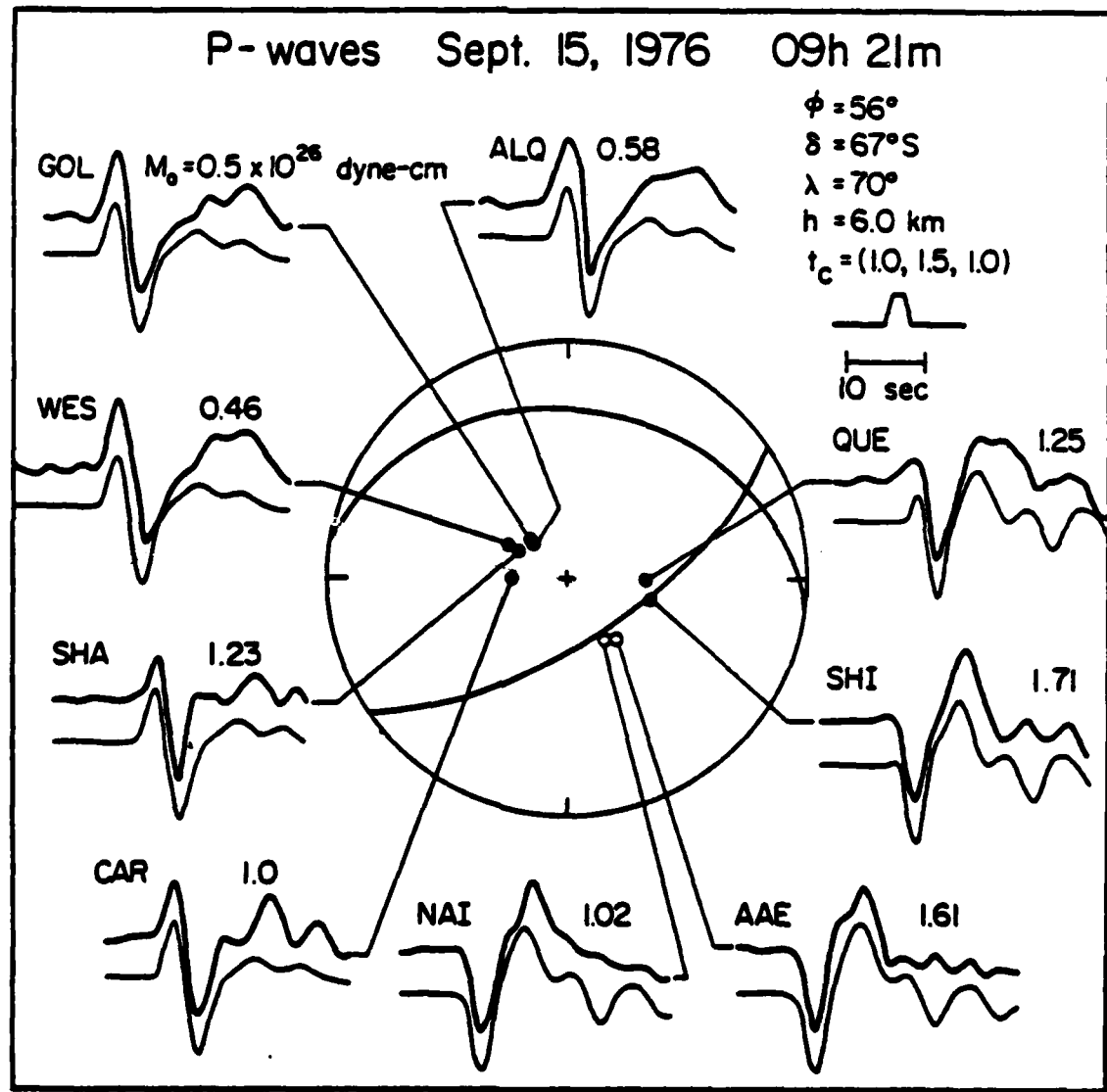


Fig. 10

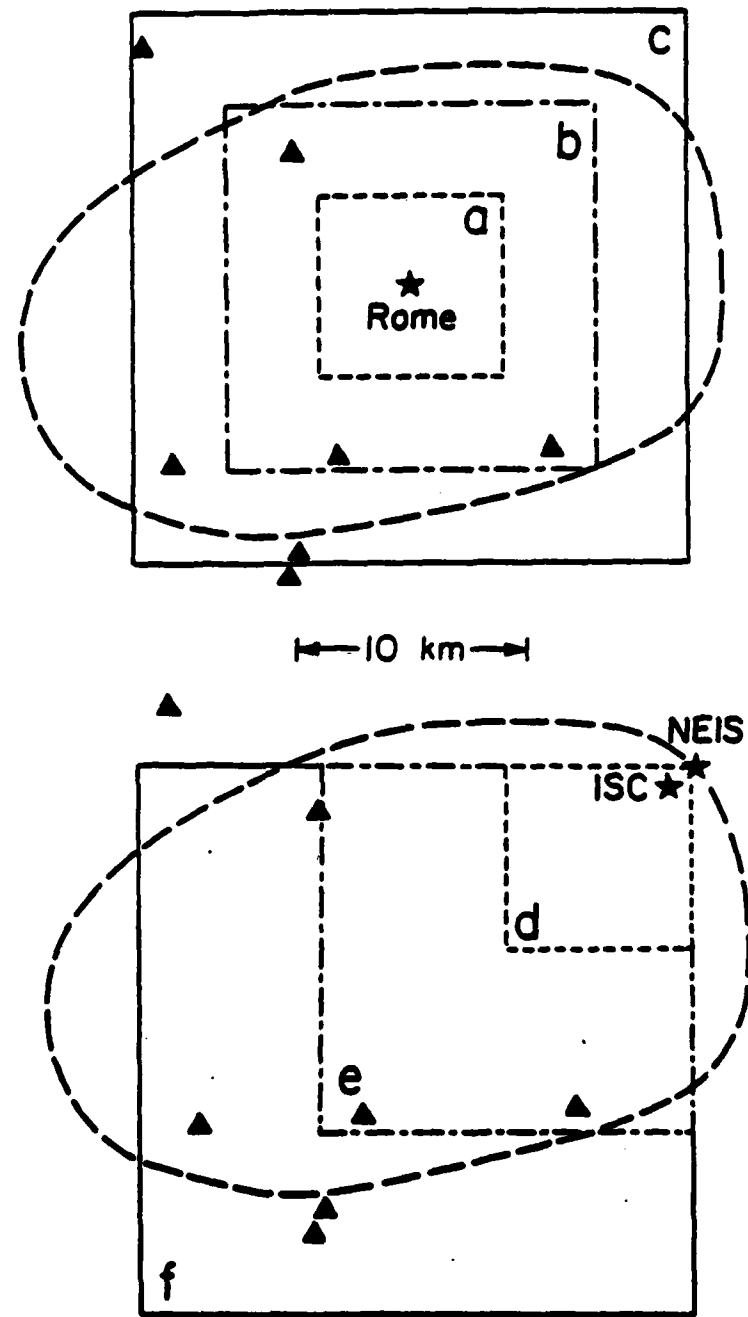


Fig. 12

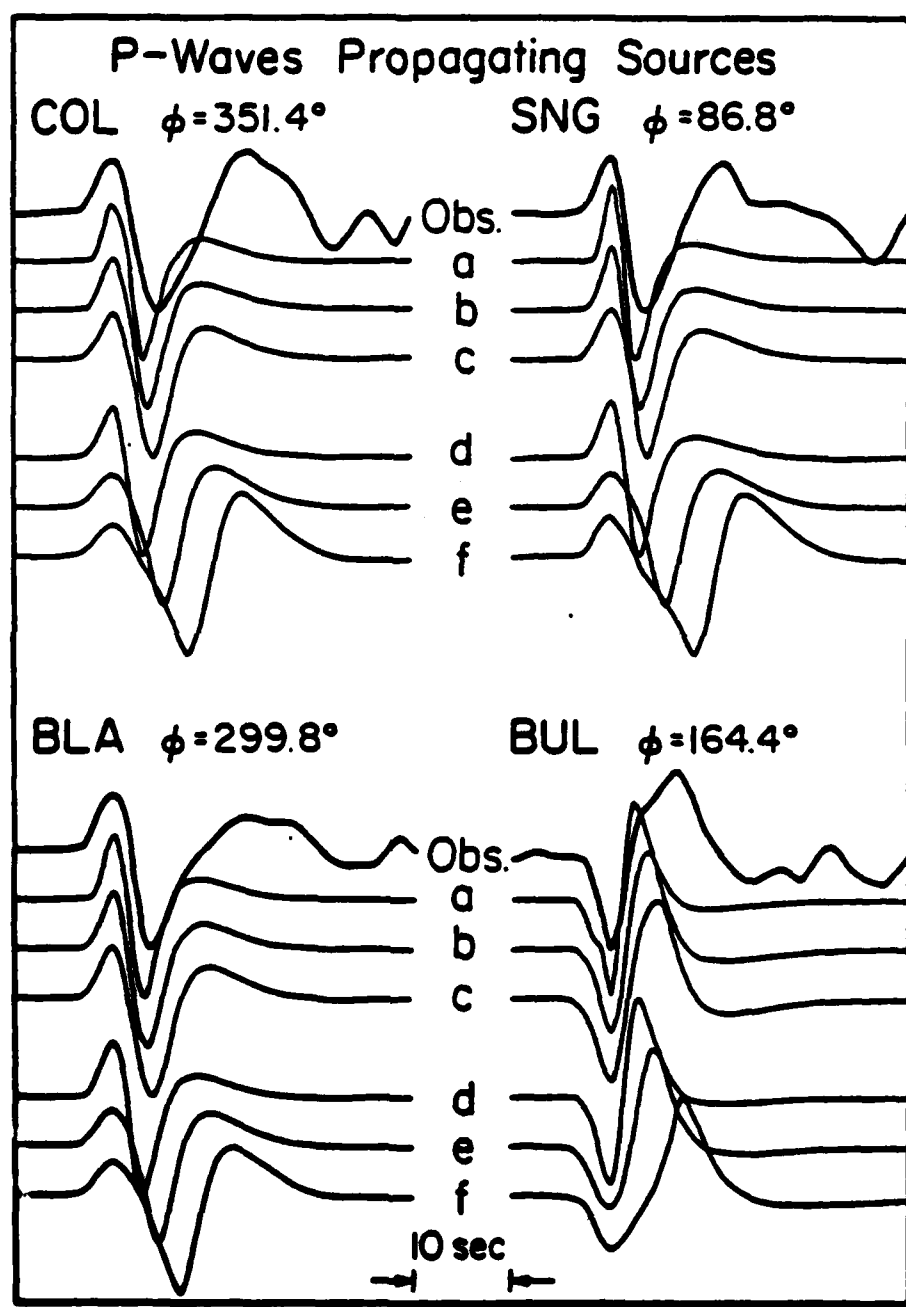


Fig. 13

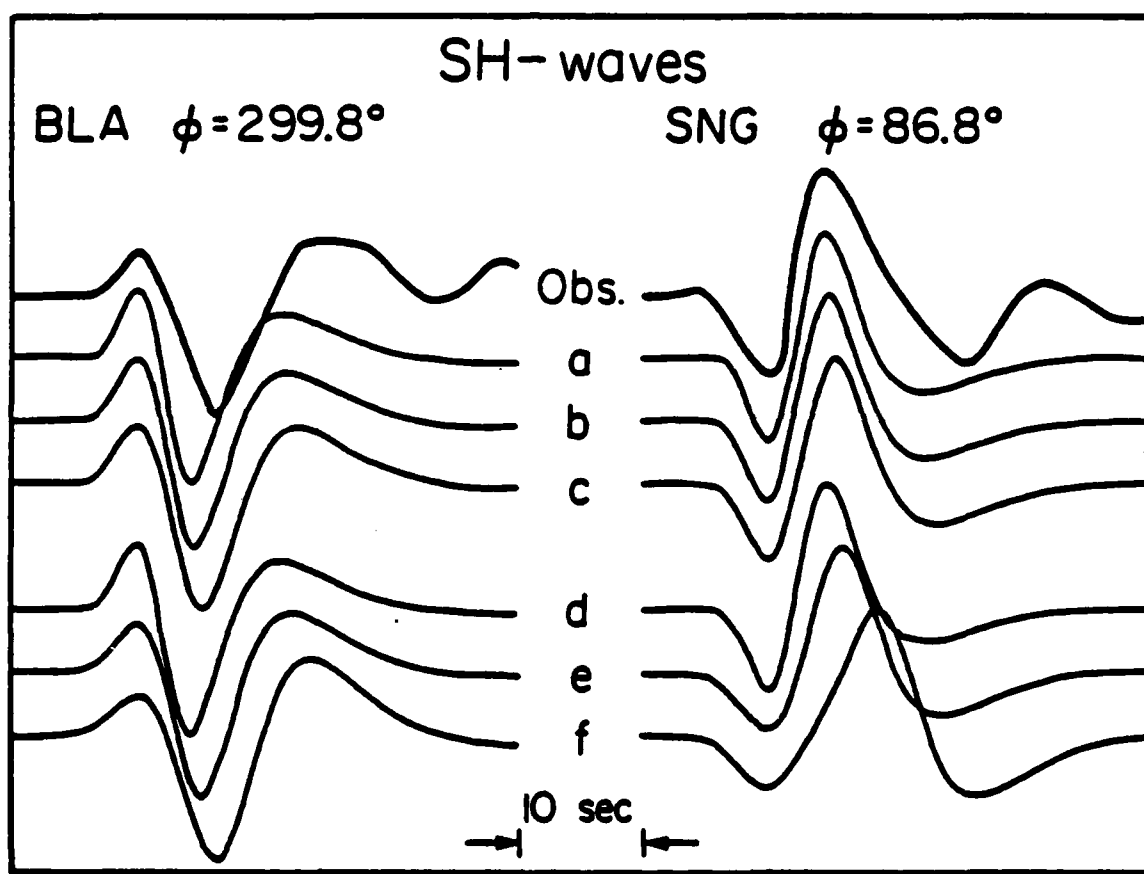


Fig. 14

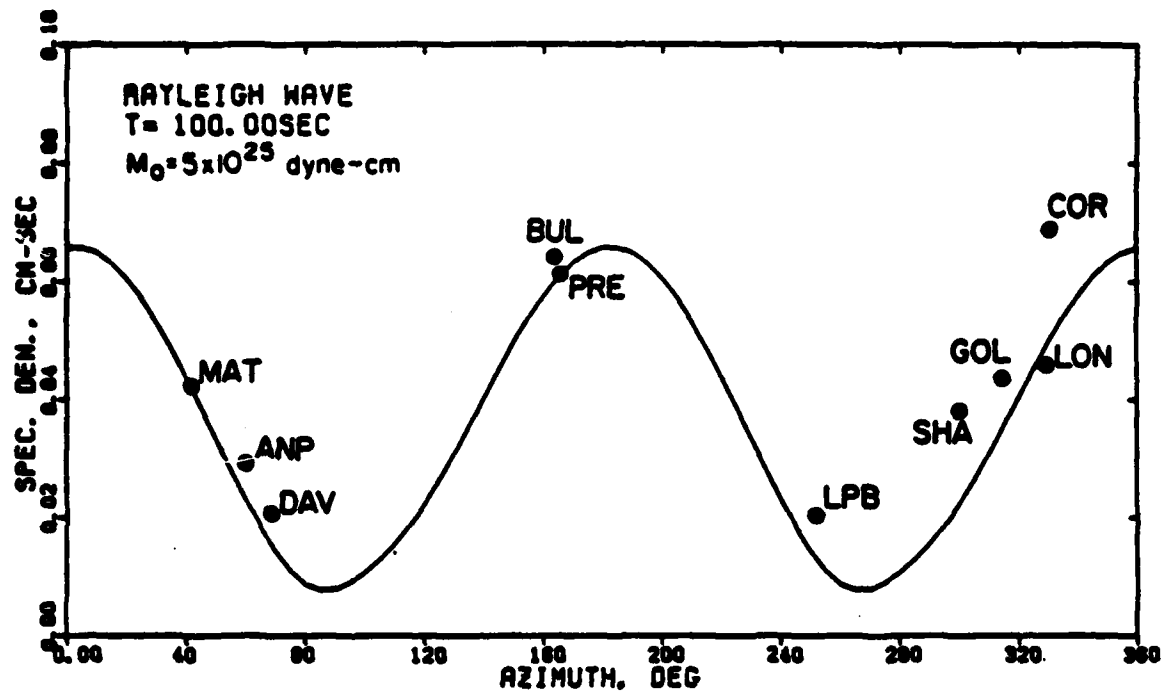


Fig. 15

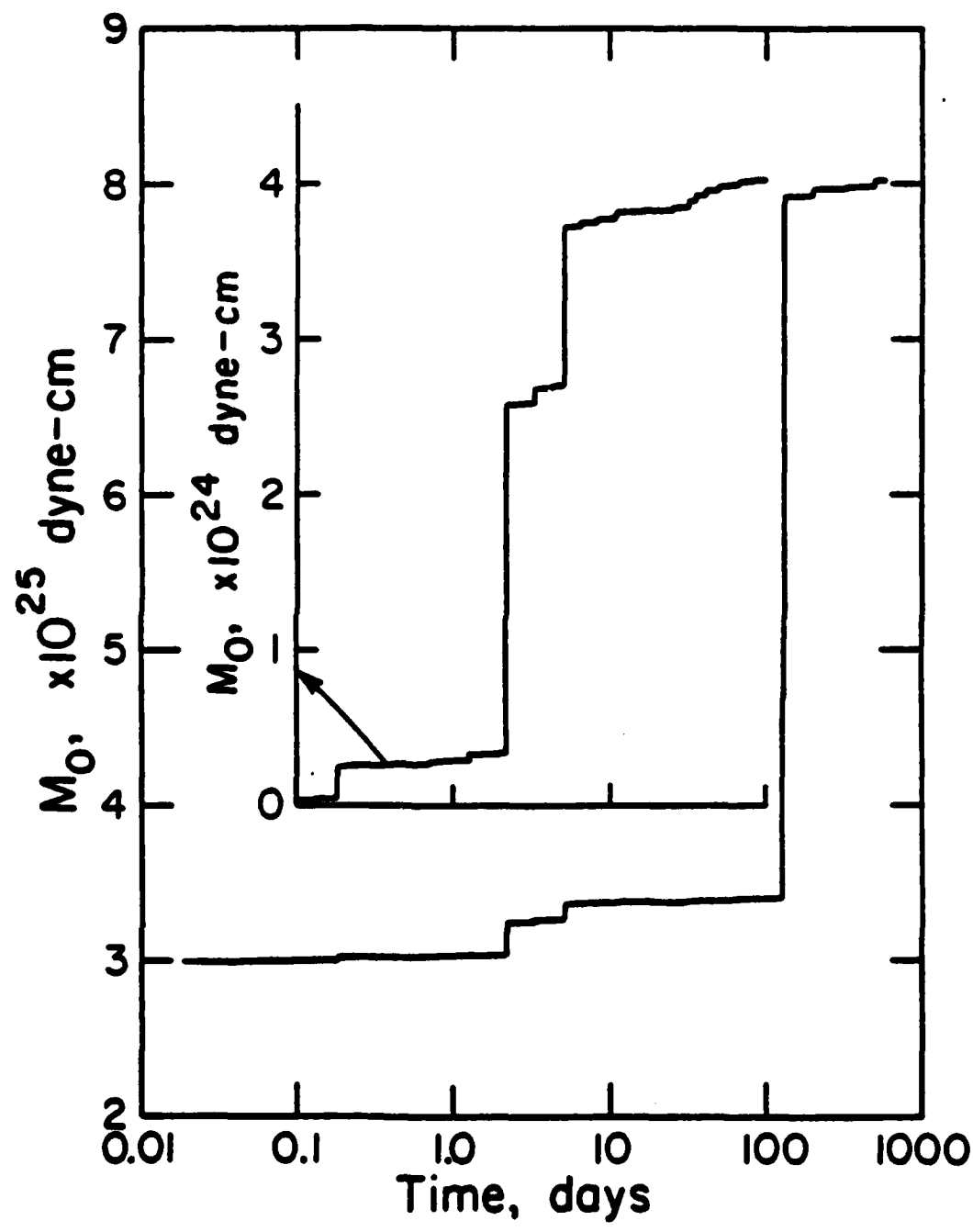


Fig. 16

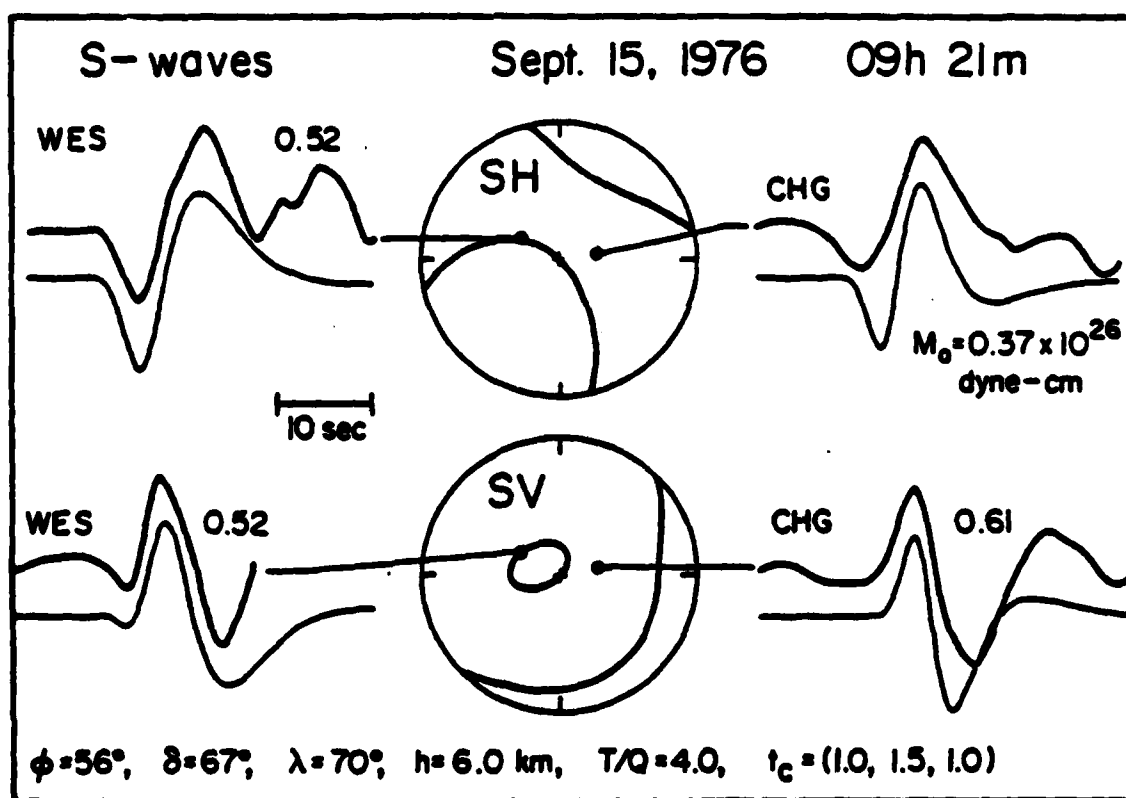


Fig. 11